ABSTRACT

Title of dissertation: A Probe of Colored Medium Effects on Quarkonia Polarization in $\sqrt{s} = 7$ TeV pp collisions at CMS

Charles Christopher Ferraioli
Doctor of Philosophy, 2017

Dissertation directed by: Professor Alice C. Mignerey
Department of Chemistry

The suppression of quarkonia mesons is one of the signature indications of the presence of a quark-gluon plasma, the colored, asymptotically free state of matter believed to have existed moments after the Big Bang, and recreated by colliding heavy-ions. Two S-wave charmonia states, the J/ψ and the $\psi(2S)$, along with three S-wave bottomonia states, the $\Upsilon(1S)$, $\Upsilon(2S)$, and $\Upsilon(3S)$, have been studied in heavy-ion collisions at both the Relativistic Heavy Ion Collider and the Large Hadron Collider (LHC), showing clear sequential suppression patterns, with the most tightly bound states less suppressed than the others, relative to scaled proton-proton (pp) collisions. Yet, the results remain difficult to interpret, owing to a combination of complicated feed-down processes from P-wave χ states, as well as regeneration of quarkonia occurring well after the initial collision. Further, the basic production mechanism of quarkonia is still far from certain, leaving open the possibility that changing mechanisms could affect the scaling of pp yields. This thesis aims to be the first in a line of studies into the effects of a colored medium on

the basic production mechanism of quarkonia by measuring quarkonia polarization.

Polarization can be measured using the angular distributions of dimuons emanating from quarkonia decays, and the Compact Muon Solenoid detector is well suited for these measurements. The polarizations of the three $\Upsilon(nS)$ and two $\psi(nS)$ states were measured versus event multiplicity using a dimuon data sample collected during the 2011 LHC run of $\sqrt{s} = 7$ TeV pp collisions, with a total integrated luminosity of 4.9 fb^{-1}. The measurements were integrated over the available rapidity range, for transverse momentum up to 35 GeV/c. All quarkonia states showed small polarizations, which were cross checked across several reference frames, and are consistent with multiplicity-integrated analyses. In the states for which a precise measurement could be made, the J/ψ and the $\Upsilon(1S)$, there was no variation with multiplicity, but these states are strongly affected by feed-down, preventing any definitive conclusions. Ultimately, this study leads the way for a polarization measurement in heavy-ion collisions, which would provide a more decisive look into the affect of a colored medium on quarkonium production.

A Probe of Colored Medium Effects on Quarkonia Polarization in $\sqrt{s} = 7$ TeV pp collisions at CMS

by

Charles Christopher Ferraioli

Dissertation submitted to the Faculty of the Graduate School of the
University of Maryland, College Park in partial fulfillment
of the requirements for the degree of
Doctor of Philosophy
2017

Advisory Committee:
Professor Alice C. Mignerey, Chair/Advisor
Professor Millard Alexander
Professor Sarah Eno
Professor John Ondov
Professor William Walters

Acknowledgments

When I first met my advisor, Dr. Alice Mignerey, she showed me a poster that accentuated the "XTREME" physics of the LHC - which is exactly why I was interested in joining her group in the first place. At that point, though, that was the extent of my knowledge of the field. I have spent the ensuing six years trying to absorb as much of her extensive knowledge as possible, and much of my success can be attributed to her. Alice, herself a sailor, gave me the freedom to chart my own course through the sometimes turbulent seas of graduate school, and for that I am both incredibly grateful, and a better scientist.

The list of colleagues who have helped along the way is long, but must begin with Jaime Gomez, who first showed me exactly what a "Terminal window" was, and taught me my first few commands. Once I moved beyond these first steps, the world of CMSSW, ROOT, and GEANT awaited, for which I have Marguerite Tonjes to thank for helping me to conquer, who deserves a special thanks for keeping the cluster up and running, despite my repeated attempts to crash it.

A wealth of gratitude is owed to the quarkonia polarization group - Valentin Knünz and Ilse Krätschmer, who held my hand as I learned the analysis, Pietro Faccioli and João Seixas for their enviable technical prowess and willingness to explain the minutiae of polarization analyses, and to Carlos Lourenço, who presented me with the opportunity to pursue a novel and interesting topic, and who coached me from a novice to the Ph.D. scientist I am today.

When not working on my analysis, I had the pleasure of working alongside

Michael Murray, the man behind the ZDC. The hands-on hardware experience and trips down to the CERN tunnel, while always a bit stressful, were something I looked forward to. I greatly enjoyed the time I spent working with Michael.

The rest of the ZDC group deserves mention as well - especially Quan Wang and Will McBrayer, who were always with me as we "enjoyed" the craziness of last minute ZDC software updates, ZDC installation issues, and trying to find the ZDC signal.

There are many others along the way who have made my time at CERN and Maryland unique and enjoyable - Raghav and James, who are defending their theses within a week of my own, as well as Owen, Ashley, Aaron, Teddy, and Andrew. A special shout out to Andrew who always gave me a couch to sleep on once I moved away from campus.

Of course, I wouldn't have made it to graduate school in the first place if it wasn't for my parents. Mom and Dad, thanks for all the support! You taught me the value of hard work, and encouraged me to pursue the things I loved most.

Finally, and most importantly of all, thank you to Jessie. Right from the beginning of my Ph.D. journey, when you helped me to craft my application personal statement, you've offered nothing but your full support, encouragement, understanding, and advice. You've always pushed me to be a better companion, scientist, and person, and you always made sure to keep me balanced. So much of my success is tied to you.

Table of Contents

List of Tables

List of Figures

List of Abbreviations

AA	Nucleus-nucleus (as in collisions)
CB	Crystal Ball
CERN	European Council for Nuclear Research
CS	Collins-Soper
CMS	Compact Muon Solenoid
CSC	Cathode Strip Chambers
DT	Drift Tube
ECAL	Electromagnetic Calorimeter
HCAL	Hadronic Calorimeter
HIN	Heavy ion
HLT	High-Level Trigger
HX	Helicity
IP	Interaction Point
LSB	Left Sideband
Level-1	L1 (as in trigger)
Level-2	L2 (as in trigger)
Level-3	L3 (as in trigger)
LHC	Large Hadron Collider
LDME	Long-distance matrix element
MC	Monte Carlo
NRQCD	Non-Relativistic Quantum Chromodynamics
pA	Proton-nucleus (as in collisions)
PX	Perpendicular Helicity
PMT	Photo-multiplier Tube
PbPb	Lead-lead (as in collisions)
pp	Proton-proton (as in collisions)
pPb	Proton-lead (as in collisions)
PDF	Probability Density Function
PS	Proton Synchrotron
PSB	Proton Synchrotron Booster
QCD	Quantum Chromodynamics
QED	Quantum Electrodynamics
QGP	Quark gluon plasma
RHIC	Relativistic Heavy Ion Collider
RPC	Resistive Plate Chambers
RSB	Right Sideband

SDCs	Short-distance coefficients
SLAC	Stanford Linear Accelerator
SPS	Super Proton Synchrotron
SR	Signal Region
T&P	Tag-and-probe
TEC	Tracker EndCaps
TIB	Tracker Inner Barrel
TID	Tracker Inner Disks
TOB	Tracker Outer Barrel

Chapter 1: Introduction

In the beginning, there was the quark gluon plasma.

According to our current measurements, the Universe sprang into existence 13.8 billion years ago in an event called the Big Bang [1]. What is believed to have followed in quick succession was an extreme inflation in the size of the universe, which broke the unification of the strong, weak, and electromagnetic forces. At the end of the inflation period, a mere 10^{-32} seconds after the Big Bang, the bulk of matter in the Universe was dominated mostly by fundamental particles called quarks, gluons, and electrons. At this stage, the Universe was so hot and dense that quarks, usually confined within bound states with other quarks, experienced a phenomenon known as asymptotic freedom that allowed these particles to move about, deconfined from other particles. This freedom lasted only a few microseconds before the Universe cooled enough and quarks coalesced to form particles called hadrons, most of which were then annihilated as hadrons made of anti-matter came into contact with those made of matter, creating photons. At this time, still only seconds after the Big Bang, the fundamental bits of "normal" matter now formed the bulk of the Universe in the form of a plasma of electrons, photons, and charged hadrons. For a few minutes, the Universe was hot enough that protons and neutrons

were able to undergo nucleosynthesis. At the end of the Big Bang nucleosynthesis, the elemental mass composition of the Universe was $\sim 75\%$ protons, $\sim 25\%$ Helium nuclei, and $< 1\%$ Lithium nuclei. The Universe remained in this opaque, plasma state for approximately 370,000 years, expanding and cooling, too hot for atoms to form and too cool for additional nucleosynthesis to proceed. Eventually, the temperature cooled enough for electrons to bind to nuclei, forming neutral atoms. Without charged matter to interact with, photons were effectively free to move, which made the Universe transparent. Now that the matter in the Universe was neutral, it became possible for matter to cluster together, through gravity, to form the seeds of galaxies, stars, and planets [2].

Then, 13.8 billion years after it all began, scientists were able to recreate the hot, dense environment that dominated the first microseconds of the Universe. In 2000, the Relativistic Heavy Ion Collider (RHIC), a particle accelerator located at Brookhaven National Laboratory in New York, began colliding gold nuclei in an effort to recreate the matter postulated to have briefly existed in the first microseconds of the Universe [3]. These collisions are called heavy-ion collisions, and the ephemeral state of matter is called the Quark-Gluon Plasma (QGP). The evolution of the Universe is presented in Figure 1.1, beginning with the Big Bang and illustrating all the major stages of the Universe up through today.

This thesis explores the experimentalist's toolkit for understanding the QGP, focusing specifically on a group of particles called quarkonia. The fundamentals of the Standard Model and the QGP will be presented in Ch. 2. The focus will turn to quarkonia, their usefulness in understanding the QGP, and their production in

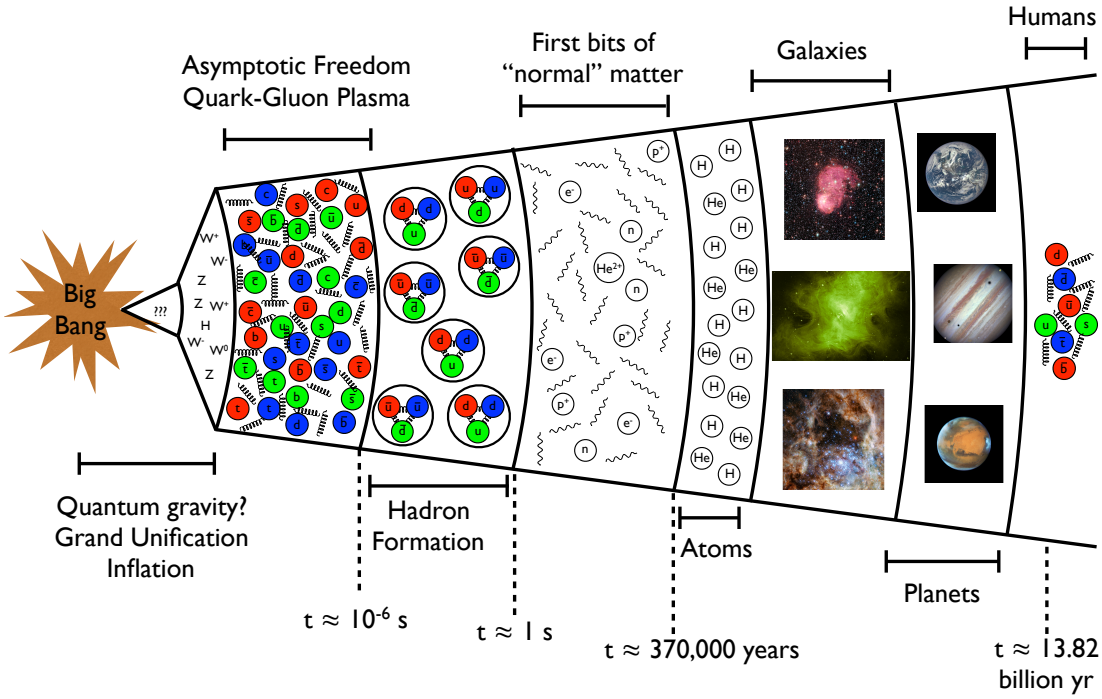

Figure 1.1: A diagram of the evolution of the Universe, started with the Big Bang and progressing through several of the main eras. The timeline ends with the recreation of the QGP in a lab. Contains images freely available for use from NASA.

Ch. 3. The instruments used to collide heavy ions and to detect the aftermath, the Large Hadron Collider (LHC) and the Compact Muon Solenoid (CMS), respectively, will be detailed in Ch. 4. Chapter 5 represents the full details of an analysis strategy used to measure quarkonia polarizations in different background environments. The results and interpretation of this analysis will be presented in Ch. 6. Overall, this thesis presents a novel analysis intended to be the first set of a series of experiments to test the effect of the nuclear medium on the production on quarkonia particles. A common practice for new measurements is to perform them in the simplest system, which, in this case, is by measuring the properties of quarkonia in proton-proton collisions, where a QGP is not expected to form. A better understanding of basic quarkonia production will help improve the interpretation of quarkonia measure-

ments in heavy-ion collisions.

Chapter 2: The Standard Model

"If we find something we can't understand we like to call it something you can't understand, or indeed pronounce."

~Douglas Adams

Akin to the more well known arrangement of elements into the periodic table, subatomic particles are grouped based on how they behave, organized as shown in Fig. 2.1. The first distinction among subatomic particles is made depending on whether particles with the same properties can be in the same place at the same time. That is, whether they obey the Pauli Exclusion Principle that arises from Fermi-Dirac statistics, or they obey Bose-Einstein statistics. In more concrete terms, the Pauli Exclusion Principle states that identical particles cannot simultaneously occupy the same quantum state, which is why atomic orbitals are restricted to two electrons with opposite spins. In contrast, this is allowed by Bose-Einstein statistics. Which of these behaviors a particle exhibits is due to an intrinsic quantum property called spin. In particular, particles with integer spins[1] will follow Bose-Einstein statistics, and are therefore called bosons, whereas those with half-integer spins are subject to the Pauli Exclusion Principle and are called fermions. All of

[1] Technically, spin is measured in multiples of $h/2\pi$, but for simplicity's sake this term is dropped.

Figure 2.1: The Standard Model of fundamental particles: quarks (green), leptons (blue), and bosons (red), and enveloped by the Higgs field.

these particles and the interactions between them are described by a theory called the Standard Model.

2.1 The Fundamental Forces and Particles

There are four distinct, fundamental forces that act throughout the Universe: the strong, weak, electromagnetic, and gravitational forces. Three of these forces are described by the Standard Model. The familiar electromagnetic force is a long-range force described using a field theory called quantum electrodynamics (QED). QED describes the interaction of light and electrically charged matter through the exchange of a gauge boson[2] called a photon (γ). The electromagnetic force is closely related to the weak force, and in fact, at high enough energies, these two forces

[2]All Standard Model force carriers are gauge bosons, with a spin of one.

merge into a single electroweak force [4]. The weak force, apparent only at very small distances, is carried by either a neutral Z boson or electrically charged $W^{+(-)}$ bosons, and is responsible for processes such as radioactive decay. The strong force, appropriately named as it is the strongest of the fundamental forces, introduces a concept called color, which is described in more detail in Sec. 2.2.3. The strong force is described by quantum chromodynamics (QCD) and acts through the exchange of gauge bosons called gluons (g). Gluons work on femtometer (10^{-15} m) scales and are responsible for confining quarks into hadrons, as well as binding protons and neutrons into stable nuclei. Hadrons are further organized into quark-antiquark (mesons) and three-quark (baryons) groups. The fourth force, gravity, has not yet been included into the Standard Model, and is instead described by Einstein's general relativity. It is thought to be mediated through a hypothetical tensor boson[3] called a graviton.

The interaction of the Standard Model forces with different fermions allows us to group these particles further. Fermions that exchange gluons via the strong force are said to have "color" charge and are called quarks (q). There are three generations of quark pairs, with each generation subsequently heavier, but with consistent charge and always with spin = 1/2. The first generation of quarks consists of the up (u) and down (d) quarks, with charges of $+2/3$ and $-1/3$, respectively. The second and third generation quarks are the charm (c, charge = $+2/3$) and strange (s, charge = $-1/3$) quarks, and the bottom (b, charge = $+2/3$) and top (t, charge = $-1/3$) quarks. Collectively, these six different quarks represent all the quark "flavors"

[3] A boson with a spin of two.

known to the standard model, and they interact with all four fundamental forces. Through the strong force, quarks come together to form hadrons like the proton and neutron. In addition to the quarks, each has an associated antiquark (notated using a bar over the letter, i.e. $\bar{q}$), which is identical to the quark, except with opposite quantum numbers.

A second group of fermions consist of particles that do not have color charge and therefore do not interact via the strong force; these particles are called leptons. Like quarks, there are three generations of lepton pairs, totaling six lepton flavors. The common electron (e, charge $= -1$), alongside it's partner, the electron neutrino (ν_e, neutral), make up the first generation. Like quarks, the second and third generation particles are heavier analogues of the e and the ν_e, called the muon (μ), muon neutrino ν_μ, tau (τ), and the tau neutrino (ν_τ)[4]. These particles mainly interact through electroweak forces, although the chargeless neutrinos do not interact via electromagnetic mechanisms. Like quarks, the leptons also have associated antiparticles.

The final piece of the Standard Model is the Higgs field that is thought to canvas the entire Universe. The Higgs field was confirmed in 2012 through the discovery of the long sought-after Higgs boson [5]. The remainder of this thesis is dedicated to more thoroughly understanding QCD by studying how certain hadrons are formed, and how they interact within a QGP.

[4]It should be noted that present understanding is that neutrinos exist in the mass eigenstates "light," "middle," and "heavy," that are superpositions of the weak eigenstates "electron," "muon," and "tau."

2.2 Development of the Strong Nuclear Force

In 1932, the proton, neutron, electron, and photon were thought to be the only fundamental particles. Noting that protons and neutrons had the same spin and nearly identical masses, Werner Heisenberg invented a new quantum number called "isospin" (I) to describe this apparent symmetry between protons and neutrons [6]. The isospin was simply a mathematical construct that allowed a proton to change into a neutron, and vice versa, through a rotation around an axis. This behavior is represented by special unitary matrices, which in this case is a set of 2×2 unitary matrices, an $SU(2)$ symmetry group. A nucleon (that is, a proton or a neutron), was assigned $I = 1/2$, and the proton and neutron were distinguished due to their opposite isospin projections ($|I, I_3\rangle$):

$$p = |1/2, +1/2\rangle \quad n = |1/2, -1/2\rangle.$$

A few years later, Hideki Yukawa published the first comprehensive theory of the force that carried isospin [7]. This force was responsible for holding together a nucleus, necessitating that it was *stronger* than the electric repulsion experienced by positively charged protons; hence, this force was called the strong force. Yukawa's theory asserted that there must be a strong-force mediating particle that was more massive than an electron, yet not as massive as a proton. In 1937, a new particle was discovered that fit within this range [8]. But there was a problem: this particle behaved *exactly* like an electron. In fact, this particle was the muon, and it's discovery was entirely unexpected.

Particles exhibiting the strong force were not found until 1947, with the discovery of the pion [9]. Pions came in a triplet, and lent further credence to the idea of isospin. If pions had an isospin of one, then each pion was simply a different projection of the isospin, exactly like the nucleons:

$$\pi^+ = |1, +1\rangle \quad \pi^0 = |1, 0\rangle \quad \pi^- = |1, -1\rangle.$$

The year 1947 also brought something a bit *strange*. Particles were discovered that were heavier than nucleons and uniquely long-lived. These particles, dubbed kaons (K), were always produced in conjunction with other heavy, long-lived particles that are now know as sigma (Σ) and lambda (Λ) baryons. To account for these new particles, in 1953, two independent scientists, Murray Gell-Mann and Kazuhiko Nishijima, conceived of another quantum number, called strangeness [10, 11]. They introduced an equation that related the charge (Q), isospin projection (I_3), baryon number (B), and the new term, strangeness (S):

$$Q = I_3 + \frac{1}{2}(B + S). \tag{2.1}$$

However, there was a problem with how strangeness fit in to the budding theory. The addition of a new quantum number meant that the strong force could not be described by an $SU(2)$ group. Meanwhile, the continued emergence of new particles led to an ever-increasing "particle zoo," which was difficult to explain.

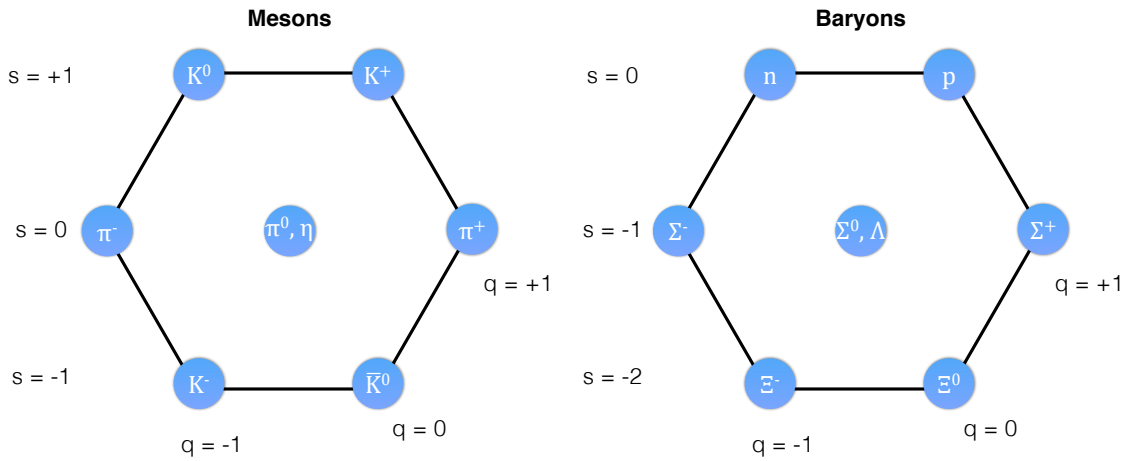

Figure 2.2: A depiction of Gell-Mann and Ne'eman's method of grouping hadrons, where "s" is strangeness and "q" is charge.

2.2.1 The Eightfold Way

A solution to the symmetry group dilemma emerged in 1961 when Gell-Mann, and independently, Yuval Ne'eman, developed a new method to organize the variety of particles [12,13]. By adding an additional rotation around the "strangeness" axis, and thus increasing from an $SU(2)$ to an $SU(3)$ symmetry group, hadrons with matching spins could effectively be grouped. This new grouping produced particle octets, and Gell-Mann named this model the Eightfold Way[5]. The octets for spin $= 0$ mesons and spin $= 1/2$ baryons are shown in Fig. 2.2. The presentation of the Eightfold Way wasn't only a method for organizing existing particles, it also had predictive power: the η meson and the Ω^- baryon, excepted to complete the spin $= 0$ meson octet and spin $= 3/2$ decuplet, respectively, had not yet been discovered. This changed later in 1961 with the discovery of the η meson [14] and in 1964 with the discovery of the Ω^- [15].

[5]A nod to Buddhism's Eightfold Path to Enlightenment

2.2.2 Quarks

A description of the strong force was well underway, but a nagging issue remained: just as $SU(2)$ demands a doublet (the $+1/2$ "up" and $-1/2$ "down" isospin doublet), $SU(3)$ suggests there should be some sort of fundamental triplet state, which, as of yet, was completely missing from data. In 1964, Gell-Mann [16], simultaneously with George Zweig [17], devised a new idea in which *hypothetical* "quarks"[6] individually carried "up", "down", and "strange" charges. A baryon must contain three of these hypothetical particles, and a meson two, where one would be the anti-matter version of the quark, its anti-quark. This new accounting perfectly explained the entire particle zoo, but it came with a catch. In order to match the charge of any particle, quarks had to have fractional charges. Even Gell-Mann himself was skeptical, writing in the paper that introduced quarks (emphasis added) [16]

> It is fun to speculate about the way quarks would behave if they were physical particles of finite mass. ... A search for stable quarks of the charge $-1/3$ or $+2/3$ and/or stable di-quarks of charge $-2/3$ or $+1/3$ or $+4/3$ at the highest energy accelerators would help to **reassure us of the non-existence of real quarks**.

Around this time, the Stanford Linear Accelerator (SLAC), a particle accelerator capable of probing the internal structure of a proton, was being built. At SLAC, electrons are accelerated along a two mile beam and collided into hydrogen in what

[6] "Quarks" according to Gell-Mann, from a line in Finnegans Wake - "Three quarks for Muster Mark!". "Aces" according to Zweig. Quarks stuck.

is essentially a scaled up version of Rutherford's scattering experiment. With the electron playing the role of the alpha particle, and the proton playing the roll of the gold atoms, scientists studied the scattering angles of the incident electrons. Over a period of experiments beginning in 1967, SLAC and MIT scientists demonstrated that the electrons scattered sharply off protons [18]. In fact, these experiments revealed that the proton had three scattering centers - the first experimental indications of the existence of quarks. Quarks were not simply a whimsical trick that could make sense of the particle zoo, they were real, physical particles that made up nucleons. Quarks, along with gluons, are now recognized as the fundamental parts of nucleons and are collectively referred to as "partons."

2.2.3 Color Charge

While the conjecture and discovery of quarks explained much of the particle picture, there were a few glaring exceptions: the Δ^{++}, Δ^{-}, and Ω^{-} baryons. These are spin = 3/2 particles that contain, respectively, three up quarks, three down quarks, and three strange quarks. As fermions, these particles are required to follow Fermi-Dirac statistics, yet each has three seemingly identical quarks sharing a quantum state, in clear violation of the Pauli Exclusion Principle. The first person to point out this problem was Oscar Greenberg, now an Emeritus Professor at the University of Maryland, who postulated the existence of a hidden quantum number that would differentiate the quarks [19]. In 1973, William Bardeen, Harald Fritzsch, and, once again, Gell-Mann, further developed Greenberg's idea and intro-

duced the concept of a new quark quantum number called color [20]. Taking into account color, baryons (B) and mesons (M) are described as color singlets made up of colored quarks:

$$B = \frac{1}{\sqrt{6}}\epsilon^{\alpha\beta\gamma}|q_\alpha q_\beta q_\gamma\rangle, \quad M = \frac{1}{\sqrt{3}}\epsilon^{\alpha\beta}|q_\alpha \bar{q}_\beta\rangle, \tag{2.2}$$

where $q(\bar{q})$ are quarks (anti-quarks) and ϵ is the Levi-Civita tensor.

Analogous to QED, color charge is transferred between particles through a boson, in this case the gluon. Unlike QED, with one kind of charge being mediated through the uncharged photon, there are three color charges called red, blue, and green, and the gluon is itself colored with the following octet of color states[7]:

$$\begin{aligned}
(r\bar{b} + b\bar{r})/\sqrt{2}, \quad & -i(r\bar{b} + b\bar{r})/\sqrt{2} \\
(r\bar{g} + g\bar{r})/\sqrt{2}, \quad & -i(r\bar{g} + g\bar{r})/\sqrt{2} \\
(b\bar{g} + g\bar{b})/\sqrt{2}, \quad & -i(b\bar{g} + g\bar{b})/\sqrt{2} \\
(r\bar{r} - b\bar{b})/\sqrt{2}, \quad & (r\bar{r} + b\bar{b} - 2g\bar{g})/\sqrt{6}.
\end{aligned}$$

A consequence of color-charged gluons is that gluons can self-couple. This feature is the key difference between QED (photons do not self-interact) and QCD, and leads to unique features in QCD like color confinement and asymptotic freedom, which are described in the following two sections. Additionally, self-coupling makes studying QCD much more difficult because the boson both mediates *and* interacts.

[7] This common listing is presented in [21].

2.2.3.1 Confinement

Despite the experimental evidence and theoretical explanations for quarks, an isolated quark has never been observed. Coupled with the observation that all identifiable particles are color-neutral leads to the QCD confinement hypothesis: all colored particles must be confined into composite color-neutral particles. To understand confinement, it is convenient to think of a gluon acting as a spring between two quarks. As the quarks are pulled apart, the gluon "spring" increases in potential energy. One could naively expect that at a certain point the gluon would break and the energy stored in the "spring" would transfer to the quarks as they fly off in opposite directions. However, due to confinement, this cannot happen. Instead, once the potential energy stored in the "stretched" gluon is large enough, it becomes more favorable to form a new quark-antiquark pair than to separate the original quarks further, and the energy is converted into a new hadron. This process can be seen in particle collisions. At high energies, some quarks and gluons are involved in hard scattering processes, in which a large amount of momentum is transferred from one particle to another. This causes a sole quark (or gluon) to scatter away from the collision vector, and as it travels, new hadrons spring up around it. This results in the detection of cones of high-momentum particles, which are called jets. While there is an overwhelming amount of empirical evidence to support the confinement hypothesis, a mathematical proof within QCD is still sought.

2.2.3.2 Asymptotic Freedom

In physics, the strength of the interaction between two particles is determined by a coupling parameters, and the dependence of this coupling on the energy scale is described by beta functions:

$$\beta(g) = \frac{\delta g}{\delta log(\mu)}, \tag{2.3}$$

where g is the coupling parameter and μ is the energy scale. Specific to QED, the coupling parameter is called the fine structure constant, given the symbol α, and at low energy determined to be

$$\alpha(\mu_0) = \frac{e^2}{4\pi\epsilon_0\hbar c} \approx \frac{1}{137}, \tag{2.4}$$

where e is the charge of the electron, ϵ_0 is the permittivity of free space, $\hbar$ is Plank's reduced constant, and c is the speed of light. The behavior of the coupling parameter can be described as an expansion of the β function in α:

$$\beta(\alpha) = \frac{\delta\alpha}{\delta \ln \mu} = \frac{2\alpha^2}{3\pi} + \mathcal{O}(\alpha^3). \tag{2.5}$$

Now, solving the differential equation from Eq. 2.5, one finds

$$\alpha(\mu) = \frac{\alpha(\mu_0)}{1 - \frac{\alpha(\mu_0)}{3\pi} \ln \frac{\mu^2}{\mu_0^2}}. \tag{2.6}$$

As the energy scale increases, which corresponds to a decrease in distance between the coupled objects, α increases, meaning that QED coupling becomes stronger with an increasing energy scale, and, therefore, shorter distances.

Turning to QCD, the beta function is:

$$\beta(\alpha) = -\frac{11C_A - 2n_f}{12\pi}\alpha^2 + \mathcal{O}(\alpha), \tag{2.7}$$

where $C_A = 3$, the number of quark colors, and n_f is the number of quark flavors. Unlike QED, QCD shows a *negative* β function, which means that coupling in QCD is the inverse of QED: as the energy scale increases, the coupling strength decreases. This leads to the following behavior of the strong force coupling constant:

$$\alpha_s(\mu) = \frac{2\pi}{(11C_A - 2n_f)\ln(\mu/\Lambda_{QCD})}, \tag{2.8}$$

where Λ_{QCD} is an experimentally determined term called the QCD scale that is used to assess different QCD regimes[8]. Intriguingly, this relationship shows that as μ goes to infinity, the coupling constant approaches zero. This feature, first described by Wilczek, Gross, and Politzer in 1973 [22, 23], is known as asymptotic freedom. This property implies that at high enough temperatures, the normally confined colored particles will move freely, deconfined. This finding was significant enough that the responsible scientists received a Nobel Prize in 2004 for their work. In fact, since 1973, an entire field has been dedicated to producing and thoroughly understanding

[8] As an example of different regimes, it is generally accepted that at scales much greater than Λ_{QCD}, the coupling constant is weak enough that perturbative calculations can describe aspects of QCD.

the properties of this predicted state of a deconfined colored medium. The field is ultra-relativistic nuclear physics, and the exotic phase of matter is called the quark-gluon plasma, which is described in detail in the following section.

2.3 The Quark-Gluon Plasma

Prior to the discovery of asymptotic freedom, Rolf Hagedorn observed a relationship in experimental data between baryon density and mass, which he described with

$$\rho(m) = f(m) \exp(m/T_H). \tag{2.9}$$

His interpretation was that there was a maximum temperature (T_H) at which matter could exist, and any additional energy added to a system at the maximum temperature would produce additional hadrons. The experimental data suggested $T_H \approx 175$ MeV [24].

After asymptotic freedom was proposed, Nicola Cabibbo and Giorgio Parisi argued that T_H was not the maximum temperature of matter, but instead the temperature at which a phase transition from confined to deconfined nuclear matter occurred. In their paper [25], the authors introduced the first version of the QCD phase diagram, which is presented in Fig. 2.3. In the authors' own words, the diagram shows a "Schematic phase diagram of hadronic matter. ρ_B is the density of baryonic number. Quarks are confined in phase I and unconfined in phase II."

The unconfined matter in phase II eventually became known as the quark-gluon plasma, and since it was first posited, scientists have sought to create and

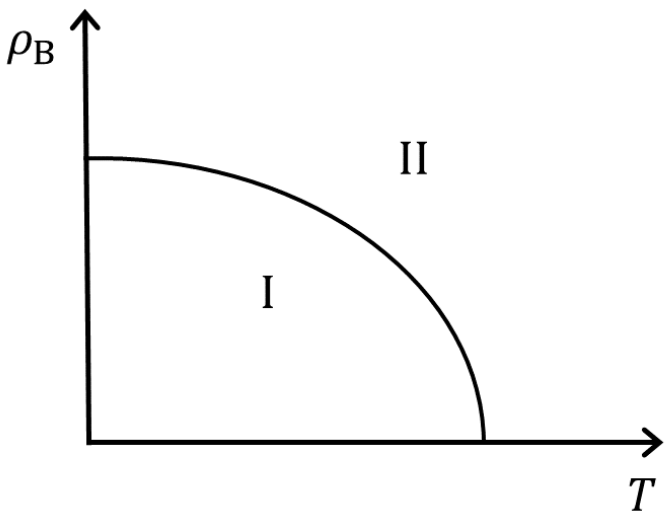

Figure 2.3: The baryon density versus Temperature nuclear matter phase diagram introduced by Cabibbo and Parisi. Confined hadronic matter exists in the area labelled I, whereas deconfined matter is proposed to area II [25].

characterize this exotic form of matter. The basic method of creating a QGP is straightforward: heat nuclear matter above T_H. To a nuclear physicist, T_H is not a maximum temperature, but a critical temperature, notated as T_c, which marks the phase transition between confined nuclear matter and the QGP. To reach the T_c in the laboratory, atomic nuclei must be accelerated to relativistic speeds and collided. These types of experiments, known as heavy-ion collisions, are the basis for the field of ultra-relativistic nuclear physics.

2.3.1 Heavy-Ion Collisions

For the description of how a QGP is produced by a heavy-ion collision, consider the model put forth by James Bjorken [26]. The space-time evolution sketched out by Bjorken begins with the assumption that there is a "'central-plateau' structure for particle production as a function of the rapidity variable." Rapidity, y, is a common

parameter in collider experiments because it is relativistically additive, defined as

$$y = \frac{1}{2} \ln \left(\frac{E + p_z c}{E - p_z c} \right), \tag{2.10}$$

where p_z is a particle's longitudinal momentum with respect to the beam direction and c is the speed of light. Particles that have a large transverse momentum (p_{T}) and small p_z have rapidity approaching zero. Those with high p_z have rapidities approaching either positive or negative infinity, depending on the direction relative to the beam. In general terms, rapidities near zero are considered "mid" or "central" rapidity. This assumption of a central-rapidity plateau ensures that the space-time evolution of the created system is boost-invariant, allowing us to assume that the thermodynamic variables of our system depend only on τ, the proper time, defined as

$$\tau = \sqrt{t^2 - z^2}, \tag{2.11}$$

where t is the time since the nuclei overlapped and z is distance from the point of the collision.

A collision evolves as follows. Two nuclei approach each other as highly Lorentz-contracted disks and collide at $t = z = 0$. This is shown as the intersection of the axes in Fig. 2.4. As the disks recede from the collision, they bring with them the initial baryons within the nuclei and leave behind a highly energetic system at the point of collision. If one assumes N nucleons were collided, the energy

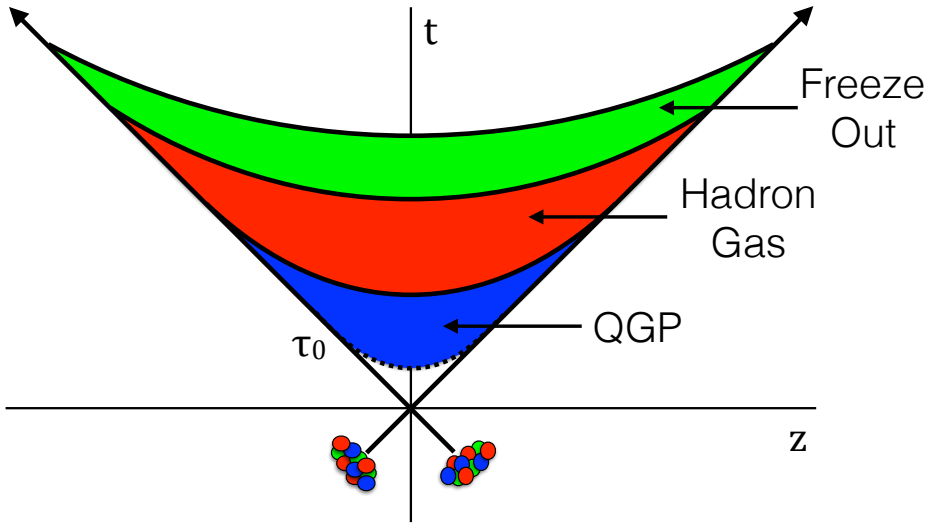

Figure 2.4: Evolution of a heavy-ion collision in the time and space dimensions. The dashed line indicates τ_0.

density (ϵ) of the system is

$$\epsilon = \frac{N}{\mathscr{A}} \frac{d\langle E \rangle}{dy} \frac{1}{t}. \tag{2.12}$$

Bjorken estimated $d\langle E \rangle / dy \approx 1.8$ GeV at Super Proton Synchrotron energies and calculated $N/\mathscr{A}$ as the number of incident nucleons per unit area, which is based on the number of nucleons colliding (A):

$$\frac{N}{\mathscr{A}} = \frac{A^{1/3}}{4.5 \text{ fm}^2}. \tag{2.13}$$

Assuming thermal equilibrium is reached at a time $\tau_0 \sim 1$ fm/c, the initial energy density of a system of particles produced in a heavy-ion collision is calculated as $\epsilon_0 \approx 2 - 20$ GeV/fm^3. In Fig. 2.4, τ_0 is labelled and indicated as the dashed line.

If the initial energy density is high enough, a QGP will form, and then undergo a longitudinal expansion that cools the system. Bjorken derived this hydrodynamic

expansion based on the system's energy density and pressure (p):

$$\frac{d\epsilon}{d\tau} = -\frac{(\epsilon + p)}{\tau}. \tag{2.14}$$

This leads to a decrease in the energy density and temperature of the system with $\tau^{-1/3}$. If a QGP is indeed formed, this phase is represented as the blue area in Fig. 2.4.

After the initial longitudinal expansion, when the size of the system has expanded to roughly the size of the colliding nuclei, the system will begin to experience expansion in three dimensions. As the system continues to expand and cool, the temperature approaches T_c, and a rapid transition to a confined state is expected, forming a "hadron gas." In this phase, the hadrons continue to interact, expand, and cool. Eventually, freeze-out occurs, where the rate of expansion is larger than the rate of particle interaction, local thermal equilibrium is lost, and the particles continue unabated until they reach a detector. Bjorken estimates time from collision to freeze-out lasts no more than $\tau \sim 5 - 10$ fm/c.

In Fig. 2.5, the evolution of a heavy-ion collision is shown within the QCD phase diagram. Nuclear matter is collided in particle accelerators like RHIC or the Large Hadron Collider (LHC), creating an extremely high temperature system. A less obvious consequence is a decrease in baryon potential from a value of approximately 1 GeV (the mass of a nucleon) in "normal" nuclear matter to nearly zero, but the reader should keep in mind that in Bjorken's model, the original baryons recede from the collision point and what is left behind is an energetic ball of quarks

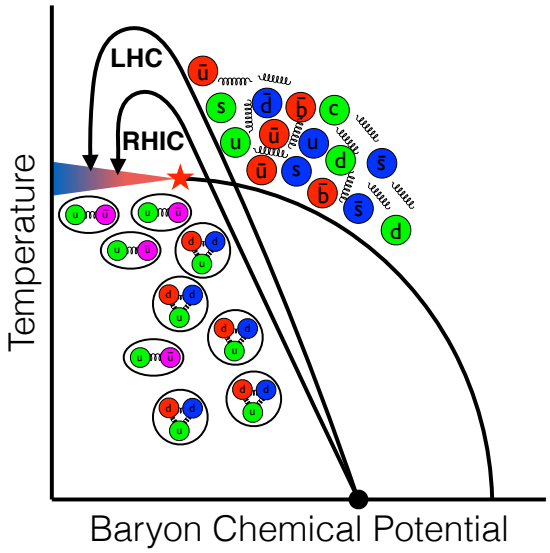

Figure 2.5: The QCD phase diagram, with curves showing the evolution of a heavy-ion collision at RHIC and the LHC.

and gluons. The LHC, with its higher collision energies, produces a higher temperature system with a lower baryon potential than is achievable at RHIC. These collisions produce a QGP that then expands and cools, eventually forming a hadron gas. The red star in the figure represents a hypothetical critical point that marks where a first order phase transition between confined and deconfined matter ends. Identification of this point through the RHIC beam energy scan is an active area of research, though it is outside the scope of this thesis [27, 28].

2.3.1.1 Collision centrality

In Bjorken's model, the calculations were performed assuming a complete overlap of colliding nuclei. In reality, a "central" collision like this is rare. A nucleus has a finite size, and so the area of overlap of two colliding nuclei varies between collisions. This experimental variable is called centrality, and is shown in Fig. 2.6. The

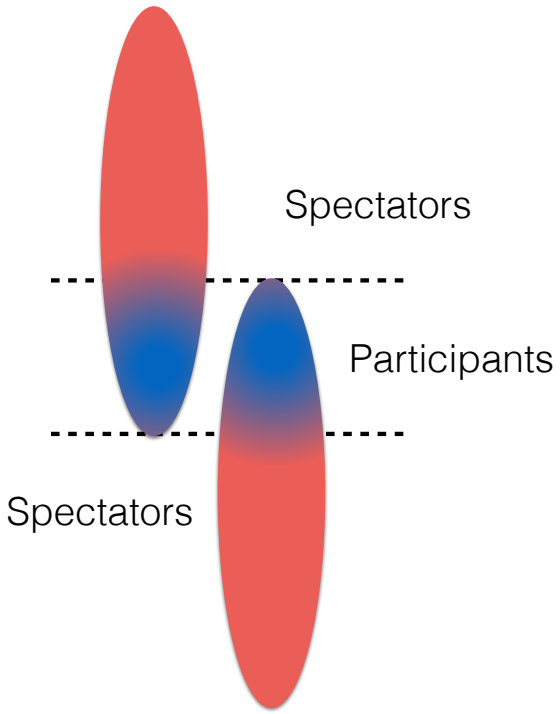

Figure 2.6: A nuclear collision will not necessarily have complete overlap, leaving some nucleons as participants, while those that don't collide are spectators.

nucleons that overlap and actually participate in the collision are called participants, whereas those that do not collide are called spectators. Centrality is presented as a percentage, as in "the $0-5\%$ most central collisions," referring to the most overlapping 5% of collisions. This is determined based on the multiplicity of particles or the amount of energy deposited in a detector, where higher centralities produce higher multiplicities and energies. Collisions with less overlap are deemed "peripheral." One can imagine the most peripheral collision to have only one participating nucleon from each nuclei, mimicking a proton-proton (pp) collision. The most extreme peripheral collisions, dubbed ultra-peripheral collisions, actually do not directly collide, and interact only through the electromagnetic force as two nuclei pass in very close proximity to one another, but do not actually overlap.

As shown in Eq. 2.12, the initial energy density of a collision is dependent on the number of colliding nucleons, N, meaning the initial conditions of a collision system change with centrality. This allows physicists to define centrality bins in order to study the QGP at it evolves from initial collisions with varying energy densities. In addition to centrality, several terms may be used throughout this thesis to describe the initial condition of the system, including N_{part}, which is a calculation of the number of participants, and N_{coll}, which accounts for the possibility that one nucleon could collide with several other nucleons within the larger nuclear collision. These terms are calculated using a widely accepted method called the Glauber Model [29].

2.3.2 Characterizing the QGP

In general, the characterization of the system created by a heavy-ion collision can be broken into two different regions: *soft probes*, which measure the behavior of the bulk of the particles created in the collision, and *hard probes*, which are relatively rare, higher momentum particles. The bulk of particles in a heavy-ion collision are created in the wake of the collision, as proposed by Bjorken, followed by an expansion, cooling, and phase transition. These particles are low-momentum and are said to be "soft." Soft probes are those that characterize the collective behavior of this created medium. In addition to the creation of soft particles, a direct parton-parton collision may occur, resulting in a large transfer of momentum and the creation of a particle that can travel through the created medium. These type of high-momentum

particles are the hard probes, and their interaction with the medium can provide valuable insight into the system's properties. The following descriptions of various probes of the QGP are not meant to be fully comprehensive, but will present a few of the most significant measurements performed by experiments at RHIC and the LHC.

2.3.2.1 Soft Probes

One common way of exploring the bulk behavior of the matter created in a heavy-ion collision is to measure the azimuthal anisotropy in the expansion of the system. The system's "anisotropic flow" is a description of how the system collectively expands, quantified by the Fourier coefficients (v_n) of the particle distribution:

$$\frac{dN}{(d\phi - \Psi_R)} = \frac{1}{2\pi}\left(1 + \sum_{n=1}^{\infty} 2v_n \cos(n(\phi - \Psi_R))\right), \tag{2.15}$$

where ϕ is the azimuthal angle of a particular particle and Ψ_R is the angle between the reaction plane of the collision, defined as the plane that bisects the two colliding nuclei and shown in Fig. 2.7, and the $X - Y$ axis of the detector. This Fourier expansion was proposed by Voloshin and Zhang [30] and a method for calculating the event reaction plane was developed by Ollitrault [31].

One can imagine two possible scenarios for the collective behavior of the system: either the system is a weakly interacting, gas-like substance that has very little collective behavior and therefore very little flow (isotropic expansion, characterized by small values of the Fourier coefficients), or the system is a strongly interacting,

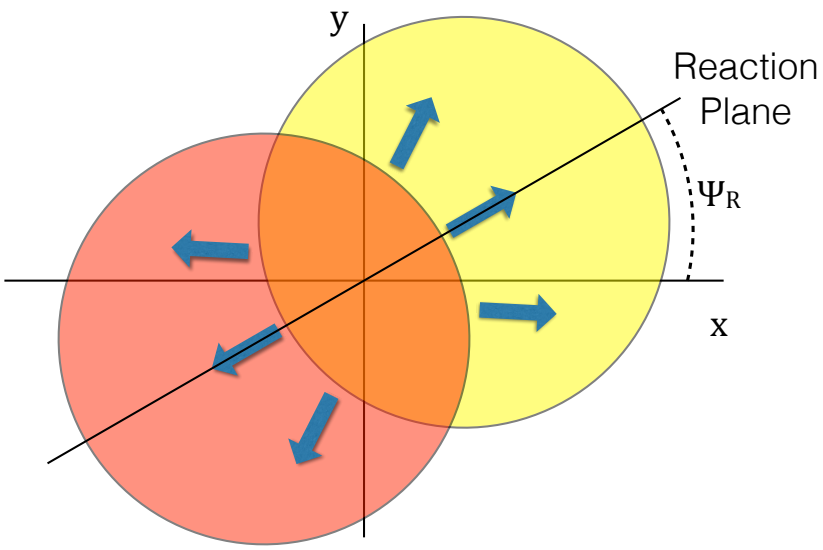

Figure 2.7: Pressure gradients in a heavy-ion collision.

liquid-like substance, with significant flow. Prior to the experiments at RHIC, the QGP was expected to be a system of weakly interacting partons, but early results from RHIC measured a significant value for the second order flow harmonic, v_2, indicating a strongly interacting system [32]. The measured flow could be modeled well using ideal hydrodynamics, suggesting the system rapidly thermalizes and behaves like an ideal fluid of interacting, yet unbound, quarks. The expansion of the system is a collective behavior based off the pressure gradients from the initial geometry of the collision [33]. This is depicted in Fig. 2.7, where the arrows represent the direction of expansion along the pressure gradient. The large measured flow was an early surprise in the experimental study of the QGP, and extensive studies are still being performed to measure other orders of flow harmonics, as well as the flow of specific particles, like quarkonia. Quarkonia, the main interest of this thesis, are mesons made of heavy quark-antiquark pairs and will be discussed in detail in Ch. 3. The relevance of quarkonia to this thesis, however, is not within the realm of soft

probes, but to exploit their properties as hard probes of the QGP.

2.3.2.2 Hard Probes

The commonality between Rutherford's gold foil experiment and the deep-inelastic experiments at SLAC that discovered quarks are that the target in each experiment was probed by a high energy particle. Rutherford used an alpha particle to discover the atomic nucleus, while the scientists at SLAC used electrons to probe the internal structure of protons. In an ideal scenario, an equivalent experiment would be to use a high energy particle beam to probe the properties of the QGP, but this is impossible due to the ephemeral nature of the QGP. However, in a nuclear collision, some partons can collide with other partons, resulting in a high momentum transfer and creation of new particles alongside the production of the QGP. The particles made in these hard interactions are produced in the very first instants of the nuclear collision, and can therefore be used as direct probes of the QGP. Hard interactions are expected to roughly scale[9] with N_{coll}, and so comparisons of the behavior of hard particles in heavy-ion collisions can be compared to the behavior in a basic *pp* collision, where no QGP is expected to form. Any modification can be attributed to interaction with the QGP, allowing scientists to better understand exactly how the QGP behaves

One of the hard scattering processes that can occur is the production of a jet: two partons can be produced back-to-back, with roughly equal, but opposite, momentum. As the partons travel away from the collision point, a cone of high

[9]There are some nuclear effects that must be considered that prevent a direct scaling.

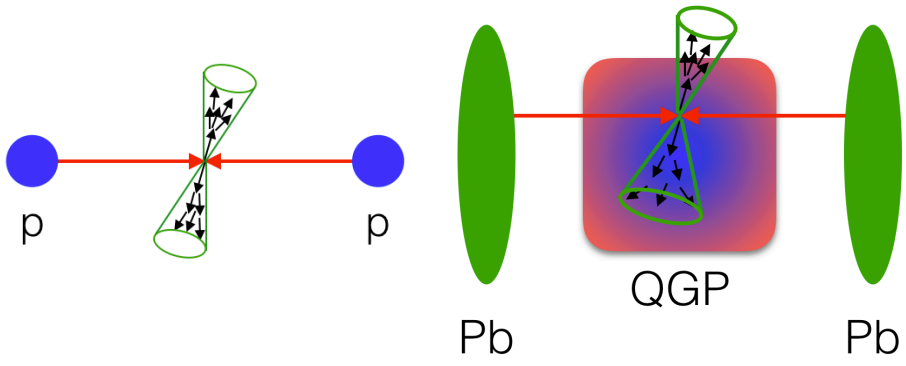

(a) (b)

Figure 2.8: A comparison of jets in a *pp* and PbPb collision.

momentum particles is produced. This cone of particles is called a jet, and when two jets are produced back-to-back, it is called a dijet event. Figure 2.8a shows an example of a dijet in an elementary *pp* collision. Dijets are exceptionally interesting probes of the QGP because it is possible that one of the jets travels through, and therefore interacts with, more of the QGP than the other jet [34]. This process is shown in Fig. 2.8b. Note that the jet going up passes through less of the QGP than the jet going down, and that the "up" jet has a smaller cone than the "down" jet, indicating that the "down" jet has been modified by the QGP. This behavior was first observed by the STAR Collaboration at RHIC, and was one of the first significant measurements suggesting the presence of a QGP [35].

A second type of hard probe of the QGP are quarkonia. The production of quarkonia and their importance in characterizing the QGP is the main theme of this thesis, and all the necessary background information will be presented in Ch. 3. For now, it must suffice to say that the various quarkonia particles have different dissociation energies, which leads to a sequential suppression of the quarkonia family in nuclear collisions, where the production of some quarkonia particles is more

suppressed than others.

2.3.3 QGP in small systems

Ideally, production of hard probes would exactly scale between *pp* and nucleus-nucleus (AA) collisions, allowing a direct comparison between the two systems. Unfortunately, the collision of partons within nuclei is more complex than the collision of partons in vacuo. A simplified version of the different collision systems at the LHC is presented in Fig. 2.9. The main tool of a nuclear physicist studying the QGP is a collision of two nuclei (indicated as "AA" in the figure). As has been discussed, these collisions are believed to create the QGP, which is characterized by its collective expansion and through its modification of probes like jets and the production of quarkonia. These effects, caused directly by the presence of the QGP, are thought of as "final-state effects." In collisions involving a nucleus, there are also initial-state effects, which arise from particle production within a cold nucleus, as opposed to in the vacuum surrounding a *pp* collision. These effects appear as modifications to the probes of the QGP, but are not actually caused by the QGP itself, and are referred to as cold nuclear matter effects. In order to differentiate initial- and final-state effects, proton-nucleus ("pA" in the figure) collisions are used. There is no QGP expected to be produced in these types of collisions, and so any differences between observables in *pp* and pA collisions *should* be attributable to these initial-state, cold nuclear matter effects.

Overall, the method of understanding the QGP was fairly straight forward: *pp*

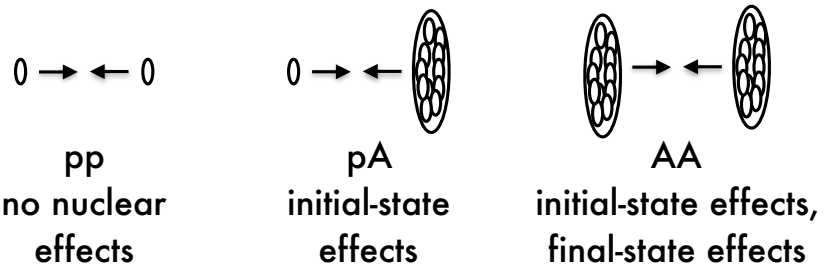

Figure 2.9: The three main collision systems at the LHC.

collisions would provide the base standard of all QGP probes, pA collisions would quantify initial-state effects, and then the properties of the QGP could be gleaned through AA collisions. Naturally, assuming such simple and clear-cut differences between the collision systems set up the field for a surprise, which presented itself in 2010 when CMS discovered that high multiplicity *pp* events seemingly exhibited collective behavior [36]. Collective behavior is thought to be a result of an interacting medium, so indications of its presence in pp, the simplest of the considered systems, was quite unexpected. After this discovery, and then the discovery of similar behavior in proton-lead (pPb) collisions [37], the most intriguing question for the field is not whether the QGP exists, but in *how small* of a system the QGP exists. In fact, while it is not a direct goal of the work contained in this thesis, the presented analysis of quarkonia production could potentially answer some questions about the behavior of such small systems.

Chapter 3: Quarkonium Physics

Quarkonia are bound states of a heavy quark and its anti-quark, $Q\overline{Q}$, comprised of the charmonium ($c\bar{c}$) and bottomonium ($b\bar{b}$) particles. There are numerous states of charmonium and bottomonium mesons, distinguished by their spin (S) and orbital angular momentum (L) quantum numbers, the sum of which gives the total angular momentum, $J = L + S$. Each state, notated with term symbols of the form $n^{2S+1}L_J$, where n is the primary quantum number, is considered a different particle, and given a specific name. The first quarkonium particle to be discovered was reported by two groups on the same day in 1974. One group, from Brookhaven National Lab, dubbed the meson the J [38], the other, from SLAC, called it the ψ [39], and so the particle came to be known as the J/ψ. This discovery confirmed the existence of the charm quark. Two weeks later, SLAC reported the discovery of a second $c\bar{c}$ resonance - the $\psi(2S)$ [40]. The J/ψ, with a mass of 3.097 GeV/c^2, has a total angular momentum $J = 1$, and was therefore assigned the term symbol 1^3S_1. The higher order $\psi(2S)$, identified by the term symbol 2^3S_1, is found at a slightly higher mass, 3.686 GeV/c^2. In 1977, the $\Upsilon(nS)$ ($b\bar{b}$) meson was found at Fermilab as an enhancement in the dimuon mass spectrum of pA collisions around

Table 3.1: Some quarkonia particles along with respective term symbols, names, and masses. Note that the $\chi_b(3P)$ has not yet been confirmed to exist as a triplet. [44]

Notation		Charmonium		Bottomonium	
$n^{2s+1}L_J$	J^{PC}	Particle	Mass (GeV/c^2)	Particle	Mass (GeV/c^2)
1^3S_1	1^{--}	J/ψ	3.097	$\Upsilon(1S)$	9.460
2^3S_1	1^{--}	$\psi(2S)$ ($\psi(2S)$)	3.686	$\Upsilon(2S)$	10.023
2^3S_1	1^{--}	-	-	$\Upsilon(3S)$	10.355
1^3P_0	0^{++}	$\chi_{c0}(1P)$	3.415	$\chi_{b0}(1P)$	9.859
1^3P_1	1^{++}	$\chi_{c1}(1P)$	3.511	$\chi_{b1}(1P)$	9.892
1^3P_2	2^{++}	$\chi_{c2}(1P)$	3.556	$\chi_{b2}(1P)$	9.912
2^3P_0	0^{++}	-	-	$\chi_{b0}(2P)$	10.232
2^3P_1	1^{++}	-	-	$\chi_{b1}(2P)$	10.255
2^3P_2	2^{++}	-	-	$\chi_{b2}(2P)$	10.268
3^3P_0	0^{++}	-	-	$\chi_{b0}(3P)$	?
3^3P_1	1^{++}	-	-	$\chi_{b1}(3P)$	10.512
3^3P_2	2^{++}	-	-	$\chi_{b2}(3P)$	?

9.5 GeV/c^2, confirming the existence of the bottom quark.[1] [43]. Some of the discovered quarkonia particles are listed in Table 3.1. The particles with $L = 0$ are called "S-wave" states, and those with $L = 1$ as "P-wave" states, referring to the spectroscopic notation for angular momentum.

Along with the term symbol, a second identifying symbol, J^{PC}, is included in the chart. Again, total angular momentum is reported as J, now noted with the superscripts P (parity) and C (charge conjugation). Parity is a description of a global symmetry (a symmetry over all points in space-time under consideration) that involves a transformation of a matrix of coordinates, using a determinant of -1 so that the spatial coordinates (x, y, z) are transformed to $(-x, -y, -z)$. A charge conjugation transformation changes the sign of all the quantum numbers of a particle; it transforms a particle into its antiparticle. The eigenvalues of parity

[1] To complete the history of quark discoveries, the top quark was discovered in 1995 at Fermilab [41, 42]. Because of it's large mass, it is not expected to form a $t\bar{t}$ quarkonium.

and charge conjugation are limited to ± 1, defined by $P = (-1)^L$ and $C = (-1)^{L+s}$. In strong interactions, parity and charge conjugation are quantum numbers that must be conserved.

The charmonium and bottomonium spectra are presented in Fig. 3.1 and 3.2. Focussing first on the charmonium spectrum, there are five particles - the two S-wave and three P-wave states introduced in Table 3.1. The S-wave particles are identified at CMS through the experimentally clean dimuon channel $\psi(nS) \to \mu\mu$. The P-wave χ_c particles are identified through their radiative decay through a J/ψ: $\chi_{cJ} \to \mathrm{J}/\psi + \gamma$. Overall, approximately 67% of *prompt* J/ψ particles are directly produced, $8.1 \pm 0.3\%$ come from $\psi(2S)$ and the remaining $25 \pm 5\%$ come from P-wave decays, while the $\psi(2S)$ is not expected to suffer any feed-down effects [45]. The introduction of the term "prompt" requires explanation - a charmonium has a very fast decay, on the order of 10^{-21} seconds or faster, yet there are some charmonia that appear to last substantially longer, on the order of 10^{-12} seconds [44]. These long-lived charmonia are called "non-prompt" and are actually the decay products of longer lived B-mesons. Because non-prompt charmonia are longer lived, the observed charmonium decay vertex (called the secondary vertex) is displaced from the primary vertex, and thus it is possible to distinguish between prompt and non-prompt charmonia.

The bottomonium family contains several more excited states than the charmonium, meaning the effects of feed-down are much more complicated, as is displayed in Fig. 3.2. Other than the increased number of decays, the spectrum is analogous to the charmonium spectrum, where the excited S-wave states feed-down to the

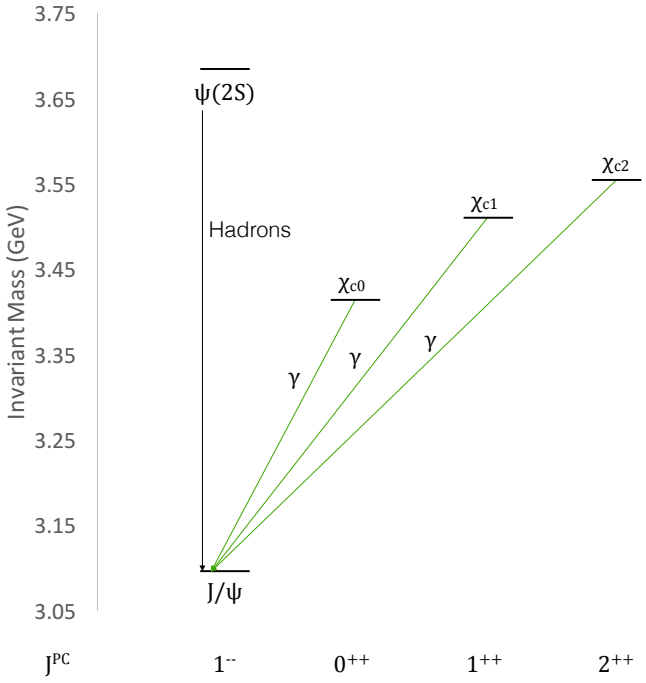

Figure 3.1: The charmonium spectrum.

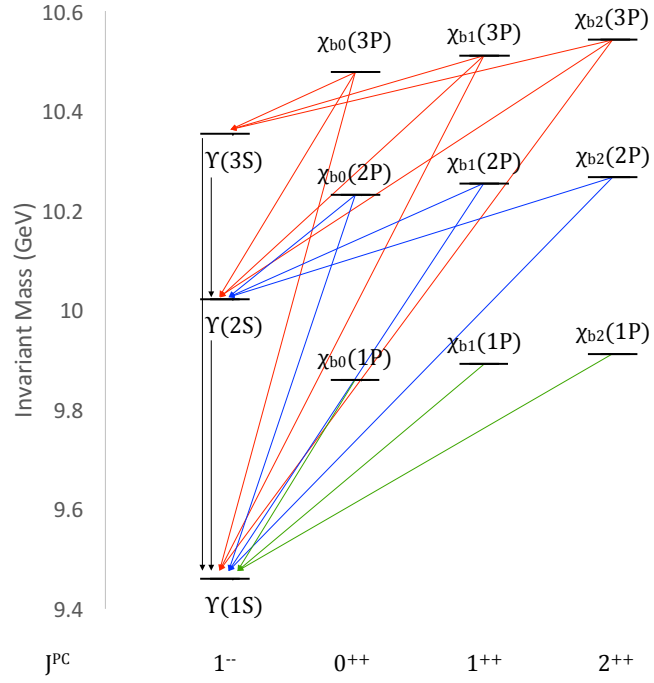

Figure 3.2: The bottomonium spectrum.

lower energy states, and the P-wave particles can decay by producing an S-wave state along with a photon. One important difference is that there is no significant non-prompt contribution in the bottomonium spectrum. Recently, the LHCb collaboration at CERN provided detailed feed-down fraction measurements from the P-wave to the S-wave states. The fractions of S-wave state produced as decays of P-wave states are presented as $R^{\chi_B(mP)}_{\Upsilon(nS)}$ in Fig. 3.3, revealing that up to $\sim 35\%$ of the $\Upsilon(1S)$ and $\Upsilon(2S)$ are indirectly produced through P-wave states, and that even the $\Upsilon(3S)$, with only the $\chi_{bJ}(3P)$ states available to feed-down into it, is only $\sim 60\%$ directly produced [46]. Without a clear idea of the feed-down fractions within the bottomonium family, interpretation of quarkonia probes of QCD and the QGP, as described in Sec. 3.1, remains difficult.

3.1 Quarkonia as Probes

The Hydrogen atom has provided scientists with a simple two-body QED system, allowing for the development of a thorough understanding how an electron and a proton are bound together. Seeking to gain similar advances within QCD, physicists have turned to an analogous system: bound quark-antiquark pairs. More specifically, because of the simplicity provided by a non-relativistic system, physicists are interested in quarkonia, whose heavy mass and slow relative velocity ($v^2 \approx 0.3$ for J/ψ, $v^2 \approx 0.1$ for Υ) lends to a non-relativistic nature [47]. The basic production mechanism of quarkonia is still not settled, and by studying how quarkonia are formed, particle physicists can probe aspects of hadron formation within QCD.

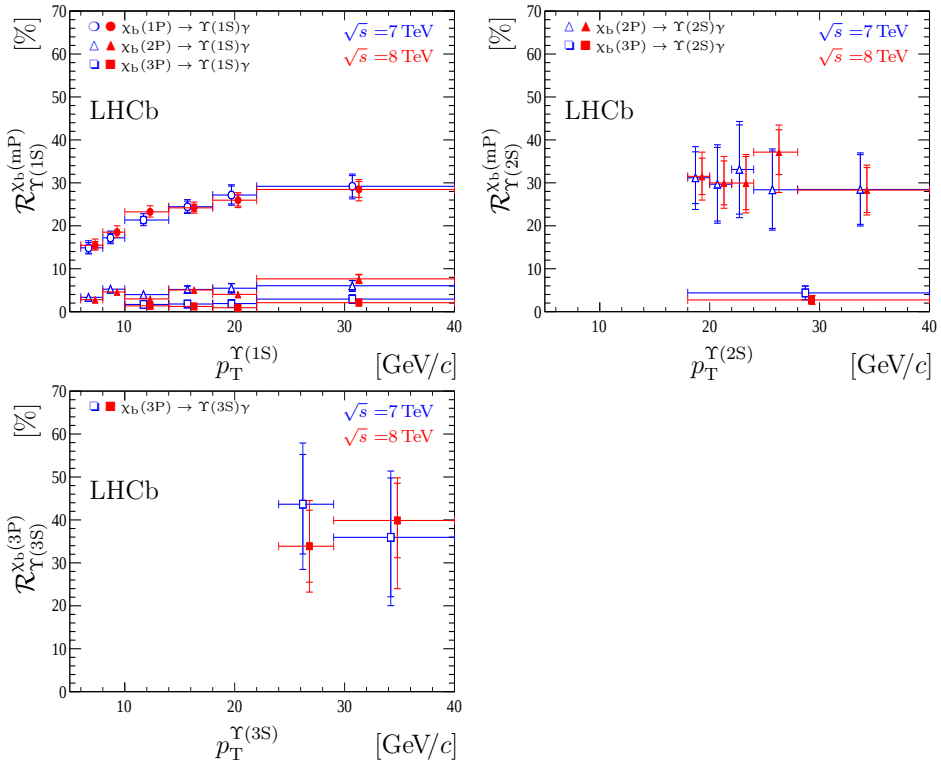

Figure 3.3: The feed-down fractions ($R^{\chi_B(mP)}_{\Upsilon(nS)}$) measured by LHCb against p_{T} of the $\chi_{bJ}(nP)$ to the $\Upsilon(1S)$ (top left), $\chi_{bJ}(nP)$ to the $\Upsilon(2S)$ (top right), and $\chi_{bJ}(3P)$ to the $\Upsilon(3S)$ (bottom) [46].

Nuclear physicists[2] use quarkonia in a different manner: quarkonia, created in the first instants of a nuclear collision, are hard probes of the QGP. Individual quarkonia have different binding energies, and therefore these particles "melt" at different energy densities within the QGP, producing a sequential suppression pattern, where some quarkonia are more suppressed than others. The nuclear physicist, because of the higher complexity of nuclear collisions, must not contend only with post-collision effects, must also be aware of how cold nuclear matter effects could alter quarkonia measurements. In fact, one may even question whether the production mechanism remains constant between *pp* and AA collisions. Here lies the crux of this thesis - is there a change in basic production mechanism between collision systems? This thesis provides the first experimental steps in an attempt to answer this question, beginning with a look into the production mechanism in *pp* collisions. Both the particle and nuclear physicist are set to gain from this analysis: for the former, a confirmation or refutation of a basic assumption could be provided, and for the latter, additional confidence could be placed on the interpretation of quarkonia suppression patterns. These two topics will be addressed in the following sections. Section 3.1.1 reviews the current state of quarkonia measurements in nuclear collisions and Sec. 3.1.2 discusses the quarkonium production mechanism and how it is experimentally verified.

3.1.1 Quarkonia Measurements as Probes of the QGP

In 1986, Hatz and Matsui argued that the suppression of quarkonia was a possible signature of QGP formation, due to Debye screening of the quark color charge

[2] And, in special circumstances, nuclear chemists.

during quarkonia production [48]. In a hadron-hadron collision, hard interactions produce $Q\overline{Q}$ pairs that subsequently form a bound quarkonia, the details of which are presented in Sec. 3.1.2. In the more complicated nuclear collisions, the $Q\overline{Q}$ pair evolves in a hot nuclear matter environment, which, depending on the temperature of the medium, should suppress quarkonia production. Quarkonia suppression in the QGP can be understood by an investigation into quarkonia binding energies through a description of the interaction potential of a $Q\overline{Q}$ pair:

$$V(r) = \sigma r - \alpha_{eff} r, \tag{3.1}$$

where σ represents the string tension, which decreases with increasing temperature until $\sigma = 0$ at T_c, the temperature at which the deconfinement of the medium is achieved, r is the radius of the quarkonium, and α_{eff} is the interaction coupling of the pair. Matsui and Satz argued that for $T \geq T_c$ the potential is

$$V(r) = -\frac{\alpha_{eff}}{r} e^{-r/r_d(T)}, \tag{3.2}$$

where r_d is the temperature-dependent Debye screening radius. When $r_d > r$, the suppression through color screening can occur, which is shown in Fig. 3.4. In Fig. 3.4a, a quarkonium has formed in a vacuum, with no interference. In a QGP, depicted in Fig. 3.4b, there is an abundance of densely packed quarks, in which $r_d > r$, and therefore the pre-resonant $c\bar{c}$ pair is blocked from forming a bound meson.

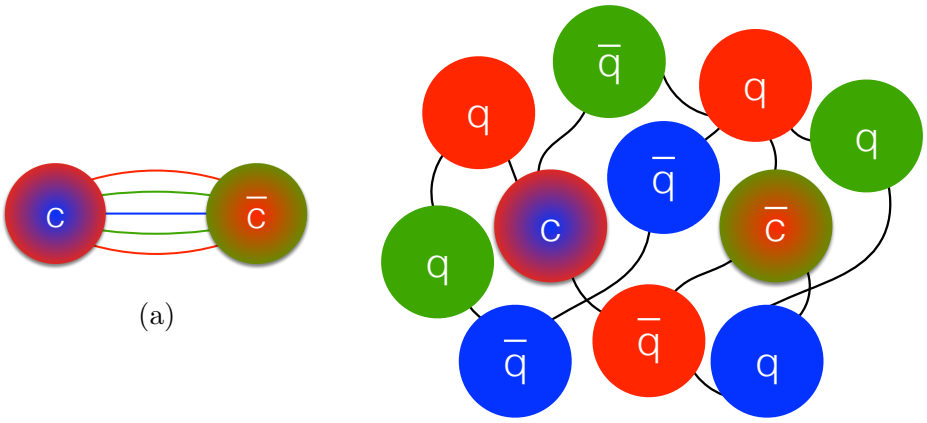

(a) (b)

Figure 3.4: On the left, a $c\bar{c}$ was created in a vacuum and formed a bound charmonium state. On the right, a $c\bar{c}$ pair was created in a nuclear collision that created a QGP. The densely packed state prohibited the $c\bar{c}$ pair from forming a bound charmonium state.

The Debye screening radius depends on the mass of the quark, m_Q, as well as the coupling of the quark pair, through the relation

$$r_d \propto \frac{1}{\alpha_{eff} m_Q}. \tag{3.3}$$

This dependence assures that heavier $Q\overline{Q}$ pairs survive higher energy densities due to their higher binding energies, meaning that one would expect suppression of the heavier bottomonia to be less than that of the lighter charmonia. The dependence on the strength of the quark coupling indicates that the radial excitations of the J/ψ and $\Upsilon(1S)$ (i.e. the $\psi(2S)$, $\Upsilon(2S)$, $\Upsilon(3S)$, and various χ particles) will be more suppressed. This means that the suppression of quarkonia depends on the energy density of the medium, and therefore the expectation is for suppression to happen sequentially, with $\Upsilon(1S)$ being the least suppressed due to its high dissociation tem-

Table 3.2: The binding energies (ΔE) and radii (r_0) of the quarkonia particles mentioned throughout this thesis [50].[3]

State	$\Upsilon(1S)$	$\chi_b(1P)$	J/ψ	$\Upsilon(2S)$	$\chi_b(2P)$	$\Upsilon(3S)$	$\chi_c(1P)$	$\psi(2S)$
ΔE (GeV)	1.10	0.67	0.64	0.54	0.31	0.20	0.20	0.05
r_0 (fm)	0.28	0.44	0.50	0.56	0.68	0.78	0.72	0.90

perature [49]. The amount of suppression increases as the binding energy decreases, giving the following sequence from least to most suppressed: $\Upsilon(1S)$, $\chi_b(1P)$, J/ψ, $\Upsilon(2S)$, $\chi_b(2P)$, $\Upsilon(3S)$, $\chi_c(1P)$, $\psi(2S)$ [50]. The quarkonium radii and binding energies are listed in Table 3.2. This suppression process is colloquially referred to as quarkonia "melting," and quarkonia can be used as a sort of thermometer to gauge the temperature of the QGP.

Quarkonia suppression measurements are generally reported through a value called a nuclear modification factor, which measures the ratio of quarkonia production yield in heavy-ion collisions and the scaled yield in pp collisions at the same energy. The term is defined as

$$R_{AA} = \frac{\mathcal{L}_{pp}}{T_{AA} N_{MB}} \frac{\Upsilon(nS)|_{PbPb}}{\Upsilon(nS)|_{pp}} \frac{\epsilon_{pp}}{\epsilon_{PbPb}}, \tag{3.4}$$

where ϵ is an efficiency correction, $\mathcal{L}$ is the integrated luminosity, T_{AA} is the average nuclear overlap function (a calculation related to N_{part}, obtained using the Glauber Model), and N_{MB} is the number of events collected. A value less than unity indicates suppression. These values are differentiated over several variables to gain a full understanding of how the system behaves and how it affects quarkonium production. Possibly the most obvious parameter is the collision centrality, which allows for an

investigation of quarkonia suppression as the energy density of the system changes, but measurements against the quarkonium's kinematic values, p_{T} and rapidity, are important as well.

A natural start for discussing quarkonia suppression measurements is the J/ψ, which is produced in abundance at both RHIC and the LHC, and therefore is the most studied quarkonium. The first significant suppression result out of RHIC, from the PHENIX Collaboration, was a measurement of J/ψ R_{AA} in AuAu collisions at $\sqrt{s_{NN}} = 200$ GeV as a function of N_{part}, p_{T}, and rapidity [51]. Their main findings are presented in Fig. 3.5, which show R_{AA} decreases with centrality, with quarkonia less suppressed at mid-rapidity than at forward-rapidity. While the overall suppression was a highly anticipated signature of the QGP, the rapidity dependence was not. In fact, one would expect the reverse dependence, with more suppression at mid-rapidity, where the energy density is highest. Turning now to Fig. 3.6, R_{AA} measurements from ALICE in PbPb collisions at $\sqrt{s_{NN}} = 2.76$ and 5.02 TeV, which ensures much higher energy densities than those at RHIC, are shown [52]. Intriguingly, the R_{AA} measurements at ALICE show *less* suppression than the lower energy collisions at RHIC, with R_{AA} values at RHIC reaching nearly 0.2, but only approximately 0.6 at the LHC. Even at LHC energies, the $\sqrt{s_{NN}} = 5.02$ R_{AA} data is systematically larger than the $\sqrt{s_{NN}} = 2.76$ TeV value. This should seem counter-intuitive, as quarkonia suppression is predicated on higher energy densities *causing* suppression, yet here are results from two different experiments seemingly indicating the opposite. The explanation is actually qualitatively simple: at higher energy densities, greater numbers of charm quarks are created, and as the QGP cools, these

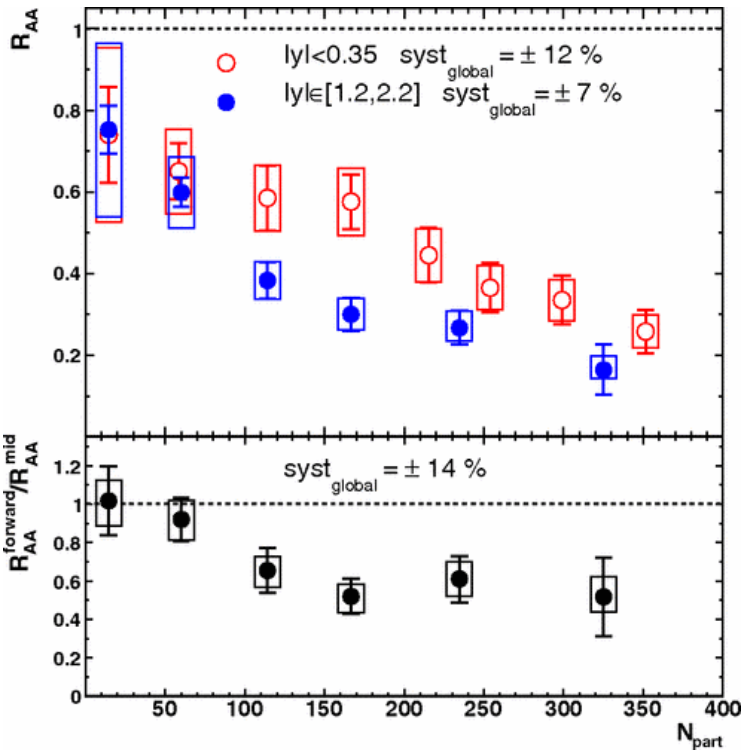

Figure 3.5: J/ψ R_{AA} in $\sqrt{s_{NN}} = 200$ GeV, shown in different rapidity ranges against centrality [51].

charm quarks come together to regenerate J/ψ particles. Of course, while simple to explain, J/ψ regeneration is an additional complication in the interpretation of suppression results. The $\psi(2S)$, owing to a much lower production yield than the J/ψ, due to both a lower production cross section and higher level of suppression, has only recently been measured in nuclear collisions. Yet it too suffers from an intricate interplay of suppressive and regenerative effects, and in fact, recent measurements from CMS have shown quite different R_{AA} trends from one run to the next, showing that at $\sqrt{s_{NN}} = 2.76$ TeV, there appears to be an enhancement of $\psi(2S)$ relative to the J/ψ that disappears at $\sqrt{s_{NN}} = 5.02$ TeV [53]. At the moment, these complexities preclude conclusive statements about the exact nature of suppression within the charmonium family.

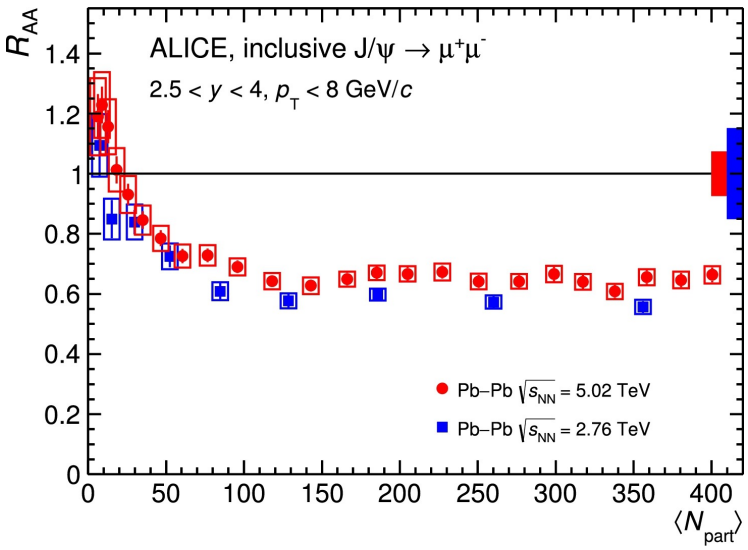

Figure 3.6: J/ψ R_{AA} in $\sqrt{s_{NN}}$ = 2.75 (blue) and 5.02 (red) TeV PbPb collisions, measured against N_{part} [52].

The bottomonium system, on the other hand, is expected to experience a much smaller degree of regeneration, and from this perspective, suppression measurements should be more straight-forward. In fact, perhaps the most spectacular[4] visualization of sequential quarkonia suppression is in Υ measurements from CMS, presented in Fig. 3.7. In this figure, the difference between the dimuon mass spectra in *pp* and PbPb collisions are compared. Figure 3.7a shows, from the left to right, three distinct peaks for the $\Upsilon(1S)$, $\Upsilon(2S)$, and $\Upsilon(3S)$. Comparing this to Fig. 3.7b, where the dashed line represents the *pp* spectrum scaled to the PbPb $\Upsilon(1S)$ peak, the suppression is immediately obvious. This measurement, taken at $\sqrt{s_{NN}}$ = 5.02 TeV, is quantified via R_{AA} values in Fig. 3.8. The red points, which represent the R_{AA} value of the $\Upsilon(1S)$, are clearly higher than blue $\Upsilon(2S)$ points, which is in turn higher than the green $\Upsilon(3S)$ points, which are actually so small that they are reported only as an upper limit at a 95% confidence level. Each set of data points

[4] In the words of Enrico Scomparin during his talk at Quark Matter 2017 [54].

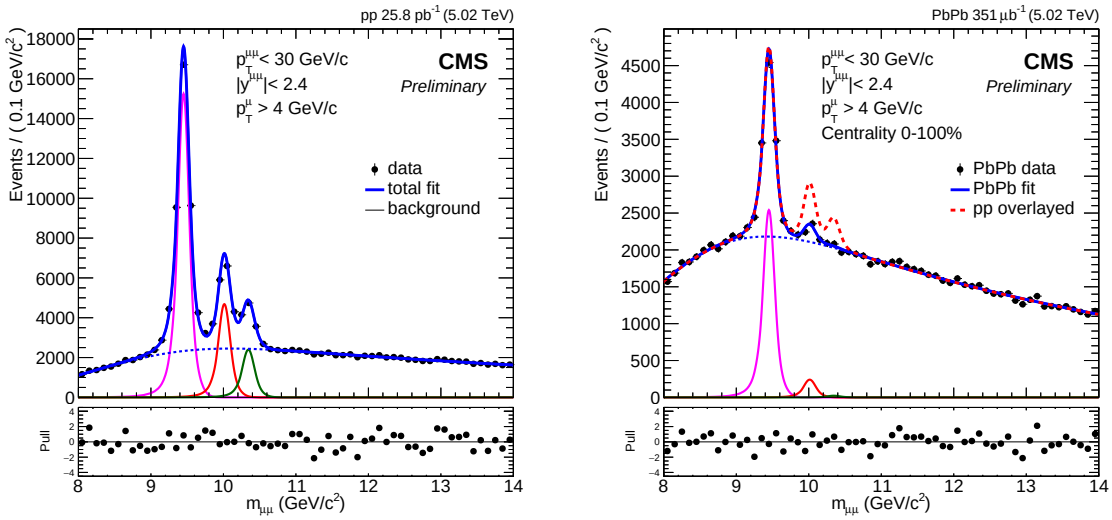

(a) (b)

Figure 3.7: The dimuon mass spectra in a) *pp* collisions, showing three distinct $\Upsilon(nS)$ peaks and b) PbPb collisions, where the dashed lines represent the the *pp* peaks scaled to match the $\Upsilon(1S)$, clearly showing sequential suppression [55].

generally falls with increasing centrality, as would be expected. This result is quite significant, clearly showing that the predicted sequential suppression within the Υ family.

Yet, the bottomonium family is not free from complications. The intricate feed-down structure means that interpretation of the suppression results is not trivial and requires precise measurements in basic *pp* collisions. Moreover, measurements of Υ states in *pp* and pPb collisions have shown curious dependencies. Take, for example, the result from CMS shown in Fig. 3.9, where ratios of excited state to ground state Υ yields are plotted against the number of particle tracks, which is an experimental observable that estimates the amount of energy created in a collision, and is generally referred to as "event activity." It is generally assumed that in the *pp* and pPb systems a QGP is not produced, and one would not expect the event

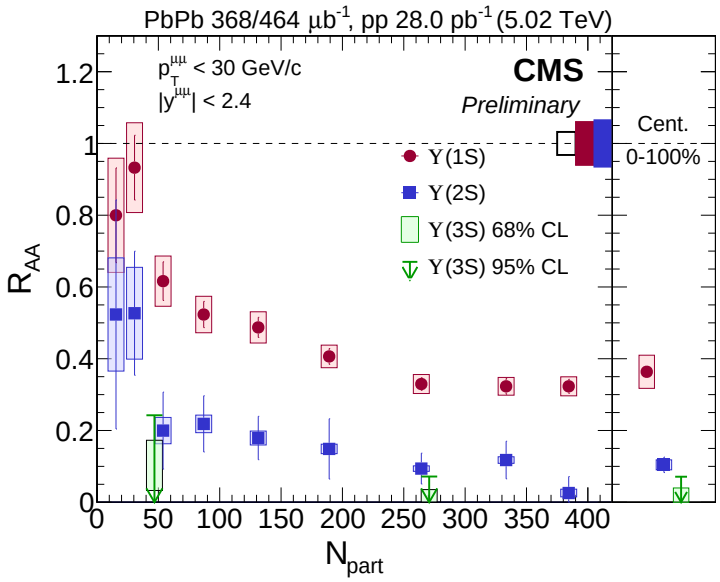

Figure 3.8: CMS measurement of sequential suppression of the Υ particles. The R_{AA} value decreases with centrality, and shows less suppression for the $\Upsilon(1S)$ (red) than the $\Upsilon(2S)$ (green). The $\Upsilon(3S)$ measurement (green) was reported as a 95% confidence level upper limit [56].

activity of a collision system to affect the production of one Υ state differently than the others, yet this result shows that excited Υ states are produced at lower rates than the $\Upsilon(1S)$ as the event activity increases.

There are at least two potential explanations for the noted dependence, either a QGP is forming in a *very* small system, or there is a change in the basic production mechanism of the Υ states as the environment surrounding its formation changes. Either of these explanations would be a significant finding, the former would challenge the notion of how one thinks of a QGP and how to create it, and the latter implies that a basic assumption about quarkonium production is incorrect, which in turn may imply that production between *pp* and PbPb collisions, thought to be consistent, may actually be changing. Considering the importance of quarkonia as a probe of the QGP, detailed studies of the effect of the surrounding environment on

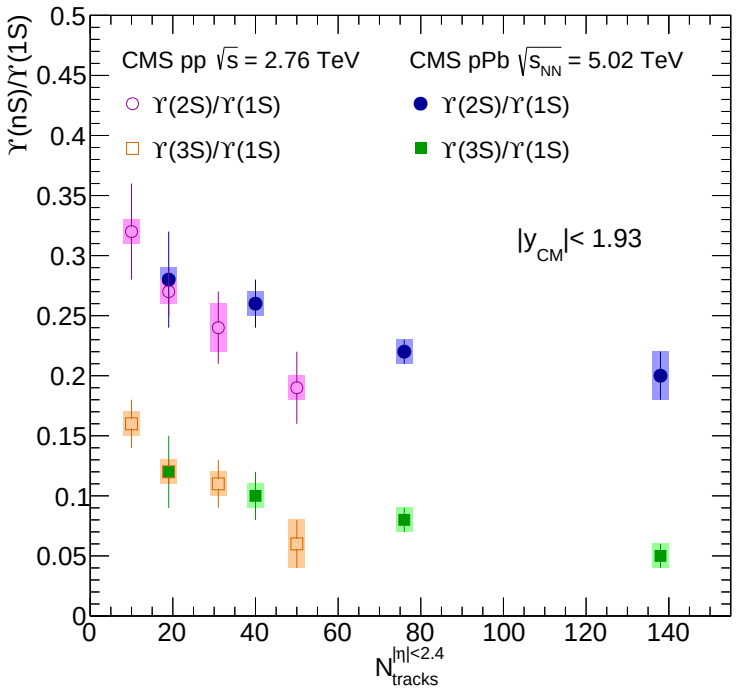

Figure 3.9: A CMS plot showing the ratio of excited ϒ to ground ϒ states against N_{tracks} in pp and pPb collisions [57].

basic quarkonium production must be undertaken. An introduction to quarkonium production is presented in Sec. 3.1.2, and then in Sec. 3.2, the details of quarkonium polarization, which is the main measurement presented in this thesis, will be established.

3.1.2 Quarkonia Production as a Probe of QCD

The currently accepted quarkonium production mechanism was introduced by Bodwin, Braaten, and Lepage in 1995 [58]. This approach uses non-relativistic quantum chromodynamics (NRQCD) and factorizes short-distance and long-distance QCD effects, which is only possible to do in quarkonia, which, unlike lighter mesons, can be treated non-relativistically. The short-distance effects are generally thought

to be reliably calculated using perturbative methods, but calculations for the long-distance effects have so far been fraught with challenges. By separating the processes, physicists are able to parametrize the short- and long-distance effects as they seek to gain a better handle on the formation of hadrons in general.

The factorization approach breaks quarkonia production into two steps: first a pre-resonant $Q\overline{Q}$ pair is produced, either as a color-singlet with L and S quantum numbers that match those of the bound state, or as a color-octet, potentially with different quantum numbers. The second step, distanced in both time and space from the first step, is the evolution of the unbound $Q\overline{Q}$ pair into the bound quarkonium, which, if necessary, occurs along with a change in L and/or S and color neutralization. The production is quantified as the quarkonium cross section (σ):

$$\sigma(\mathcal{Q}) = \sum_n \mathcal{S}[Q\overline{Q}(n)] \cdot \mathcal{O}^{\mathcal{Q}}(n). \tag{3.5}$$

The first term, $\mathcal{S}[Q\overline{Q}(n)]$, represents the momentum-dependent "short-distance coefficients" (SDCs) that describe the perturbative production of $Q\overline{Q}$ pairs in a specific quantum state n, where $n = {}^{2S+1}L_J^{[C]}$, with the color multiplicity notated as $C = 1, 8$. In the second term, $\mathcal{O}^{\mathcal{Q}}(n)$, the non-perturbative "long-distance matrix elements" (LDMEs) quantify the likelihood that a particular $Q\overline{Q}$ state evolves into a bound quarkonium. This process in portrayed in Fig. 3.10, showing the perturbative production of possibly colored $Q\overline{Q}$ pair and its non-perturbative evolution into a bound quarkonium.

In principle, the quarkonia can be produced through an infinite set of pre-

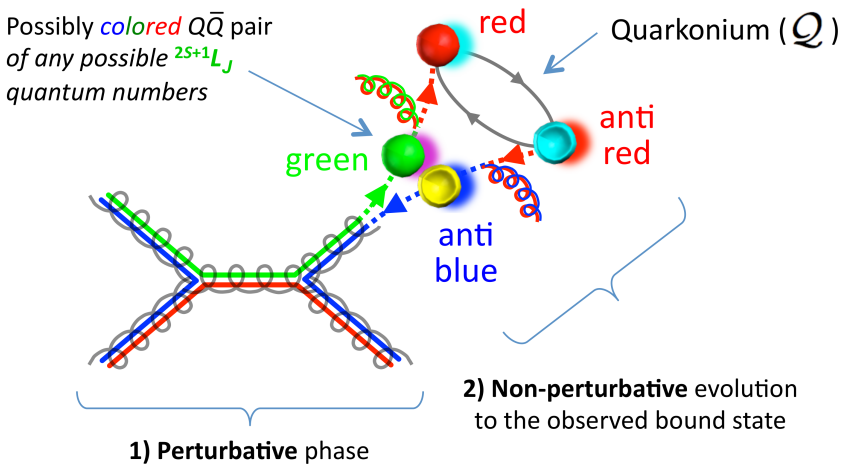

Figure 3.10: The factorized process of the production of a pre-resonant $Q\overline{Q}$ pair and subsequent evolution into a bound quarkonium. [59]

resonant states, but velocity scaling leaves only a few non-negligible terms through which a quarkonium could be produced: either the color-singlet ${}^3S_1^{[1]}$, or from one of three color-octet states ${}^3S_1^{[8]}$, ${}^1S_0^{[8]}$, or ${}^3P_J^{[8]}$. Because the evolution from the color-singlet is straight-forward, with no change in S or L, the LDME for the color-singlet state is calculable through potential models. In fact, this special case of quarkonium production is called the "Color-Singlet Model," and was the leading production theory until the CDF collaboration at Fermilab showed $\psi(nS)$ cross section measurements to be 50 times lower than predicted [60]. The color-octet LDMEs are non-calculable owing to the complexities arising from a colored system, and must be determined by fits to quarkonia production data, such as cross sections and polarizations.

An NRQCD calculation at next-to-leading order of p_{T}-differential $Q\overline{Q}$ SDC cross sections for the J/ψ is shown in Fig. 3.11. Scaling the SDC cross sections by their respective LDME will produce the total J/ψ cross section. The inverse of

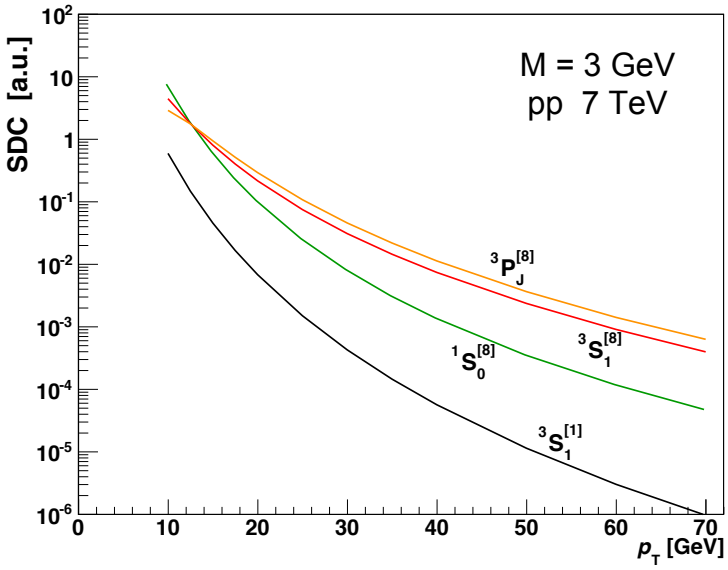

Figure 3.11: NRQCD calculations from [61] of the J/ψ SDCs, as presented in as a function of p_{T} [62].

this process is to determine the LDMEs through fits to the cross section data, as was commonly done prior to the LHC era, when polarization measurements were unreliable. The problem with this approach is that the SDCs all have a very similar shape, making it difficult to truly discern the LDMEs strictly from cross sections.

Polarization measurements, on the other hand, give a direct observation of the quantum state of the pre-resonant $Q\overline{Q}$, and the NRQCD predictions are much more distinct. For example, a $^3S_1$ meson (i.e. a ψ or Υ) that evolves predominantly from a $^1S_0^{[8]}$ $Q\overline{Q}$ pair is expected to be completely unpolarized, whereas a transverse polarization would be expected if production occurred through the $^3S_1^{[8]}$ state. The predictions for the other two terms are considered to be not fully converged and would greatly benefit from next-to-next leading order calculations, but their predictions are also distinct: the $^3S_1^{[1]}$ term should produce longitudinal polarization and the $^3P_J^{[8]}$ produces a "hyper-transverse" measurement that changes rapidly with p_{T}.

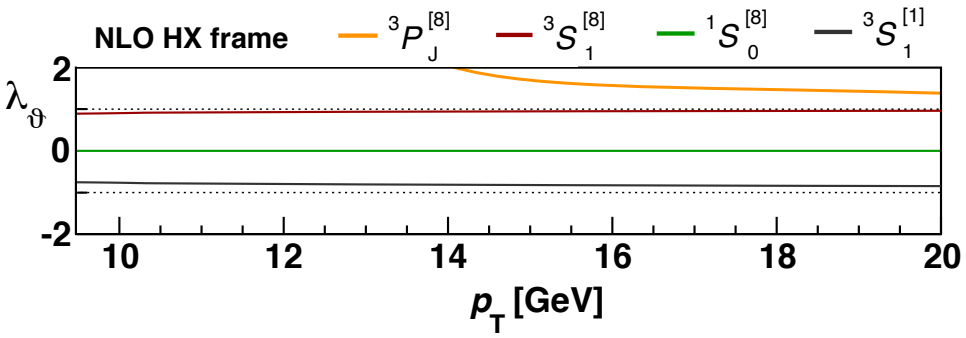

Figure 3.12: NRQCD calculations from [61] of the polarization parameters of each $Q\overline{Q}$ term, as presented in [62].

These predictions are shown in Fig. 3.12, where $\lambda_\vartheta = +1$ is transverse polarization, $\lambda_\vartheta = -1$ is longitudinal, and $\lambda_\vartheta = 0$ is unpolarized. The meaning of these terms and the method for measuring quarkonia polarization is discussed in Sec. 3.2.

Recently, conclusive polarization measurements have been published, with CMS showing p_{T} and $|y|$ differentiated polarization results of the J/ψ, $\psi(2S)$, $\Upsilon(1S)$, $\Upsilon(2S)$, and $\Upsilon(3S)$ [63,64]. Surprisingly, the results, which have proven to be consistent with other recent measurements out of CDF [65], LHCb [66], and ALICE [67], showed very small polarizations for the measured quarkonia. Cross section fits had led to the belief that the $^3S_1^{[8]}$ state was the dominant production color channel, which was first proposed by Braaten and Fleming in [68]. Consequently, this implies a strongly *transverse* polarization. At the momentum scales achieved at the Tevatron and the LHC, where $p_{\mathrm{T}} >> m_{\mathcal{Q}}$, quarkonium should be produced via gluon fragmentation [69], and, as proposed by Wise and Cho, the transversely polarized on-shell gluon should transfer its angular momentum to the $Q\overline{Q}$ pair, resulting in a similarly polarized quarkonium [70]. Thus, these new, unexpected polarization results where quite confounding.

Yet, the recent measurements are not a refutation of NRQCD, and instead show the importance of polarization input into LDME calculations. In fact, upon reevaluation of available high-p_{T} cross section data and inclusion of the polarization results, these polarization measurements, though originally unexpected, are acceptable within NRQCD by a dominance of quarkonia production through the ${}^1S_0^{[8]}$ term [62]. The new fits benefited not only from polarization data, but also from high-p_{T} cross section data, whereas previous analyses have had only low-p_{T} data available, where NRQCD approximations begin to lose validity.

The confirmation that quarkonia are produced through a color-octet channel, even if not the originally expected channel, leads to more questions. If, indeed, the majority of quarkonia are produced through the ${}^1S_0^{[8]}$ channel, that means that the dominant pre-resonant $Q\overline{Q}$ pair would have to radiate or absorb soft gluons in order to form the observed color-neutral quarkonium. That is, the $Q\overline{Q}$ pair must neutralize its color by *interacting with its surroundings*. This statement is significant, because implicit in the NRQCD factorization hypothesis is the assumption that the LDMEs are both constant and universal - that is, they are not dependent on production kinematics, and the same values should be extracted from production in, e.g., e^+e^-, *pp*, and PbPb collisions. On the other hand, one may question whether interaction of the $Q\overline{Q}$ pair with its surroundings could affect the LDMEs, and that question leads to several more: What if the production is different between a *pp* and a PbPb collision? Does the environment surrounding the quarkonium influence its production? Does the presence of a QGP effect the basic mechanism?

Finally, this leads to a question of interest to the nuclear physicist - Does this

influence the interpretation of quarkonia suppression results? Recall that yields can be modified by phenomena *other* than the QGP, and these cold nuclear matter effects are studied using pPb collisions. Generally, the effects are attributed to known phenomena like parton energy loss, modification of parton distribution functions, and a shift of the hadron momentum distribution, called the Cronin effect [71, 72]. In NRQCD terms, these effects all modify the short-distance SDCs. As we have seen, the $Q\overline{Q}$ pair must interact with its surroundings as it evolves into a bound state quarkonium. Now, based on LDME universality, we can assume that the second step of quarkonium production will not change, but at the moment, LDME universality remains a conjecture. Experimental verification would not only be of significant importance to the NRQCD factorization approach, it would also rule out a possible change in the basic production mechanism between *pp* and AA collisions, eliminating an as-of-yet unaccounted for modification of quarkonia suppression in nuclear collisions.

With quarkonia cross sections significantly modified in nuclear collisions, polarization measurements, unambiguously sensitive to the $Q\overline{Q}$ bound-state formation process, are of unparalleled importance in ensuring the production mechanism does not change between systems. Indeed, a change in polarization only has two possible explanations: First, this could be caused by a reordering of the dominant color channel, i.e. a change in the basic production mechanism. Second, assuming the polarization of the P-wave states are different from that of the S-wave, a polarization change could give insight into feed-down effects in quarkonium suppression measurements. Distinguishing between these two possibilities requires a broad investigation

in QCD medium effects, requiring polarization measurements in pp, pA, and AA systems.

This thesis seeks to answer the above questions, to attempt to either experimentally confirm, or present evidence of a violation of the LDME universality conjecture, and to begin the investigation of QCD medium effects through measurements of the $\Upsilon(nS)$ and prompt-$\psi(nS)$ polarizations as functions of charged-particle multiplicity.

3.2 Quarkonium Polarization

S-wave quarkonia are produced in a superposition of angular momentum states $J_z = +1, -1, 0$ with respect to the polarization axis z:

$$|J, M\rangle = |1, +1\rangle\,, |1, 0\rangle\,, |1, -1\rangle\,. \tag{3.6}$$

When a particle is produced preferentially in a subset of the possible eigenstates, the particle is said to be polarized. Due to the basic conservation principles of the electromagnetic and strong interactions, this polarization is passed from parent particle to decay products, and so the polarization may be inferred through the distribution of a particle's decay. To explain this process in more detail, consider the case of a J/ψ decaying into a dilepton pair, from the perspective of the J/ψ rest frame, as seen in Fig. 3.13, which defines the polar and azimuthal angles, ϑ and φ, of the positive lepton. The quarkonium production plane itself is defined as shown in Fig. 3.14a, where b_1 and b_2 represent the two colliding beams. There

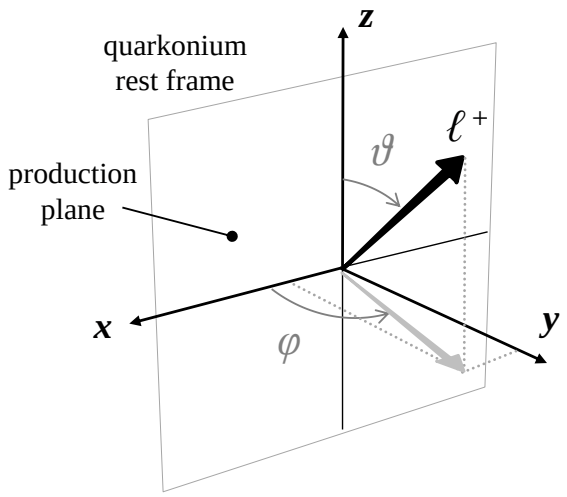

Figure 3.13: The polar and azimuthal angles of a quarkonium decay are defined with respect to the quantization axis z [73].

are then many potential choices for the quantization axis within the production plane, but for the the purposes of this thesis, the chosen reference frames are the Helicity (HX) frame, where the quantization axis coincides with the direction of the quarkonium, the Collins-Soper (CS) frame, which bisects the angle of the beams, and the Perpendicular Helicity (PX) frame, which is orthogonal to the CS frame. These reference frames are all shown in Fig. 3.14b.

The overall decay is intrinsically tied to the initial quantum state of the J/ψ, and so the basic rules of rotational invariance and conservation of parity and helicity are applicable. As the J/ψ decays into a dilepton pair, helicity conservation demands that the leptons retain the spin alignment of the J/ψ, requiring that the meson decay to two leptons with spins aligned along a new quantization axis z', leaving spin projection $M_{l^+l^-} = \pm 1$, and with $M_{l^+l^-} = 0$ forbidden. This implies that a rotation is necessary to align to z' of the dilepton pair, and that it must be a superposition of the original three eigenstates. This can be done using Wigner D-matrices ($D^J_{MM'}$)

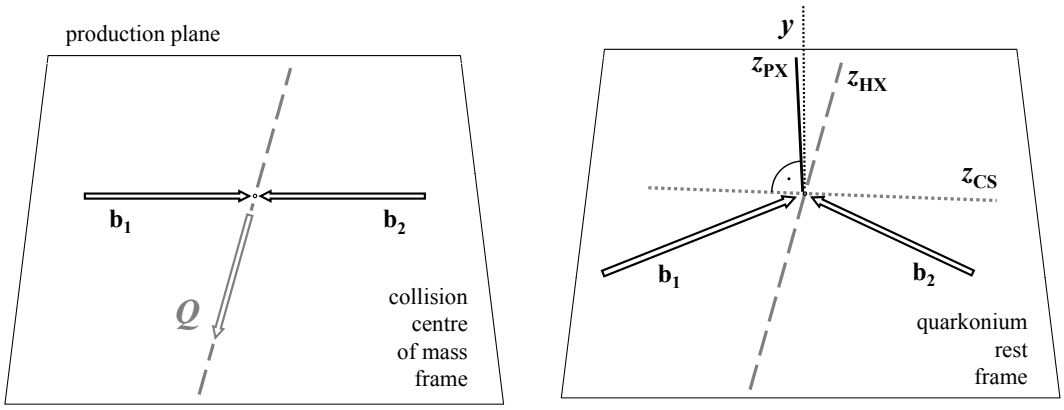

(a) (b)

Figure 3.14: A plane that holds the two beams (b_1 and b_2) and the quarkonium ($\mathcal{Q}$) is defined as the production plane is shown in (a). Three common quantization axes are shown in (b). The PX quantization axis is set as orthogonal to that in CS frame, which sets the z-axis as the bisect of the beam angles. The HX axes coincides with the direction of the quarkonium. Figures from [73].

as follows:

$$|J, M'\rangle = \sum_{M=-J}^{+J} D^J_{MM'}(\vartheta, \varphi)\,|J, M\rangle\,. \tag{3.7}$$

For a J/ψ decay to a $M = +1$ dilepton pair this becomes

$$|1, +1\rangle = D^1_{-1,+1}(\vartheta, \varphi)\,|1, -1\rangle + D^1_{0,+1}(\vartheta, \varphi)\,|1, 0\rangle + D^1_{+1,+1}(\vartheta, \varphi)\,|1, +1\rangle\,. \tag{3.8}$$

This shows that within the dilepton $|1, +1\rangle$ state there is information about the initial quantum state of the J/ψ, with the Wigner D-matrices giving the amplitude of each component. By squaring the Wigner operations, decay distributions are obtained:

$$\frac{dN}{d\Omega} \propto |\,\langle 1, +1|\,\mathcal{O}\,|1, 0\rangle\,|^2 \propto 1 - cos^2\vartheta, \tag{3.9}$$

$$\frac{dN}{d\Omega} \propto |\,\langle 1, +1|\,\mathcal{O}\,|1, +1\rangle\,|^2 \propto 1 + cos^2\vartheta + 2cos\vartheta, \tag{3.10}$$

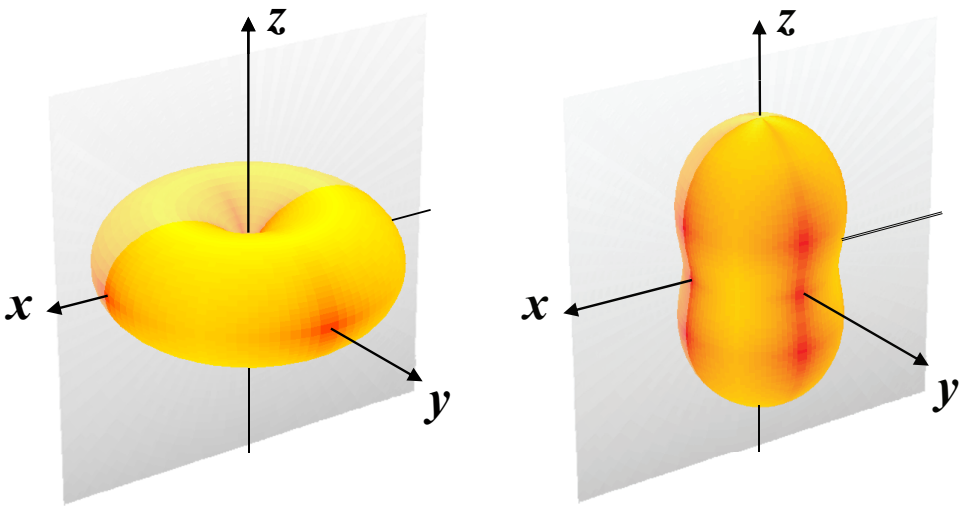

(a) (b)

Figure 3.15: The decay distributions of two extreme polarization scenarios, purely longitudinal (a) and purely transverse (b). [73]

$$\frac{dN}{d\Omega} \propto |\langle 1,+1|\,\mathcal{O}\,|1,-1\rangle|^2 \propto 1 + cos^2\vartheta - 2cos\vartheta. \tag{3.11}$$

An alignment along $M = 0$, referred to as "longitudinal" polarization, produces a decay modeled by Eq. 3.9, the shape of which is shown in Fig. 3.15a. The $M = \pm 1$ alignments are called "transverse" polarization, and the decay distribution, due to parity conservation, is an equal sum of Eq. 3.10 and 3.11, producing the shape shown in Fig. 3.15b.

The most general description of the angular decay distribution is written as

$$\frac{dN}{d\Omega} \propto \frac{1}{3+\lambda_\vartheta}(1 + \lambda_\vartheta cos^2\vartheta + \lambda_\varphi sin^2\vartheta cos2\varphi + \lambda_{\vartheta\varphi} sin2\vartheta cos\phi), \tag{3.12}$$

where $\vec{\lambda} = (\lambda_\vartheta, \lambda_\varphi, \lambda_{\vartheta\varphi})$ are frame-dependent polarization parameters; λ_ϑ measures the polar anisotropy, λ_φ the azimuthal anisotropy, and $\lambda_{\vartheta\varphi}$ the correlation between the two. Though the ideal quantization axis is *a priori* unknown, the natural refer-

ence frame is obtained if the chosen quantization axis were to be aligned as shown in Fig. 3.15, which gives λ_ϑ at its maximum value, while λ_φ and $\lambda_{\vartheta\varphi}$ are zero. In this frame, a transverse polarization measures polarization parameters $\lambda_\vartheta = +1$ and, longitudinal measures $\lambda_\vartheta = -1$, both with $\lambda_\varphi = \lambda_{\vartheta\varphi} = 0$. In other frames, a measured $\lambda_\vartheta = 1$ value may not necessarily imply transverse polarization. Furthermore, in a less ideal frame, the observed polarization parameters become dependent on kinematics. Therefore, it is beneficial to define a frame-invariant polarization parameter, $\tilde{\lambda}$:

$$\tilde{\lambda} = \frac{\lambda_\vartheta + 3\lambda_\varphi}{1 - \lambda_\varphi}. \tag{3.13}$$

This parameter is dependent only on the actual shape of the distribution, and is independent of both kinetics and reference frame choice. In the case of no polarization, the distribution would be completely isotropic, and all polarization parameters would be calculated as zero.

Until recently, polarization measurements were quite puzzling. Results out of CDF Run 1, with a measurement of slightly longitudinal J/ψ polarization were in conflict with expectations from theory [74]. More so, inconsistencies between, and even within, experiments complicated matters. Measurements from CDF showed the $\Upsilon(1S)$ is produced unpolarized, yet D0 showed longitudinal polarization [75, 76]. A second measurement of J/ψ polarization from CDF Run II contradicted the results from Run I, showing no significant polarization. These mutually exclusive experimental results likely were the result of ambiguous methodologies that failed to account for the frame dependence of polarization observables [73].

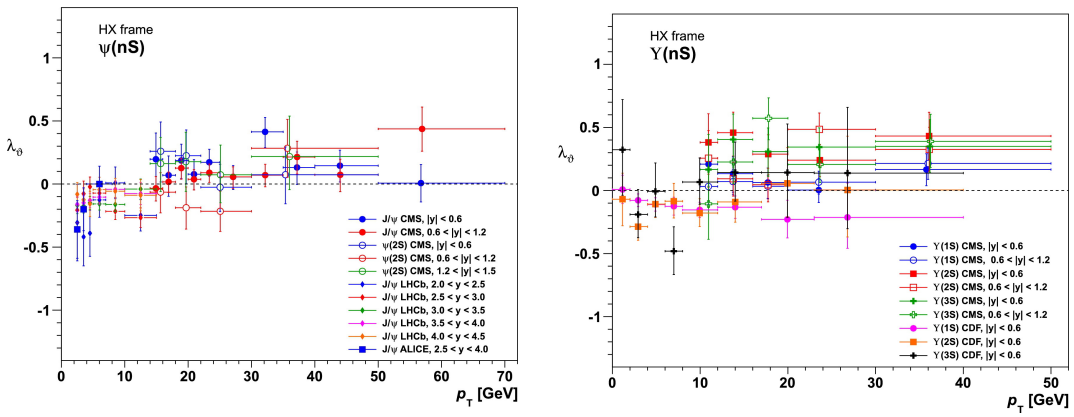

(a) (b)

Figure 3.16: Recent λ_ϑ measurements from several different experiments, for the ψ (a) and Υ (b) mesons [62]. The CMS, ALICE, and LHCb data was measured in $\sqrt{s} = 7$ TeV pp collisions and the CDF data in $\sqrt{s} = 1.96$ TeV $p\overline{p}$ collisions.

More recently, CMS has emerged as a leader in quarkonia polarization measurements, publishing unambiguous p_{T} and $|y|$ differentiated polarization results of the J/ψ, $\psi(2S)$, $\Upsilon(1S)$, $\Upsilon(2S)$, and $\Upsilon(3S)$ in three different reference frames for the three frame dependent (λ_ϑ, λ_φ, and $\lambda_{\vartheta\varphi}$) and the frame independent ($\tilde{\lambda}$) polarization parameters [63,64]. These results, along with additional measurements from ALICE [67], CDF [65], and LHCb [66], are shown in Fig. 3.16.

This thesis represents an extension of the CMS results, integrating the results in rapidity and partially integrating in p_{T} and measuring polarization against charged particle multiplicity in pp collisions. The aim of this thesis is different than the previously published results, where the authors strove to probe QCD to further understand hadron production. The present work concentrates more on the implications of quarkonium production within a QGP, and serves as the first step of a broad study of QCD medium effects on the production of quarkonia.

Chapter 4: The LHC and CMS

"We know it will discover exciting things. We just don't know what they are yet."

~Dr. Brian Cox, on the LHC

The study of the infinitesimal systems described so far in this thesis requires tools worthy of superlatives. The Large Hadron Collider (LHC) is a 27 km circumference dual-ring accelerator, the last and largest part of an intricate series of accelerators at CERN. Used to produce collisions that create the QGP, quarkonia, and other rare particles, the LHC accelerator complex is recognized as the world's largest experimental apparatus. Capable of reaching center-of-mass collision energies of up to 14 TeV per nucleon, a second accurate descriptor is that of the world's highest energy particle collider. The accolades bestowed upon the detector system, the Compact Muon Solenoid (CMS), are that it contains the world's most powerful superconducting magnet, designed to produce a 4 Tesla magnetic field, as well as the world's largest silicon detector system. The series of accelerators that culminates with the LHC acts as the heart of the high-energy physics program at CERN, circulating protons and/or lead nuclei in opposing beam pipes at nearly the speed of light. At four points along the LHC, where the beam pipes intersect and particles collide, sit giant detectors that act as the eyes of the experiments. CMS, along with

LHCb, ATLAS, and ALICE, readout electronic traces of particles, which are then processed by the brains[1] of the experiments, the massive, worldwide computing network that turn the electrical signals into physical descriptions of an event. These three components, the collider, the detector, and the computing grid that must be finely tuned to work in conjunction with one other, will be described in this chapter. For a full description of the LHC, see Ref. [77], and for the design and physics performance of CMS, see Refs. [78–80].

4.1 The Large Hadron Collider (LHC)

The LHC, located outside of Geneva across the Franco-Swiss border at the European Organization for Nuclear Research (CERN), is a synchrotron particle collider. The main tunnel, 27 km in circumference and more than 100 m underground, houses two opposing particle beams that cross at four points, where the beams collide and the emergent particles are measured. The LHC is capable of accelerating protons and/or lead nuclei, which are accelerated in bunches to ensure collisions at regular intervals. This can lead to multiple collisions per punch crossing, which is referred to a "pile-up." The point of each collision is called the event's "vertex." High beam luminosities are required to produce enough of the exceedingly rare events that the experiments at the LHC seek. The amount of events produced per second is given by

$$N_{\text{event}} = L\sigma_{\text{event}}, \tag{4.1}$$

[1] Of course, there are thousands of biological brains involved in each of the experiments as well.

where σ is the cross section of a particular process and L is the luminosity of the beam, which quantifies the number of collisions per $cm^2 \cdot s$ is given by

$$L = \frac{N_b^2 n_b f_{\text{rev}} \gamma_r}{4\pi \epsilon_n \beta *} F, \tag{4.2}$$

where the number of of particles per bunch is given as N_b, the number of bunches per beam as n_b, the revolution frequency as f_{rev}, γ_r is the relativistic gamma factor, ϵ_n is the normalized transverse beam emittance, $\beta *$ is the beta function, and F is a factor that corrects the luminosity due to the crossing angle at the point of the collision. The LHC is designed to deliver peak luminosities of $L = 10^{34}\,\text{cm}^{-2}\text{s}^{-1}$ for pp collisions and $L = 10^{27}\,\text{cm}^{-2}\text{s}^{-1}$ during PbPb operation.

Before being injected into the LHC, protons are boosted through a series of smaller accelerators, as depicted in Fig. 4.1. The original proton source is a tank of hydrogen gas. The first step in the chain of events leading to a proton collision is to break apart hydrogen gas and strip the protons of their electrons by applying an electric field, which occurs on one end of the linear accelerator Linac 2. Once the protons reach the other end of Linac 2, they have an energy of 50 MeV and enter the Proton Synchrotron Booster (PSB). In the PSB, they are boosted to 1.4 GeV and injected into the Proton Synchrotron (PS), where they are boosted to 25 GeV. The final step before injection into the LHC is the Super Proton Synchrotron (SPS), which accelerates the protons to 450 GeV. This process is repeated until each LHC ring is full, which takes 4 minutes and 20 seconds for each beam. Once in the LHC it takes 20 minutes for the protons to reach their specified energy.

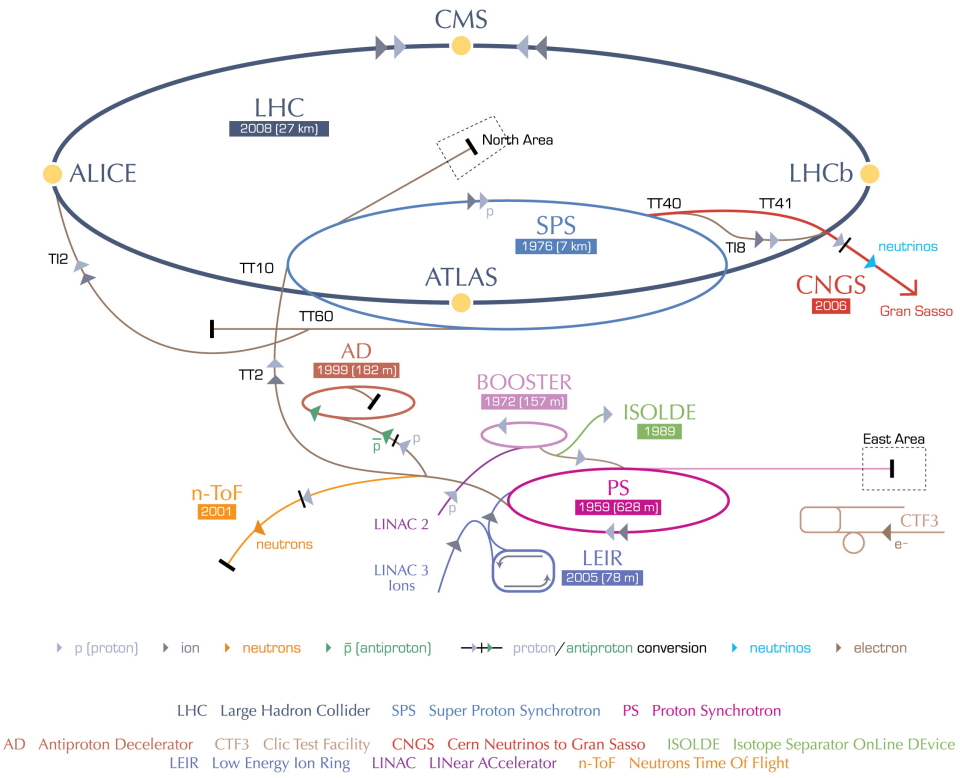

Figure 4.1: The elements of the CERN accelerator complex [81].

Lead nuclei take a slightly different route to the LHC [82]. The initial lead source is a solid block of isotopically pure lead-208, which is heated to vaporization and ionized using Electron-Cyclotron Resonance to create Pb^{29+}. The lead ions are then accelerated up to 4.2 MeV and pass through a sheet of carbon foil, which strips more electrons to produce Pb^{54+}. The ions are then collected as bunches in the Low Energy Ion Ring (LEIR) and injected into the PS, where the acceleration proceeds as it does for protons. Between the PS and the SPS there is another carbon sheet that strips the remaining electrons, giving Pb^{82+}.

Once the beams are filled and at their maximum energy, they are directed to the collision point and data collection begins. The beams remain in this state for

several hours, until the beam has too few particles or loses focus, ending a particular "fill." The remainder of the beam is then "dumped" by guiding it into large graphite absorbers and the entire process restarts.

4.2 The Compact Muon Solenoid (CMS)

CMS is located at CERN's Point 5 in an underground cavern near Cessy, France. True to its name, CMS is a compact[2] detector that excels in the measurement of muons using a 3.8 T solenoidal magnet. There are many components of the detector that cover a large pseudorapidity (η, the experimentalist's approximation of rapidity, where $\eta = -ln[tan(\frac{\theta}{2})]$, shown in Fig. 4.2) range that, in addition to muons, detect different types of particles necessary to reconstruct a particle collision (an event). Some events are more interesting to observe than others, and because of the immense amount of data being generated, a series of triggers have been defined in order to determine which events are worth saving. Reconstruction of events is a computer driven process that traces the number and energy of detected particles back to the original event vertex.

An overview of the CMS detector is shown in Fig. 4.3. The coordinate system of the detector is centered at the nominal "Interaction Point" (IP) of the collisions, which is ideally in the exact center of the detector, and then follows the commonly used "right-hand rule," with the z-axis defined along the beam, the x-axis directed towards the center of the LHC ring, and the y-axis pointed upwards. The azimuthal angle ϕ is measured relative to the $x-y$ plane, and the polar angle θ is measured

[2]This term is relative, as it is "only" a 12,500 metric ton, 21 m long, 15 m diameter cylinder.

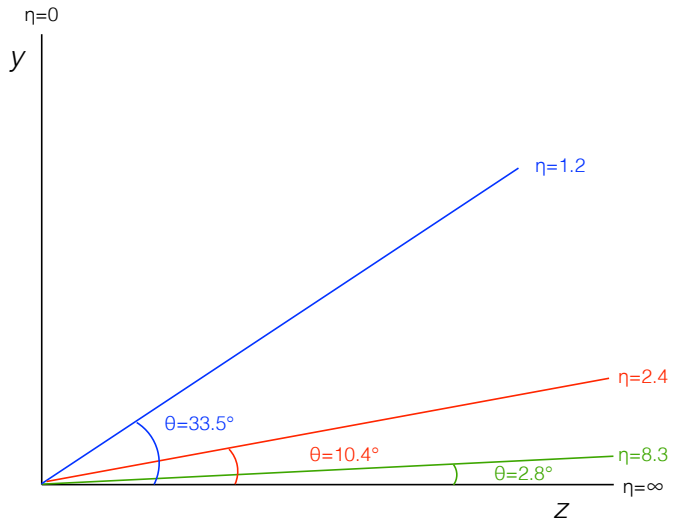

Figure 4.2: The relationship between the polar angle θ and pseudorapidity, η. The lines indicate major points in the detector. At $\eta = 1.2$ the barrel section ends and the end caps begin, extending to $\eta = 2.4$. The Zero Degree Calorimeter begins at $\eta = 8.3$ and extends through infinity. The Forward Hadron (not depicted) is located at $2.9 < |\eta| < 5.2$.

relative to the z-axis.

The main feature of CMS is the 3.8 T superconducting solenoidal magnet. Immediately inside the magnet is the Hadronic Calorimeter (HCAL), then the Electromagnetic Calorimeter (ECAL), and finally the Silicon Tracker. Outside the magnet lie alternating layers of the muon tracking system and the magnetic return yoke. Each system has a cylindrical "barrel" section with disk-shaped "end caps" on each side, providing full azimuthal coverage out to $\eta < 2.4$. CMS also has calorimeters at higher pseudorapidities, including a Forward Hadron Calorimeter ($2.9 < |\eta| < 5.2$) and a Zero Degree Calorimeter ($|\eta| > 8.3$) on each side of the detector. Transverse momentum, p_{T}, is measured with respect to the beam, and thus calculated from the x- and y- components a particle's four-momentum vector.

Many of the particles of interest produced in LHC collisions, like quarkonia, are

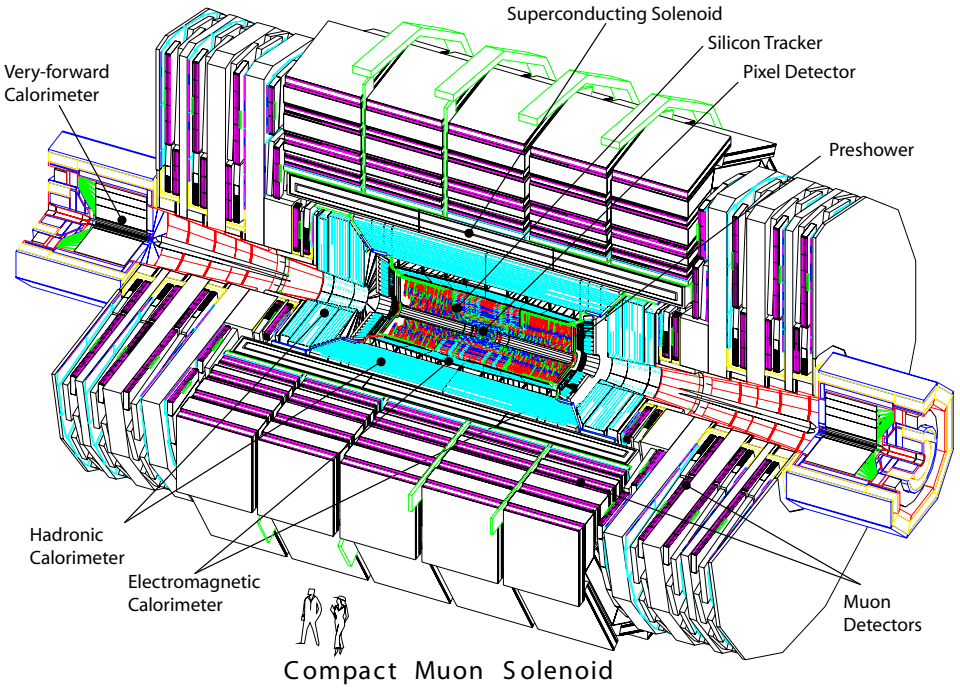

Figure 4.3: A layout of the main CMS detector system, showing the majority of the subsystem detectors. Not pictured are the Zero Degree Calorimeters, located at ±140 m down the beam pipe, which measure neutrals [78].

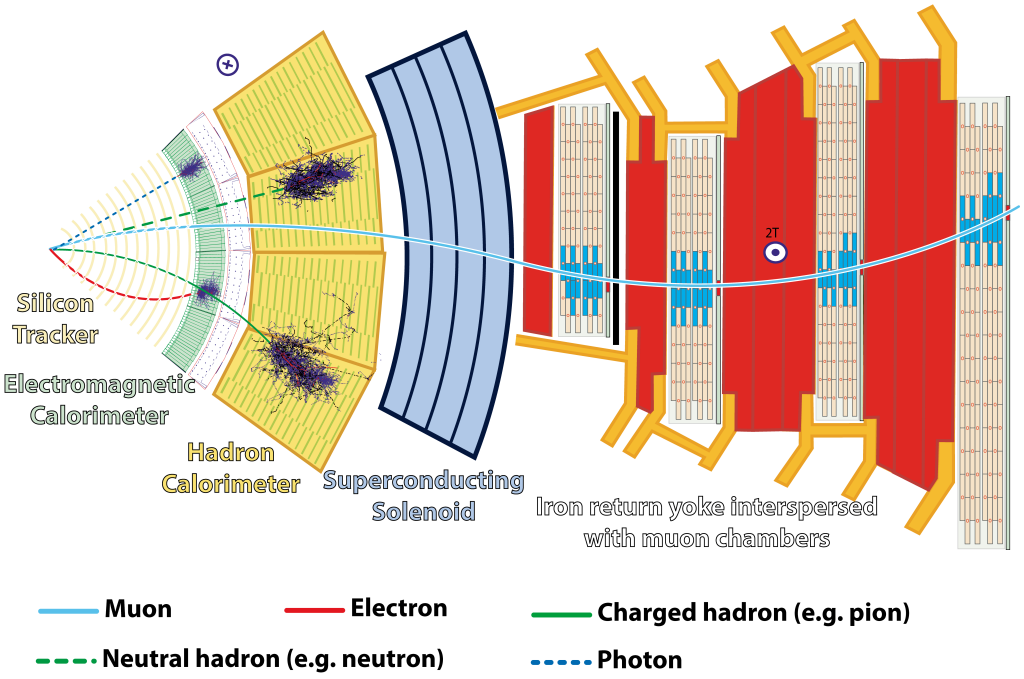

Figure 4.4: A transverse slice of the CMS detector illustrating its main components and the tracks of particles passing through [83].

highly unstable, and very quickly decay into lighter, more stable particles, which are what CMS actually detects. Figure 4.4 shows a transverse slice of the CMS detector, and illustrates how it detects these stable particles. The solenoidal magnet is integral to the detector's performance because it bends charged particles, enabling the calculation of the particle's transverse momentum (p_{T}) based of the radius (r) of the curvature and strength of the magnetic field (B):

$$p_{\mathrm{T}} = 0.3Br. \tag{4.3}$$

The various subsystems of CMS are all designed to detect a particular type of particle, and a specific particle is identified based on how it interacts with the detector. The first component, starting from the IP (the left most point of Fig. 4.4), is the Silicon Tracker. The purpose of the tracker is not to stop and identify particles, but to track charged particle movement through the detector. Surrounding the tracker is the ECAL, which detects photons and electrons as they interact with lead tungstate crystals and produce particle showers that eventually are picked up by avalanche photodiodes. The charged electron is differentiated from a photon because it will have left a curved path in the silicon tracker, while uncharged photons pass straight through, undetected until registering a signal in the ECAL. Hadrons pass through the tracker and begin to shower in the ECAL, then deposit most of their energy in the HCAL, which is made of alternating brass and plastic scintillator layers. Neutral and charged hadrons, analogous to photons and electrons, are differentiated by matching tracks in the Silicon Tracker to energy deposits in the HCAL. The

only detectable particles that pass through the magnet are muons, and thus they are fairly easy to identify, as any track in the muon system can be identified as a muon, and then matched to a track in the Silicon Tracker. Neutrinos do not interact with the detector, but their presence can be inferred by measurements of missing transverse momentum. The two systems most pertinent to this analysis are the Silicon Tracker and the Muon System, which will be discussed in more detail in the following section.

4.2.1 Muon Detection at CMS

The detection of muons at CMS is quite important, with the presence of a muon generally indicating an interesting physics process has occurred, such as the production of a quarkonium. For a high quality measurement of muons, CMS employs both the Silicon Tracker and the Muon System. The Muon System consists of three types of gaseous detectors, Drift Tubes, Resistive Plate Chambers, and Cathode Strip Chambers, and increases the resolution of the momentum measurement of of high-momentum muons ($p > 200$ GeV/c) and are an integral part of the detector triggering system. Two systems comprise the Silicon Tracker, the Silicon Strip and Silicon Pixel detectors, which together are able to quickly and efficiently track the trajectories of charged particles emanating from the collision vertex and identify secondary vertices. The performance of the two systems is shown in Fig. 4.5, where it is clear that for $p > 200$ GeV/c the Muon System improves the muon momentum resolution.

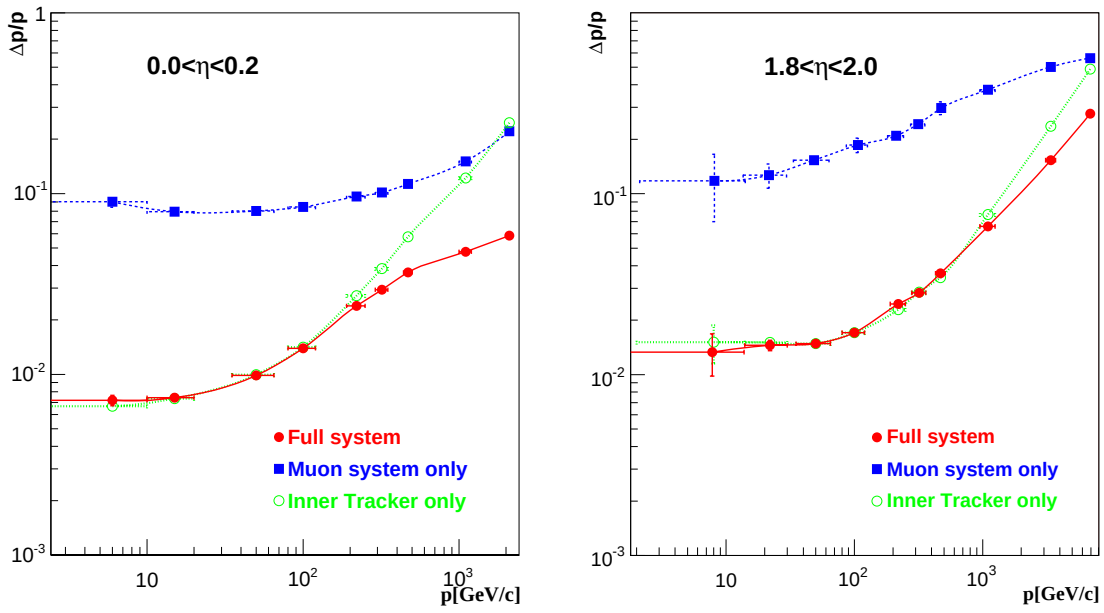

(a) (b)

Figure 4.5: Momentum resolution $\Delta p/p$ for muons in CMS in two pseudorapidity ranges. The inner tracker system (green) has very good resolution at lower p_{T}. Above a certain point, using the full system (red) provides improved momentum resolution. Resolution is better at lower pseudorapidities [78].

4.2.1.1 The CMS Tracking System

At the LHC design luminosity, an average of 20 pp collisions will occur every 25 ns, producing an average of approximately 1000 charged particles per bunch crossing [80], requiring an exceptionally fast and granulated detector. Considering the intense particle flux the tracker must withstand, radiation hardness is also a must. These requirements led to the design of a fully silicon based detector. Overall, the tracker has 1440 pixel and 15,148 silicon strip detector modules, totaling approximately 200 m^2 of active silicon, extending out to $|\eta| < 2.5$.

The design of the tracker is shown in Fig. 4.6. Closest to the IP is the Pixel tracker, which consists of three barrel layers with $100 \times 150\ \mu\mathrm{m}^2$ pixels, at radii of

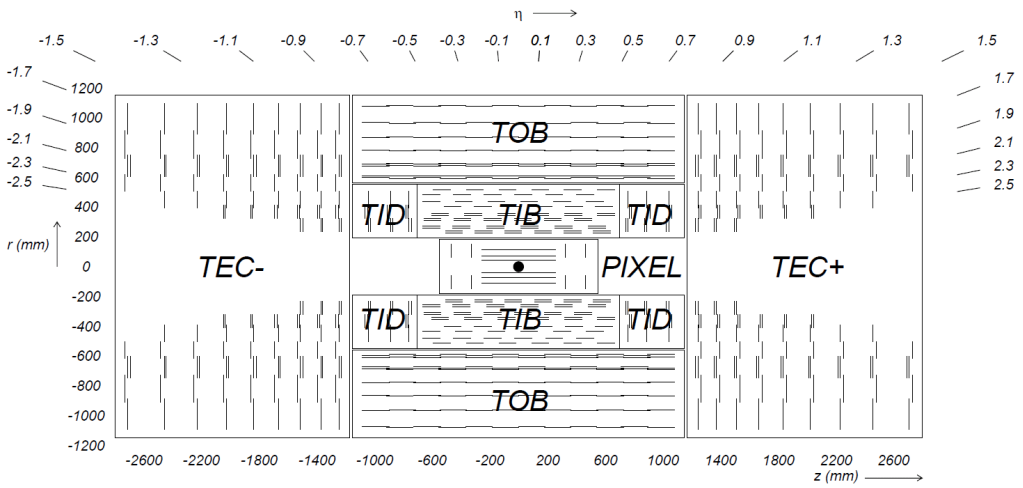

Figure 4.6: A schematic of the Silicon Tracker at CMS. The Silicon Tracker is made up of several systems: the innermost Pixel Detector, enveloped by the Tracker Inner Barrel (TIB), Tracker Outer Barrel (TOB), and Tracker Inner Disk (TID) systems, with the Tracker End Cap system on each end. Each line depicts an individual module [80].

4.4, 7.3, and 10.2 cm from the center, with two disk shaped end caps at $|z| = 34.5$ and 46.5 cm. The Silicon Strip Detector has ten layers split across two barrel parts, the Tracker Inner Barrel (TIB), set at $20 < r < 50$ cm, with silicon strip cells of size 10 cm $\times$ 80 µm, and the Tracker Outer Barrel (TOB), at $55 < r < 110$ cm, 25 cm $\times$ 180 µm silicon strips. Next to the TIB are the Tracker Inner Disks (TID), which add another three layers of silicon strips orthogonal to the TIB. The barrel section is capped by a Tracker End Cap (TEC) on each end, which adds another nine layers of silicon strips. Some layers of the Strip Detector have two back-to-back silicon strips, indicated in Fig. 4.6 by double lines, to produce "stereo" signals, which provides a measurement of z in the barrel regions and r in the disk regions. Even at the high particle densities in PbPb collisions, the occupancy of the Pixel Detector is expected to be $\sim 1\%$ and less than $\sim 20\%$ in the Silicon Strip Detectors, allowing for excellent particle track reconstruction.

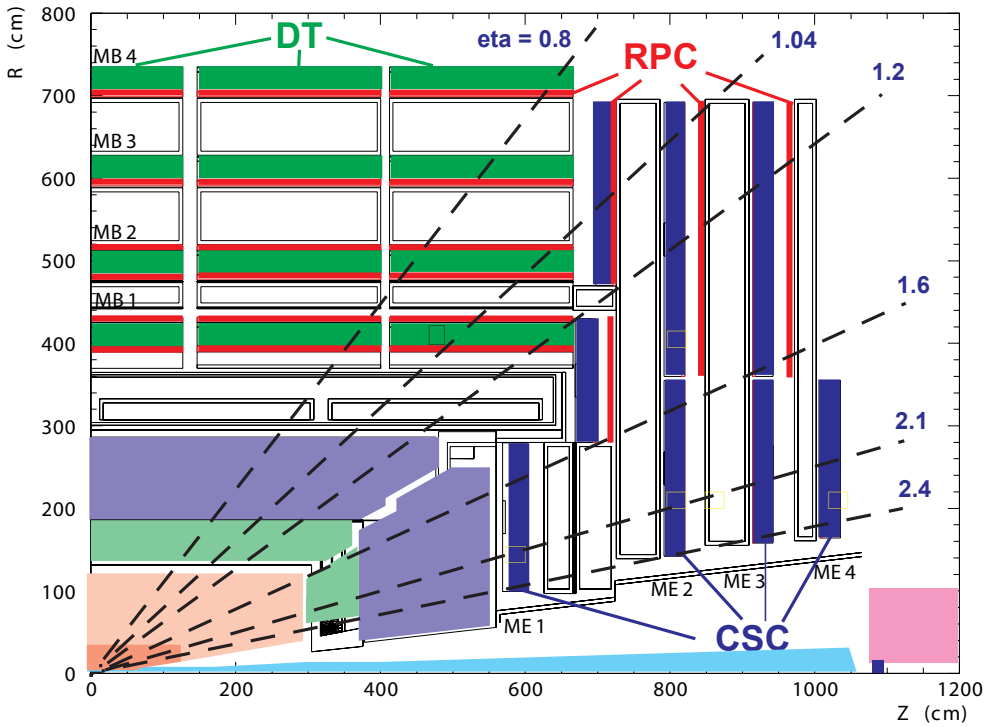

Figure 4.7: The Muon System at CMS. Drift tubes are shown in green, resistive plate champers in red, and cathode strip chambers in blue [78].

4.2.1.2 The CMS Muon System

The muon system is also designed with a barrel and two end cap sections, as seen in Figure 4.7, which shows one-quarter of the overall detector. The muon detectors are sandwiched between a steel return yoke, which confines the magnetic field and supports the weight of the detector. Three different technologies, drift tubes in the central barrel region, cathode strip chambers in the end cap regions, and resistive plate chambers for triggering in both regions, are used to detect muons. Between the central barrel and end cap detectors, the muon detection range extends to $|\eta| < 2.4$.

In the barrel region, the muon rate is fairly low and the magnetic field is

uniform. This allows for the use of Drift Tube (DT) chambers within $|\eta| < 1.2$. There are four layers of drift tubes, with each of the first three containing two groups of four DT plates, with one group measuring the r-ϕ bending plane and the other measuring z, and between each layer is the return yoke. The fourth layer has only one group of DT plates that measures r-ϕ. The DT chambers are a gaseous mixture of 85% argon and 15% carbon dioxide. When a muon enters a DT, the gas is ionized and ions drifts to the chambers' electrodes. The drift time is measured to calculate the coordinates of the muon as it entered the chamber.

In the end cap region, where the magnetic field is uneven and the particle rate high, Cathode Strip Chambers (CSC) detect muons between $0.9 < |\eta| < 2.4$. The CSCs are made of an arrays of negatively charged cathodes and positively charged anodes in a gaseous environment (40 % Ar, 50 % CO_2, 10 % CF_4) that register charges of ionized molecules caused by passing muons. Like the drift tubes, two coordinates of the passing particle are determined. The spatial resolution of both of these detectors is about 100 μm with a time resolution of 25 ns.

The DTs and CSCs are complemented by Resistive Plate Chambers (RPC) up to $|\eta| < 1.6$. The RPCs are made of parallel anode and cathode plates separated by a gaseous volume of 96.2 % $C_2H_2F_4$, 3.5 % C_4H_{10}, and 0.3 % SF_6. Because of their excellent time resolution ($\sim$ 1 ns), the resistive plate chambers are an integral part of the muon trigger system and are able to exactly identify with which bunch crossing a muon is associated.

4.2.2 CMS Triggering System

The most interesting processes at the LHC are exceedingly rare. In fact, for all the collisions that occur, only a select few are saved for processing and eventual data analysis. The LHC is designed to deliver collisions every 25 ns, with an average of at least 20 collisions per bunch crossing, corresponding to approximately 10^9 interactions per second, orders of magnitude higher than to 10^2 crossing per second that can actually be stored. Thus the development of an effective trigger system is mandatory, one capable of quickly rejecting information from up to 10^6 bunch crossings per second [78]. A tiered system was developed made up of a hardware-based "Level-1" (L1) trigger and a software-based "High-level" trigger (HLT), which is the combined Level-2 (L2) and Level-3 (L3) triggers. Both of these systems are constantly evolving as software and hardware is improved from year to year.

The amount of time elapsed between a bunch crossing and a preliminary L1 trigger decision is 3.2 μs, so to enable a fast trigger decision, trigger objects are formed from reduced granularity and resolution data while the high-resolution data is held in memory. The L1 Trigger keeps information from approximately 1 out of every 1000 bunch crossings. The L1 Trigger uses information from the calorimeters and the muon system based on the presence of certain photons, electrons, muons, and/or jets that hit specified E_{T} or p_{T} values. For more exotic processes, the triggers are also based off of global sums of E_{T} and missing E_{T}.

If a collision event passes L1, the buffered data is passed along to the HLT for further processing in a processor farm. The HLT is a software-based analysis

of full-resolution data that applies different filters and algorithms using information from all the sub-detector systems. Because full reconstruction takes time, each event is only reconstructed up to the maximal necessary level. For example, if a muon event passes the L1 trigger, but does not pass the stricter requirements once the muon system information has been reconstructed, the event is rejected outright, without wasting valuable computing time on the more intensive reconstruction of the tracking system. The HLT is designed to reduce the output rate from 100 kHz down to 100 Hz, which is then read out for full reconstruction and storage. For full details regarding the HLT, see [84].

4.2.2.1 Dimuon Triggering

This analysis was performed on 2011 pp collision datasets. The cleanest experimental signature of a quarkonium is a dimuon decay, so a dimuon trigger is used to collect potential quarkonia events. The basic trigger requirement was that there were two muon candidates detected in the same event. In 2011, the two muon candidates were required to be high-quality, which was accomplished by requiring that a muon candidate was confirmed in the Drift Tubes, Cathode Strip Chambers, and/or the Resistive Plate Chambers. This requirement was implemented using what is called the L1_DoubleMu0_HighQ trigger seed. The dimuon rate was high enough to require multiple triggers for different mass and kinematic regions, which were performed by the HLT. The HLT triggers relevant to this analysis required that both muons came from the same collision vertex, by requiring that the distance of

closest approach of the two muons was not more than 5 mm and that the vertex fit χ^2 probability was larger than 0.5 %. The dimuon pair was then restricted to mass regions around the J/ψ, $\psi(2S)$, and $\Upsilon(nS)$ mass peaks. The dimuon rapidity was restricted to the barrel region of the detector, $|y| < 1.25$, except the $\psi(2S)$, which had no such restriction. The p_{T} was variable throughout the run, depending on the instantaneous luminosity, and was lower for the Υs than for the J/ψ and $\psi(2S)$. Due to trigger bandwidth constraints, there was also a rejection of "cowboy" dimuons, which are those that bend towards each other in the magnetic field and therefore have lower detection efficiencies than "seagull" dimuons, which bend apart. The names of the HLT paths used to fulfill these requirements were:

- HLT_DimuonX_Jpsi_Barrel (X = 10, 13 GeV/c),
- HLT_DimuonX_PsiPrime (X = 7, 9, 11 GeV/c),
- HLT_DimuonX_Upsilon_Barrel (X = 5, 7, 9 GeV/c).

Figure 4.8 shows the invariant mass spectrum from the various dimuon triggers in 2011.

4.3 Computing Grid

The CMS computing grid employs computing clusters from around the world in a tiered system. All of the data that passes through the trigger system begins processing in Tier-0, which is the CERN central data processing center. The processed data is written out as RECO (reconstructed) data files, which are stored securely

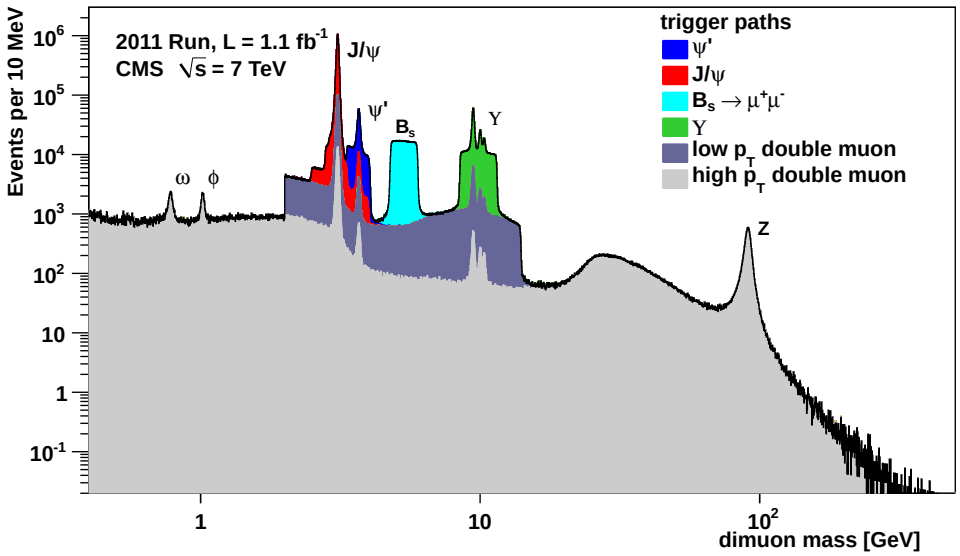

Figure 4.8: The invariant dimuon mass spectrum from data collected in 2011 with various dimuon triggers [85].

along with RAW data at Tier-0. User accessible RAW and RECO data files are copied to one of the Tier-1 centers, where they are processed further. Processing at the Tier-1 level is specific to the interested party, with different groups performing different types of event processing, producing smaller datasets that are more easily manageable for physics analyses. The output of the Tier-1 processing is generally transferred to Tier-2 sites, where physics analysis of the datasets is performed. Additionally, there are many local Tier-3 sites that are used as access points to the grid system. A full technical design report of the CMS computing system can be found in Ref. [86].

Chapter 5: Analysis

"If I have seen further it is by standing on the shoulders of giants."

~Sir Isaac Newton

The methods used in this analysis were developed and validated by the CMS Quarkonium team and have been previously been employed in the Ph.D. theses of Ilse Krätschmer [87] and Valentin Knünz [88], who measured the $\psi(nS)$ and $\Upsilon(nS)$ polarizations, differentiated in rapidity and p_{T}. The work culminated in the publication of two papers on quarkonia polarization measurements, [63] and [64]. Based on these efforts, this thesis extends the previous work to include a measurement of the event multiplicity dependence of the $\psi(nS)$ and $\Upsilon(nS)$ polarizations, the latter of which has been published [89]. As of writing, the $\psi(nS)$ has yet to be published.

As this thesis is a continuation of previous work, the structure of this section follows a similar outline to that of [87] and [88]. The polarization framework was developed and tested by Pietro Faccioli, João Seixas, and Valentin Knünz, and is summarized in [88]. All of the necessary inputs for the analysis was previously prepared, including the necessary datasets and various muon efficiency studies, thanks to Hermine Wöhri, Ilse Krätschmer, Linlin Zhang, and Valentin Knünz, as described in [87]. Ilse Krätschmer worked to develop the mass and pseudo-proper decay fits

necessary for the $\psi(nS)$ analysis, which was also presented in [87]. Carlos Lourenço was essential in preparation of internal CMS Analysis Notes[1] describing these analyses, and in pushing the results towards publication. My personal contributions to the project were to extend the polarization framework to include a measurement against event multiplicity, which required edits to the entire suite of code. I was then responsible for the entirety of the present analysis, the measurement of the $\Upsilon(nS)$ and $\psi(nS)$ polarization parameters versus the event charged particle multiplicity, N_{ch}, defined in Sec. 5.3. Compared to the previous analyses, the measurement is integrated in rapidity and partially integrated over p_{T} in order to ensure a sufficient number of events to accurately measure the $\vec{\lambda}$ parameters. Though these parameters can be kinematically dependent, the previous analyses showed no dependence on rapidity or p_{T}, and the integration over these variables is justified.

This chapter begins with a discussion of the muon efficiencies, essential for a proper implementation of the polarization framework, in Sec. 5.1. The common factors between the $\Upsilon(nS)$ and $\psi(nS)$ analyses are described in Sec. 5.2, and the definition of the event multiplicity is defined in Sec. 5.3. The specific details of the $\Upsilon(nS)$ and $\psi(nS)$ measurements are presented in Secs. 5.4 and 5.5, respectively. The two analyses are quite similar, differentiated only by the addition of a lifetime fit in the $\psi(nS)$ measurement, necessitated by a large feed-down fraction of events from B-hadrons. This requires the addition of an extra step in the $\psi(nS)$ data preparation, and must be accounted for in the background subtraction prior to

[1]For a member of CMS, in addition to the theses mentioned above, the Analysis Notes are valuable sources of information. For the development and validation of the framework, see [90]. The analysis of muon efficiencies is in [91] and [92]. The analyses themselves are detailed in [93], [94], [95], and [96].

extraction of the polarization parameters.

5.1 Muon Efficiencies

An accurate understanding of the single muon and dimuon efficiencies introduced by the detector and the trigger are of particular importance for unbiased polarization measurements. Single muon efficiencies (ϵ_μ) are determined using the data-driven tag-and-probe (T&P) method in different η and p_{T} ranges. Dimuon efficiencies ($\epsilon_{\mu\mu}$) are calculated partially from the single muon efficiencies, but also must take into account correlations between the two muons, which become increasingly important at high p_{T}. The total dimuon efficiency is given by

$$\epsilon_{\mu\mu} = \epsilon_{\mu,1} \cdot \epsilon_{\mu,2} \cdot \epsilon_{vtx} \cdot \rho, \tag{5.1}$$

where ϵ_{vtx} is the efficiency of the dimuon vertexing module used in the trigger, and ρ quantifies the dimuon correlations.

5.1.1 Single Muon Efficiencies

The single muon efficiencies are calculated as the product of several factors:

$$\epsilon_\mu = \epsilon_{track} \cdot \epsilon_{muonID} \cdot \epsilon_{muonQual} \cdot \epsilon_{L1 \cdot L2} \cdot \epsilon_{L3}, \tag{5.2}$$

where ϵ_{track} is the efficiency of the silicon tracker, ϵ_{muonID} is the muon identification and reconstruction efficiency with respect to a silicon track, $\epsilon_{muonQual}$ is the efficiency

of the muon quality cuts with respect to the previously reconstruced muon with no quality cuts, $\epsilon_{L1 \cdot L2}$ is the L1 $\cdot$ L2 trigger efficiency with respect to the reconstructed muon with muon quality cuts applied, and ϵ_{L3} is the generic efficiency of the L3 muon reconstruction.

The value of the tracking efficiency was calculated by the CMS Muon Physics Object group [97]. The remaining efficiencies are calculated using the T&P method described in [98]. Dedicated T&P efficiency triggers are needed to calculate the single muon efficiencies at low-p_{T} in an unbiased way, while keeping the trigger rate at a reasonable level. These triggers require that a single muon, combined with either a track or a L2 muon, lies within the J/ψ mass window (2.8–3.4 GeV). The latter combination is used to study efficiencies related to track requirements ($\epsilon_{muonQual}$, ϵ_{L3}), while the former is used to calculate the muon identification and the L1 $\cdot$ L2 efficiencies.

The triggered single muon is used as the "tag" muon while the track or L2 muon, required to be of opposite sign to the tag, is identified as the "probe." Probes are then subjected to the selection criteria under study (i.e. the muon selection requirements noted in Sec. 5.4.1) and grouped as either passing or failing probes, and used to build a "passing" or "failing" event mass spectrum. These two J/ψ invariant mass spectra are then fit simultaneously, and the efficiency is determined to be the number of passing probes over the number of total probes, which is left as a free parameter in the fit.

The four factors of the single muon efficiencies are calculated in narrow bins of single muon p_{T} and η, for data as well as Monte Carlo. Figure 5.1 depicts the data-

driven factorized single muon efficiencies for two different η regions. The efficiencies show a steep turn-on curve before they reach a plateau around an efficiency value of approximately 95% at a p_{T} of approximately 6 GeV/c. The efficiency values in the $0.2 < |\eta| < 0.3$ range are slightly lower due to a gap between the sections of the muon system.

The polarization studies are not dependent on the absolute value of the efficiencies, but are sensitive to the shape of the efficiency curves. Therefore, an exact mapping of the low-p_{T} turn-on curve is essential. Statistical fluctuations in the efficiencies are accounted for through parametrization, using the shapes of single muon efficiencies calculated directly (i.e. without using T&P) with a high statistics MC sample unbiased by dimuon correlations [87]. These "MC truth" efficiencies are shifted and scaled by three free parameters ($p^{\mu}_{\mathrm{T,scale}}$, $p^{\mu}_{\mathrm{T,shift}}$, and $\epsilon_{\mathrm{shift}}$) to match the data:

$$\epsilon_{\mu}^{\mathrm{DataT\&P}}(p_{\mathrm{T}}^{\mu}) = \epsilon_{\mu}^{\mathrm{MCTruth}}\left(\frac{p_{\mathrm{T}}^{\mu}}{p_{\mathrm{T,scale}}^{\mu}} - p_{\mathrm{T,shift}}^{\mu}\right) + \epsilon_{\mathrm{shift}}. \tag{5.3}$$

The scaled and shifted MC Truth efficiency curves are shown as the red lines in Fig. 5.1, and are seen to closely match the data. The dashed blue lines in this figure represents the error curves of the parametrization, which are determined by adding or subtracting a specific shift to each of the parameters, creating six error curves. The shifts are determined using information from the covariance matrix of the fit of MC Truth to the data, ensuring that correlations between that parameters are accounted for. These errors are used to establish a systematic uncertainty on the data, explained in Sec. 5.4.4.

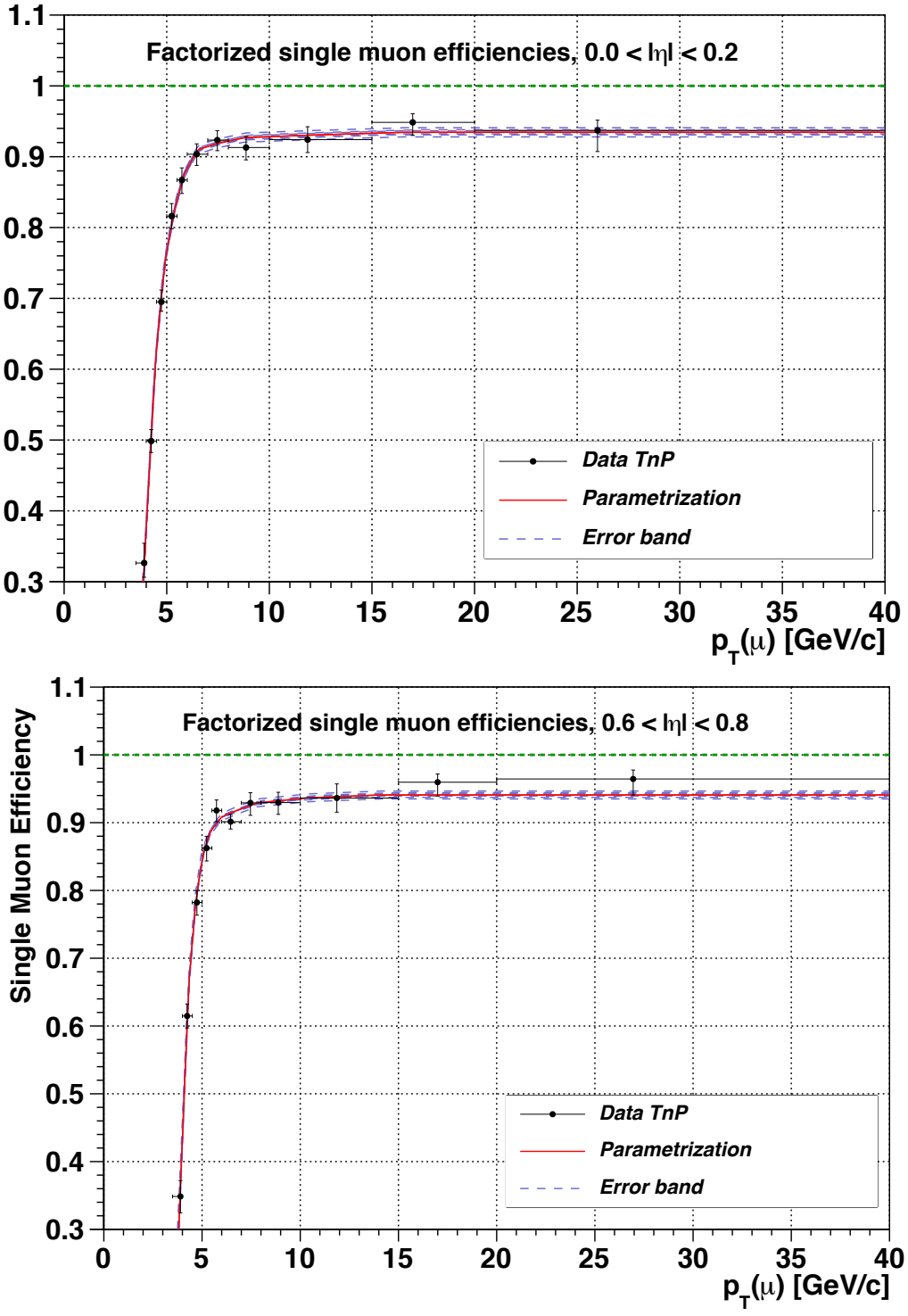

Figure 5.1: Single muon efficiencies as a function of p_{T}, the two η regions given in the figure, along with the corresponding parameterizations (red) and uncertainty bands (blue).

The MC truth efficiencies are compared to MC-based T&P efficiencies to evaluate the region where the efficiencies were valid. There were some slight deviations noted at low-p_{T} that led to the definition of a "safe" fiducial region that served as basic muon cuts for the polarization analysis:

$$\begin{aligned} |\eta^{\mu}| < 1.2: &\quad p_{\mathrm{T}}^{\mu,\mathrm{min}} > 4.5 \text{ GeV}/c, \\ 1.2 < |\eta^{\mu}| < 1.4: &\quad p_{\mathrm{T}}^{\mu,\mathrm{min}} > 3.5 \text{ GeV}/c, \\ 1.4 < |\eta^{\mu}| < 1.6: &\quad p_{\mathrm{T}}^{\mu,\mathrm{min}} > 3 \text{ GeV}/c. \end{aligned} \tag{5.4}$$

Any remaining differences between the MC T&P and MC Truth efficiencies are accounted for by establishing a T&P systematic uncertainty with ToyMC studies, as described in Sec. 5.4.4.

5.1.2 Dimuon Correlations

There is the possibility that when two muons are close in phase space, which happens in particular at high-p_{T} where the curvature of the muons in the magnetic field is less, that the two muons are recognized as only a single muon by the trigger. This inefficiency is corrected for by the ρ-factor, defined as:

$$\rho = \frac{\epsilon_{\mu\mu}(\mathrm{MC})}{\epsilon_{\mu,1}(\mathrm{MC}) \cdot \epsilon_{\mu,2}(\mathrm{MC})}. \tag{5.5}$$

The ρ-factor is calculated in different dimuon p_{T} and rapidity bins as a function of $\cos\vartheta$ and φ in the PX frame, individually for the J/ψ, $\psi(2S)$, and $\Upsilon(1S)$ states. The

produced $(\cos\vartheta, \varphi)$ maps are fitted by Eq. 3.12 to show the effect of the rho factor on the angular distributions. The polarization induced by the ρ-factor is shown in Fig. 5.2 as function of p_{T}. The λ_ϑ and λ_φ parameters exhibit a significant transverse and slightly longitudinal trend, respectively, starting at a p_{T} of around 35 GeV/c for the J/ψ around 40 GeV/c for the $\psi(2S)$. The $\Upsilon(nS)$ states, with a higher mass, do not suffer from significant dimuon correlations in the p_{T} range used in the present analysis. Ultimately, the p_{T} is restricted to below 35 GeV/c for all quarkonia states, and any ρ-factor effect is accounted for by applying a systematic uncertainty.

5.1.3 Efficiency of the Dimuon Vertexing Module

The 2011 quarkonia triggers include an online cut on the χ^2 probability of the dimuon vertex fit of 0.5%, which induces a slight inefficiency, which is accounted for by ϵ_{vtx}. This inefficiency was studied using a dedicated dimuon trigger set up identically to the quarkonium trigger, but without the cut on the dimuon vertex χ^2 probability. A T&P analysis was performed using this trigger, and the inefficiency was determined to be quite small. The efficiency correction is applied as a systematic uncertainty for the charmonia analysis and regarded as negligible enough to ignore for bottomonia.

5.2 Overall Polarization Framework

The current polarization methodology was developed in response to the ambiguous polarization measurements mentioned in Sec. 3.2. It is a fully data driven

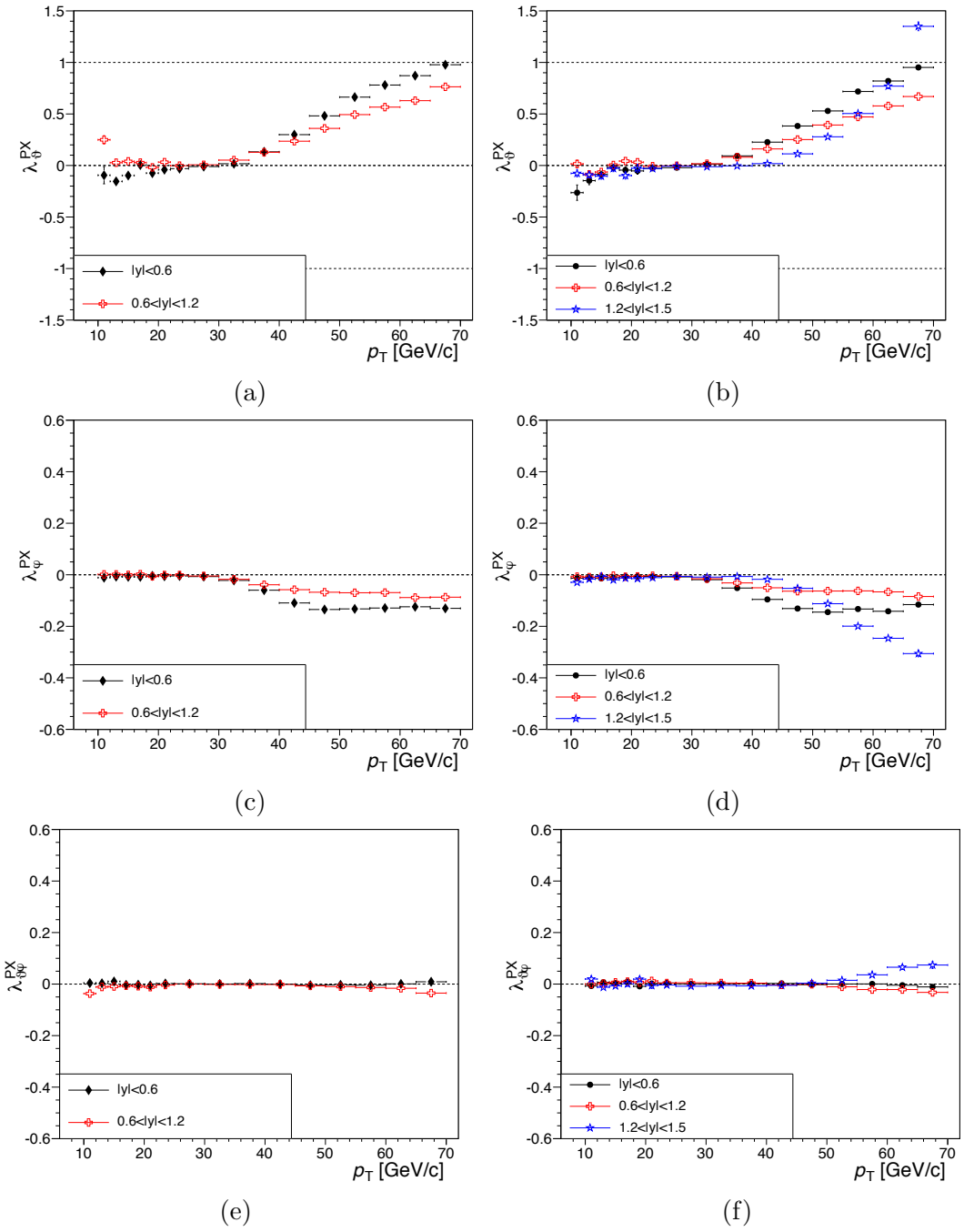

Figure 5.2: The λ_ϑ, λ_φ and $\lambda_{\vartheta\varphi}$ parameters in the PX frame induced by the ρ-factor as functions of p_T, in bins of rapidity, for the J/ψ (a, c, e) and $\psi(2S)$ (b, d, f).

analysis, except for the calculation of the CMS dimuon correlations, which are ultimately used only to assess systematic uncertainties. The analysis requires several internal inputs from the $\psi(nS)$ and $\Upsilon(nS)$ datasets that are obtained through a series of data file preparation steps to provide the following information:

- The muon 4-momentum vectors of events with mass within a specific window around the pole masses of each quarkonium state
- The fraction of background events in the selected sample as determined by fits to the mass, and, in the case of the ψ analysis, the pseudo-proper decay length
- The (p_{T}, $|y|$, $M_{\mu\mu}$, $\cos\vartheta$, φ) distribution of the background events, split into a 2-dimensional ($\cos\vartheta$, φ) and a 3-dimensional (p_{T}, $|y|$, $M_{\mu\mu}$) histogram

The preparation of the data files is done for different ranges of p_{T} and N_{ch}, producing a ROOT file for each different (p_{T}, N_{ch}) bin that contains all of the necessary internal inputs. Splitting the 5-dimensional (p_{T}, $|y|$, $M_{\mu\mu}$, $\cos\vartheta$, φ) distribution into two histograms is justifiable assuming that the ($\cos\vartheta$, φ) distribution does not change within each (p_{T}, $|y|$, $M_{\mu\mu}$) bin, an assumption that will be discussed further in Secs. 5.4.1. Additionally, the analysis requires single muon and dimuon efficiencies as functions of the (di)muon kinematics, which were described in Sec. 5.1.

After preparation, the data files are fed into the polarization extraction framework, which begins with an event-by-event background subtraction, described in Sec. 5.2.1, slightly different for the Υs and the ψs due to the non-prompt contribution in the $\psi(nS)$ signal. The surviving events are considered background free and

the polarization extraction procedure, described in Sec. 5.2.2, can begin.

5.2.1 General Background Subtraction

A background model is built using angular and kinematical distributions from sideband regions near the quarkonium mass pole. Individual events in the signal region, which could be either signal or background, are compared to this model, and backgrounds events are removed using a likelihood-ratio method. The transformation of the background model from one reference frame to another is an exact process, and so it is only necessary to build the background model for one reference frame. Fiducial cuts on single muons impose limits on the angular phase space (see Sec. 5.4.1 for more detail), so the chosen frame for the analysis is the one with the simplest shape, the PX frame (defined in Sec. 3.2).

The general likelihood-ratio method is applied as follows. The background model is built from an appropriate mixture of the left (LSB) and right (RSB) sidebands, specific for each quarkonia state. The model consists of one histogram, $\mathcal{K}_{BG}(p_{\mathrm{T}}, y, M_{\mu\mu})$, containing the kinematic information and another, $\mathcal{A}_{BG}(\cos\vartheta, \varphi)$, containing the angular information of sideband dilepton events. In $\mathcal{K}_{BG}$, p_{T} and y are filled with actual values of the sidebands, but $M_{\mu\mu}$ is a randomly chosen value from the dimuon mass background fit within the respective signal region. For a specific dilepton event, the probability that the event is background, $\mathcal{P}_{BG}(p_{\mathrm{T}}, y, M_{\mu\mu}, \cos\vartheta, \varphi)$, is be calculated as the product of $\mathcal{K}_{BG}(p_{\mathrm{T}}, y, M_{\mu\mu}) \cdot \mathcal{A}_{BG}(\cos\vartheta, \varphi)$. Next, histograms from the signal region, $\mathcal{K}_{S+BG}(p_{\mathrm{T}}, y, M_{\mu\mu})$ and $\mathcal{A}_{S+BG}(\cos\vartheta, \varphi)$, which contain ac-

tual quarkonia signal (S) in addition to background (BG), are used to calculate $\mathcal{P}_{S+BG}(p_{\mathrm{T}}, y, M_{\mu\mu}, \cos\vartheta, \varphi)$ for that same event. These probabilities are then appropriately normalized: $\mathcal{P}_{BG}$ to the fraction of background, f_{BG}, within a particular experimental bin and $\mathcal{P}_{S+BG}$ to unity. At this point, if $\mathcal{P}_{BG}$ is larger than $\mathcal{P}_{S+BG}$, the event is rejected as background. Otherwise, $\mathcal{P}_{S+BG}$ is multiplied by a random number, $r \in [0, 1]$, and rejected if the result is less than $\mathcal{P}_{BG}$. A fraction of events equal to f_{BG} is removed from the sample and surviving events are considered signal. Due to the random component of the method, the background subtraction and subsequent lambda extraction (Sec. 5.2.2) procedure is repeated 50 times to account for any potential fluctuations. Owing to the non-prompt contribution to the charmonia signal, the $\Upsilon(nS)$ and $\psi(nS)$ background models differ slightly, detailed further in Secs. 5.4.3 and 5.5.3, respectively.

The performance of the background subtraction can be established by comparing the subtracted background to the amount from the background model. This is shown in Fig. 5.3, where ratios between the subtracted background distribution and the input background model are plotted against the five background model inputs, $\cos\vartheta$ (a), φ (b), p_{T} (c), dimuon mass (d), and rapidity (e) for a specific $\Upsilon(1S)$ bin. The ratios fluctuate around unity, showing the background subtraction algorithm is quite good. Also plotted (f) is the distribution of the ratio between total background subtracted and total input background, which shows a mean consistent with unity, but highlights the importance of mitigating statistical fluctuations by repeating the procedure 50 times.

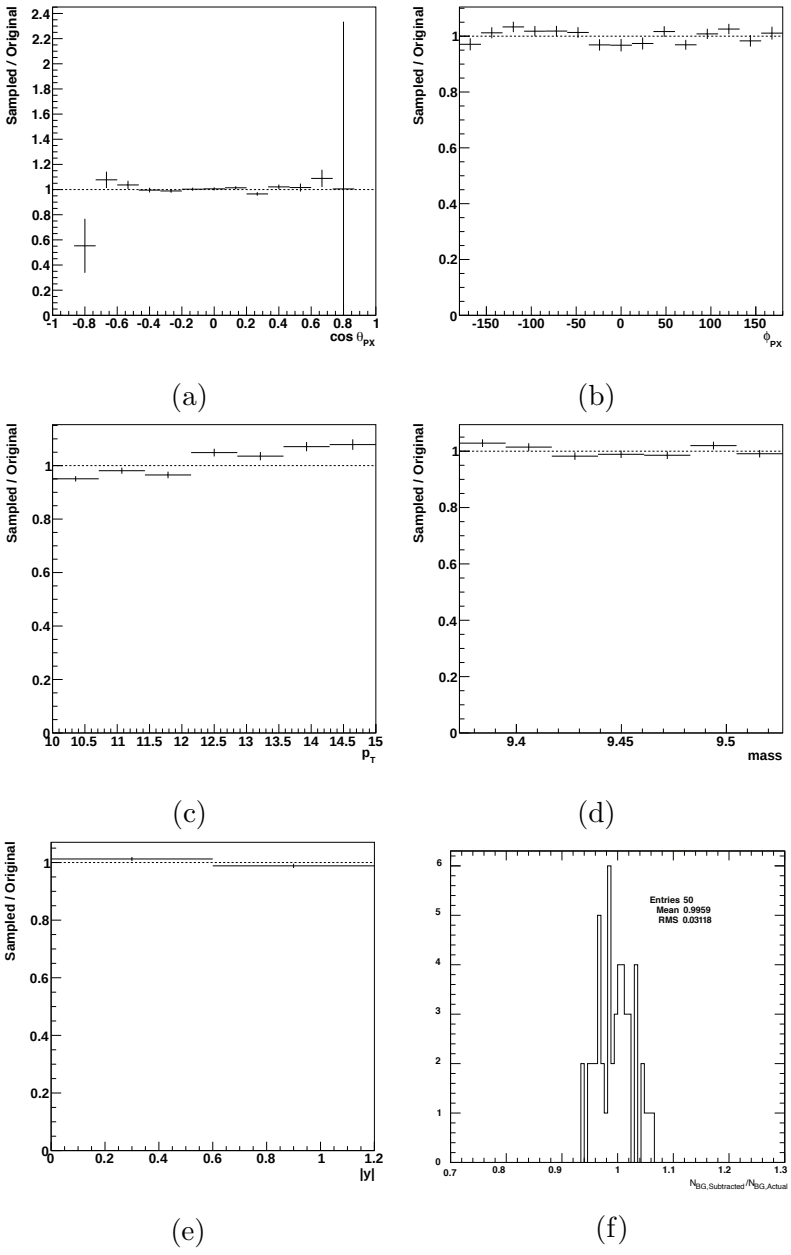

Figure 5.3: Ratios of the amount of background subtracted to the actual amount of background, for the $\Upsilon(1S)$ bin with $10 < p_{\mathrm{T}}^{\mu\mu} < 15$ GeV/c and $0 < N_{\mathrm{ch}} < 10$. The ratios are plotted against $\cos\vartheta$ (a), φ (b), p_{T} (c), dimuon mass (c), and rapidity (e). For each of the 50 background subtractions, the ratio of total background subtracted to total actual background is shown in (f).

5.2.2 Extraction of Polarization Parameters

The extraction of the lambda parameters from the dimuon distribution begins with the definition of the probability density function (PDF) for the kinematic parameters of a given event, $\mathcal{E}$:

$$\mathcal{E}(\vec{p}_1, \vec{p}_2) = \frac{1}{\mathcal{N}(\vec{\lambda})} \cdot W(\cos\vartheta, \varphi|\vec{\lambda}) \cdot \epsilon(\vec{p}_1, \vec{p}_2), \tag{5.6}$$

where $W(\cos\vartheta, \varphi|\vec{\lambda})$ is the dilepton angular distribution, equal to Eq. 3.12, and ϵ is the efficiency correction from Eq. 5.2. $\mathcal{N}$ is a normalization term, calculated by integrating $W \cdot \epsilon$ over $\cos\vartheta$ and φ; however, the efficiency correction is a complicated function of the muon kinematics, and therefore also a function of $\cos\vartheta$ and φ. That is to say, the dimuon data sample is *not unpolarized*, and therefore not uniform over the $\cos\vartheta$ and φ, making an integration over the data sample impossible. Instead, the integration is estimated by uniformly integrating over $\cos\vartheta$ and φ in MC generated muons based on the efficiency and acceptance corrected $(p_{\mathrm{T}}, |y|, M_{\mu\mu})$ data distributions.

The likelihood ($\mathcal{L}(\vec{\lambda})$) is then defined as the product of the probability of every accepted signal event:

$$\mathcal{L}(\vec{\lambda}) = \prod_i \mathcal{E}(\vec{p}_1{}^{(i)}, \vec{p}_2{}^{(i)}). \tag{5.7}$$

The polarization parameters are extracted from $\mathcal{L}(\vec{\lambda})$ using a Bayesian Markov Chain Monte Carlo method that employs a Metropolis-Hastings algorithm [99], resulting in a Posterior Probability Function (PPD) for each of the three frame-dependent

polarization parameters, in each reference frame. The Metropolis-Hasting algorithm works by computing the log-likelihood of a particular point in the polarization parameter space, $\log(\mathcal{L}(\vec{\lambda}_i))$ and comparing to a subsequent sample, $\log(\mathcal{L}(\vec{\lambda}_{i+1}))$. If $\Delta = \log(\mathcal{L}(\vec{\lambda}_{i+1})) - \log(\mathcal{L}(\vec{\lambda}_i)) > 0$, the subsequent point is more likely than the former, so the point is accepted, and the Markov Chain moves forward with the new value. Otherwise, the former point is accepted and the Markov Chain continues with a new subsequent point. All accepted points are used to construct the PPD of the polarization parameters.

The final result of each polarization parameter is taken as the most probable value of each respective 1-dimensional projection of the overall PPD. The statistical uncertainties are evaluated by first fitting the PPD with a Gaussian in a small interval around the maximum value, then using the fit to identify an interval that contains 68.3 % of the total values, including the most probable. The statistical uncertainties are established by identifying two regions, $[-\infty, \vec{\lambda} - \sigma_-]$ and $[\vec{\lambda} + \sigma_+, +\infty]$ and requiring that each contains $0.5 \cdot (100 - 68.3)\%$ of the 1D PPD. An example showing the most probable value and the associated statistical uncertainties of the 1-dimensional PPD is shown in Fig. 5.4, for λ_ϑ^{PX} and λ_φ^{PX}, for a specific $\Upsilon(1S)$ bin.

The application of the background subtraction method and the Metropolis-Hastings algorithm introduces a degree of randomness in the calculation of the polarization parameters. To mitigate these effects, the process is repeated 50 times to produce 50 separate output PPDs. The final estimation of the polarization parameters is extracted after these files are merged, which ensures all uncertainties

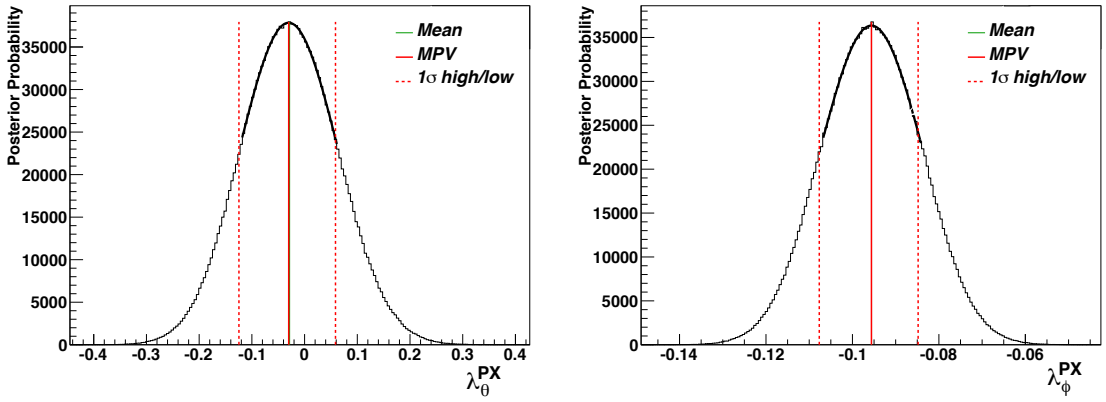

(a) (b)

Figure 5.4: The 1-dimensional PPDs of λ_ϑ^{PX} (a) and λ_φ^{PX} (b) for the $\Upsilon(1S)$, for $10 < p_{\mathrm{T}}^{\mu\mu} < 15$ GeV/c and $0 < N_{\mathrm{ch}} < 10$. The solid red line shows the most probable value, taken as the central value for the polarization measurement. The dashed red lines indicate the 68.3 % closure limit around the central value.

related to the random nature of the procedure are included in the polarization parameter projections. In Fig. 5.5 the two-dimensional $(\lambda_\vartheta^{PX}, \lambda_\varphi^{PX})$ contour plots for a specific kinematic bin of the $\Upsilon(3S)$ are shown at the 68.3 % closure limit, with each line representing the number of times the polarization extraction procedure is performed. The projections stabilize after approximately $n_{\mathrm{fit}} = 30$ repetitions; to be certain, this procedure uses 50 repetitions.

For an estimation of the accuracy of how well the extracted parameters fit the data, Fig. 5.6 shows the background-subtracted $\cos\vartheta^{PX}$ and φ^{PX} data distributions with the best-fit lambda projections, along with the two potential polarization extremes, fully longitudinal and fully transverse.

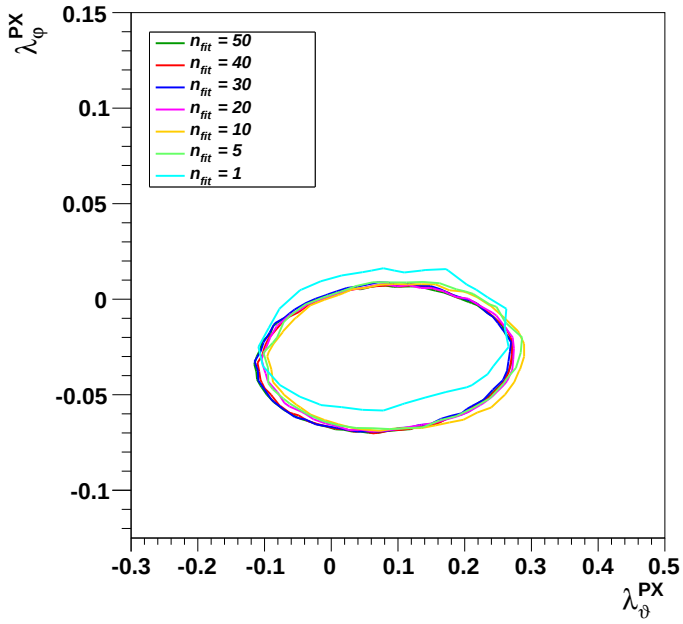

Figure 5.5: Two-dimensional $(\lambda_\vartheta^{PX}, \lambda_\varphi^{PX})$ contour plots at the 68.3 % closure limit for the $\Upsilon(3S)$ in the kinematic bin $|y| < 0.6$ and $20 < p_{\mathrm{T}}^{\mu\mu} < 30$ GeV/c, integrated in multiplicity. Each line represents an evaluation of the parameters after a different number, n_{fit}, of extraction fits.

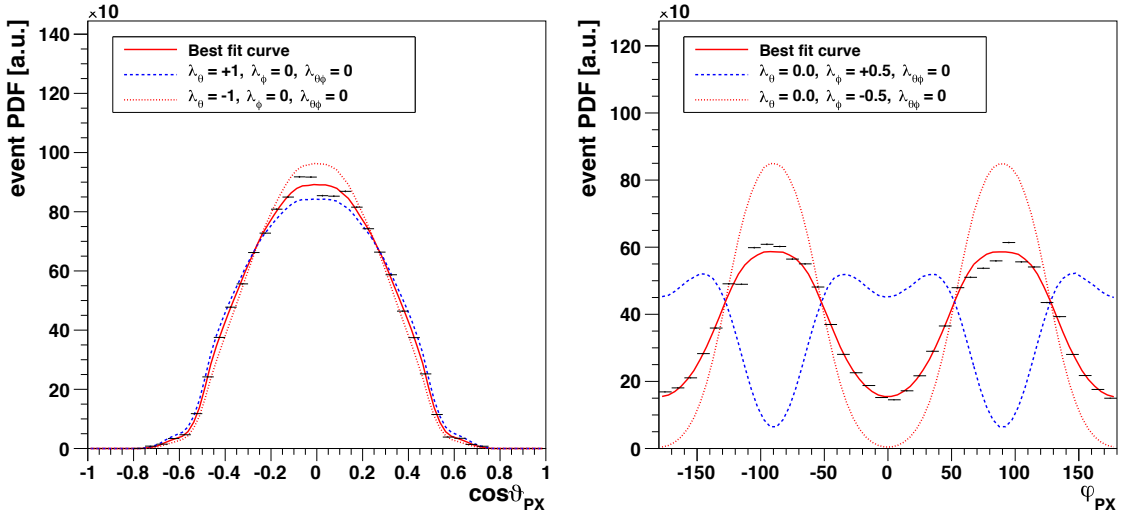

(a) (b)

Figure 5.6: The background-subtracted $\cos\vartheta^{PX}$ (a) and φ^{PX} (b) data distributions for the $\Upsilon(1S)$, for $10 < p_{\mathrm{T}}^{\mu\mu} < 15$ GeV/c and $0 < N_{\mathrm{ch}} < 10$. The solid red curve represents the extracted lambda values, the dashed blue curve shows the expected distribution for a fully transverse measurement, and the dotted red line is that of a fully longitudinal polarization.

5.3 Event Multiplicity Definition

In this analysis, the polarization is measured versus the charged particle multiplicity, N_{ch}, of the event. The N_{ch} variable is calculated during reconstruction of an event by counting "high-purity" [100] tracks with $p_{\mathrm{T}} > 500$ MeV, measured with at least 10 % relative accuracy. Each track, not including the two muons, is assigned a likelihood that it originated from the primary vertex, based on the transverse distance between the track and the primary vertex. N_{ch} is defined as the sum of this likelihood. The N_{ch} distributions of the three datasets are shown in Fig. 5.7. The vertical dashed lines represent the edges of each multiplicity bin.

5.4 Measurement of the $\Upsilon(nS)$ Polarizations

In this section, the polarization analysis of the three $\Upsilon(nS)$ states is detailed. The work is an extension of [64], which measured polarizations against p_{T} and rapidity in $\sqrt{s} = 7$ TeV collisions. This analysis integrates fully over the rapidity and partially over the p_{T} values of the previous analysis, focusing instead on the effect of the particle density on $\Upsilon(nS)$ production. To study this effect, the polarization is measured against the charged particle multiplicity, N_{ch}, defined in Sec. 5.3. The results are published in [89].

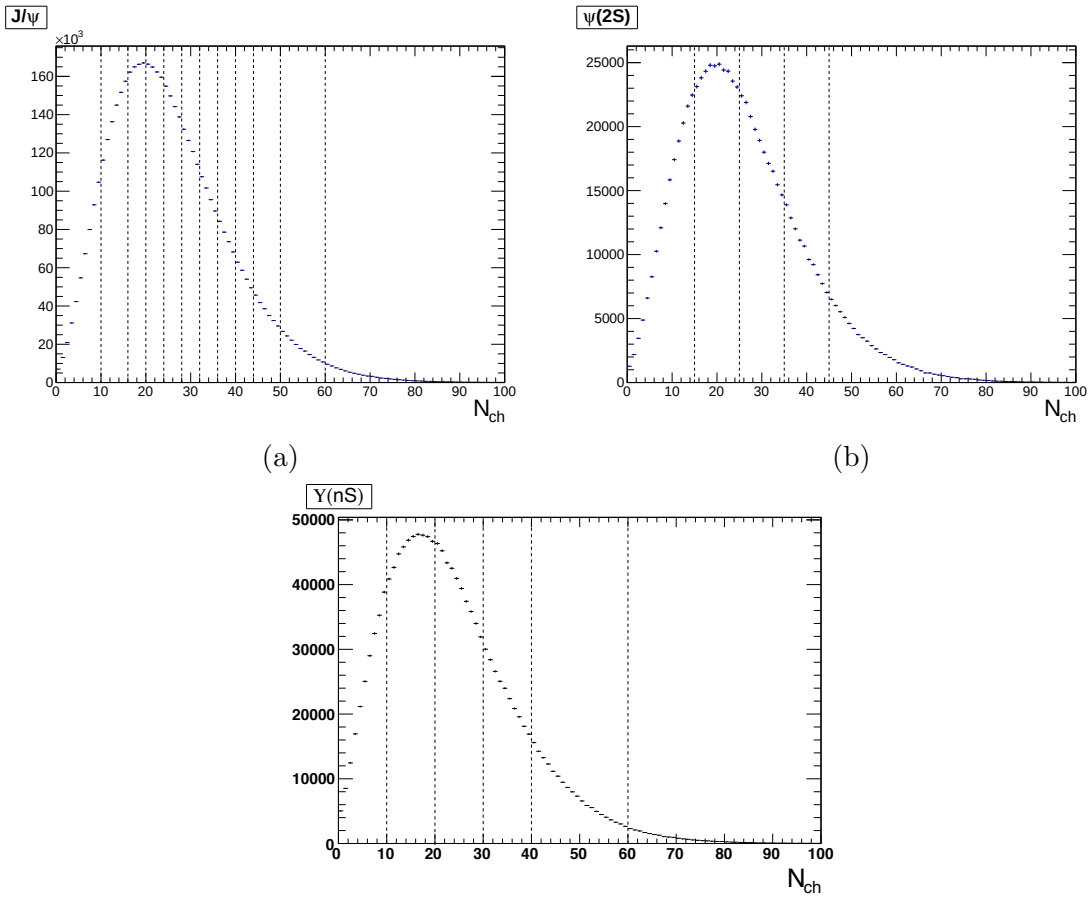

Figure 5.7: The N_{ch} distribution of the J/ψ (a), $\psi(2S)$ (b), and $\Upsilon(nS)$ (c) datasets, with vertical dashed lines indicating edges of the experimental bins.

5.4.1 Event Selection

The data for this analysis was taken during the LHC pp run in 2011, with a total integrated luminosity of 4.9 fb^{-1} collected by the triggers listed in Sec. 4.2.2.1. The muons are reconstructed using the CMS Software suite and applying the standard muon selections, requiring a minimum of 11 hits in the Silicon Tracker, with at least two of those in the Pixel Detector and matched to a track in the Muon System, a maximum distance away from the beam spot, and a χ^2 vertex probability

of $> 1\%$ that the muons originated from the same vertex. Additionally, there was an offline cut on the pseudo-proper decay length significance, $|c\tau/\sigma_{c\tau}| < 2$, where $c\tau = L_{xy}M/p_{\mathrm{T}}$, L_{xy} is the transverse decay length, M is the dimuon invariant mass, and $\sigma_{c\tau}$ is the uncertainty of $c\tau$. Although all muons from $\Upsilon(nS)$ decays are prompt, this last cut is significant because the background is reduced by 25 % at the expense of only 5 % of signal events.

The single muon 2-dimensional (p_{T},$|\eta|$) distribution of the collected data is shown in Fig. 5.8, built from dimuons in mass regions close the the $\Upsilon(nS)$ mass poles. A minimum p_{T} threshold, caused by the strong magnetic field, is seen near 3.3 GeV/c at midrapidity, and decreases further as rapidity increases. Once the minimum threshold is crossed, the muon detection increases abruptly, indicative of reaching the detector efficiency turn-on regions described in Sec. 5.1.1. These minimum thresholds restrict the analysis to the single muon safe fiducial region given in Eq. 5.4.

Imposing the fiducial cuts has consequences on the $(\cos\vartheta, \varphi)$ phase space, restricting the coverage, especially at low p_{T}. This is illustrated in Fig. 5.9, where (a) and (b) show the $(\cos\vartheta^{PX}, \varphi^{PX})$ distribution of the $\Upsilon(2S)$ in a lower p_{T} range ($10 < p_{\mathrm{T}}^{\mu\mu} < 15$ GeV/c) is restricted compared to the higher p_{T} range ($15 < p_{\mathrm{T}}^{\mu\mu} < 35$ GeV/c) in (c) and (d). Comparing (a) and (c), with a multiplicity $0 < N_{\mathrm{ch}} < 10$, against (b) against (d) with $40 < N_{\mathrm{ch}} < 60$, indicates there is no effect of multiplicity on the phase space coverage. The effect of p_{T} on the phase space coverage for the other $\Upsilon(nS)$ states is similar to the presented figures. Because the angular $\cos\vartheta$ distribution closest to ± 1 discriminates the most between a transverse and longitudinal

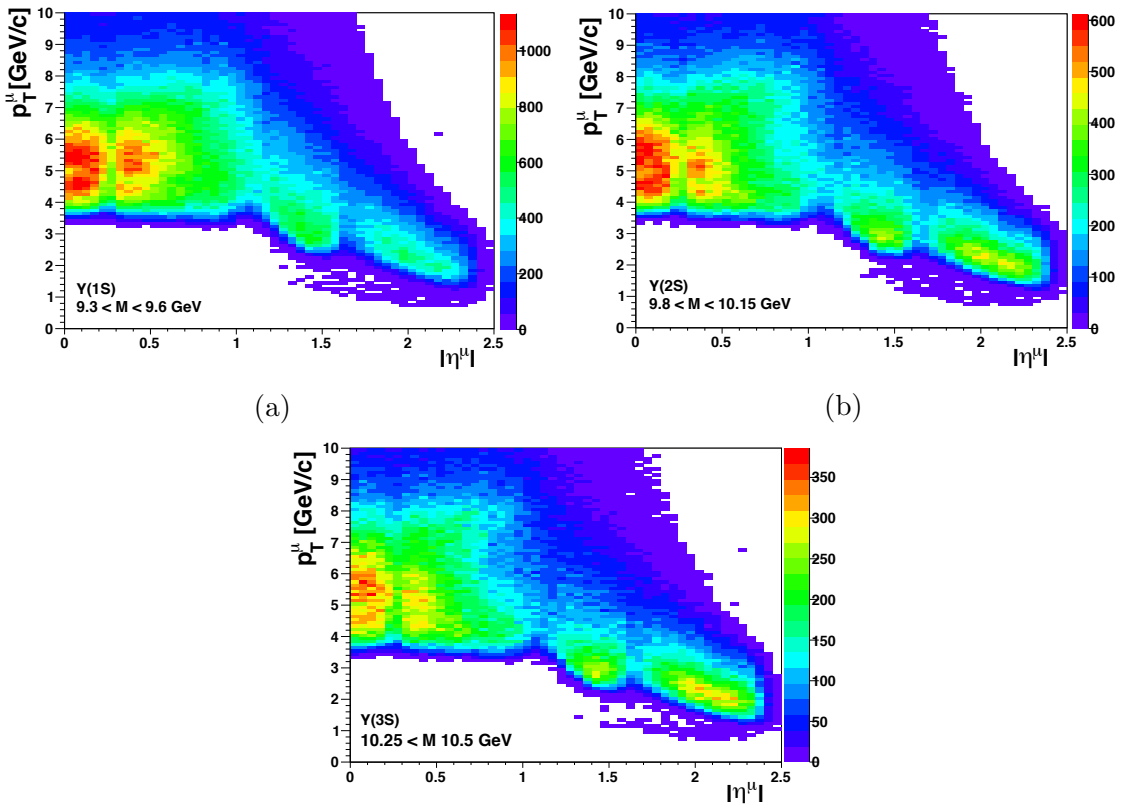

(a) (b) (c)

Figure 5.8: The 2-dimensional $p_{\mathrm{T}} - |\eta|$ distributions of single muons build from the dimuon data sample around the mass poles of the $\Upsilon(1S)$ (a), $\Upsilon(2S)$ (b), and $\Upsilon(3S)$ (c).

polarization, this restriction in phase space makes the polarization measurements much more difficult at lower p_{T}. In the previous analysis [64], measurements below $p_{\mathrm{T}}^{\mu\mu} = 10$ GeV/c are considered to be unreliable, so the measurement against multiplicity takes this p_{T} value as the minimum. As long as the p_{T} bins are kept sufficiently narrow, the $(\cos\vartheta^{PX}, \varphi^{PX})$ distribution will not change so much as to introduce a bias into the framework, and the 5-dimensional kinematic and angular distribution histogram may be split into two histograms, as mentioned in Sec. 5.2.

A final cut in the analysis is made after studying the migration of events from one N_{ch} bin to the next by looking for any trends in the cross section fractions of

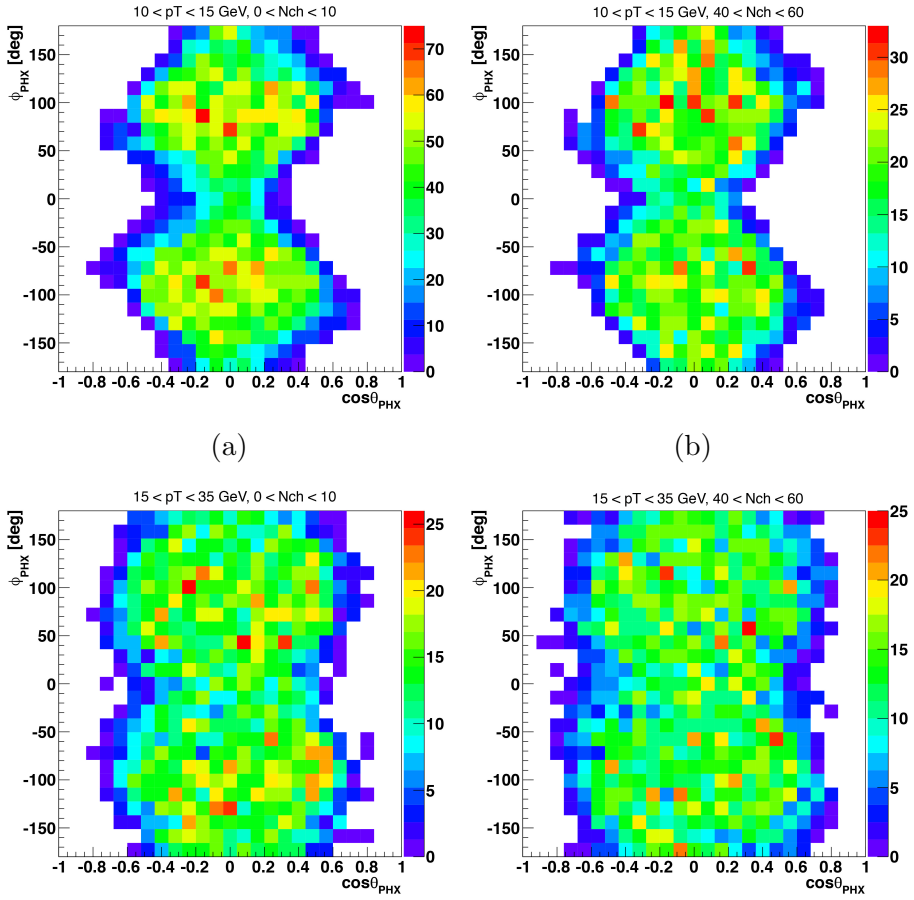

(a) (b)

(c) (d)

Figure 5.9: Two-dimensional $\cos\vartheta^{PX}, \varphi^{PX}$ angular distributions for the $\Upsilon(2S)$ for $10 < p_{\mathrm{T}}^{\mu\mu} < 15$ GeV/c and $0 < N_{\mathrm{ch}} < 10$ (a), $10 < p_{\mathrm{T}}^{\mu\mu} < 15$ GeV/c and $40 < N_{\mathrm{ch}} < 60$ (b), $15 < p_{\mathrm{T}}^{\mu\mu} < 35$ GeV/c and $0 < N_{\mathrm{ch}} < 10$ (c), and $15 < p_{\mathrm{T}}^{\mu\mu} < 35$ GeV/c and $40 < N_{\mathrm{ch}} < 60$ (d).

each bin. Event migration could potentially be caused by inadvertently counting spurious tracks produced in nearby pileup vertices, biasing the results. The check is shown in Fig. 5.10; fractions are generally steady until there are 15 pileup collisions (i.e. 16 primary vertices). Therefore, an offline cut excluding any event with more than 16 primary vertices is performed.

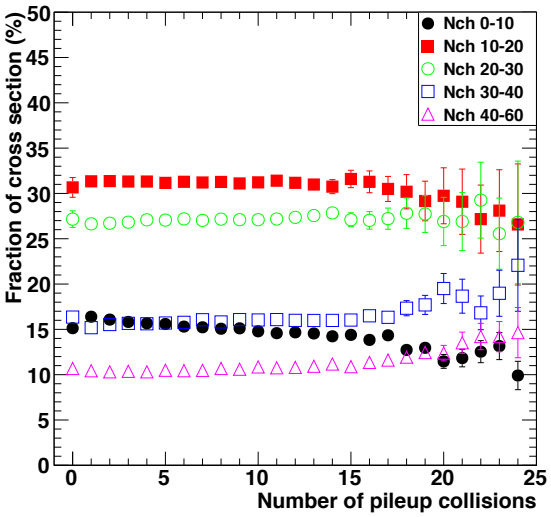

Figure 5.10: The percent cross section of each multiplicity bin for the full $\Upsilon(nS)$ dataset, after all analysis selection cuts, plotted against the number of pileup collisions.

5.4.1.1 Definition of $\Upsilon(nS)$ Experimental Bins

In the present analysis, to split the events into N_{ch} bins with a limited number of events, the other kinematical variables are partially integrated. Integration over the p_{T} and rapidity is justified because the previous measurements showed no significant variation with either kinematic variable [63, 64]. The rapidity variable could be fully integrated so that there is one rapidity bin, $|y| < 1.2$. The p_{T} could only be partially integrated, given that the $(\cos\vartheta, \varphi)$ phase space coverage changes with p_{T}, and a basic tenant of the background subtraction method is that the phase space coverage does not change within a p_{T} bin. Therefore, two p_{T} ranges are defined, $10 < p_{\text{T}}^{\mu\mu} < 15$ and $15 < p_{\text{T}}^{\mu\mu} < 35$ GeV/c. The higher-p_{T} bin could be broader than the lower-p_{T} bin because the phase space changes most drastically at lower-p_{T}. For each $\Upsilon(nS)$ state, the p_{T} bins are then differentiated into five N_{ch} bins, with edges

at $N_{\mathrm{ch}} = 0$, 10, 20, 30, 40, and 60, except for the low-p_{T} $\Upsilon(3S)$ state, for which the highest two multiplicity bins are merged.

5.4.2 $\Upsilon(nS)$ Mass Fit

Modeling the dimuon invariant mass spectrum for each $\Upsilon(nS)$ peak is essential for the polarization analysis. The background fraction, f_{BG}, established through the mass fit, is a necessary component of the background subtraction method, as described in Sec. 5.2.1. Additionally, the definition of the sidebands depends on the resolution of the mass peaks, which is also provided through fits to the signal peaks. The fit is performed in two steps: first, sidebands are preliminarily defined as $8.6 - 8.9$ and $10.6 - 11.4$ GeV/c^2, which are fitted with a second-order polynomial to define the background. Next, each signal peak is fitted with a single Crystal Ball (CB) function, giving a total of four fits - one CB per $\Upsilon(nS)$ state plus the background polynomial. CB functions are four parameter functions built from a Gaussian core, accounting for two of the parameters, μ_{CB} and σ_{CB}, along with a power-law tail that models the effects of final-state radiation with the remaining terms, n_{CB} and α_{CB}.

In this analysis, μ_{CB} and σ_{CB} of the $\Upsilon(1S)$ are free parameters, but μ_{CB} of the $\Upsilon(2S)$ and $\Upsilon(3S)$ are fixed to their Particle Data Group values. The heavier state σ_{CB} values are also fixed using Particle Data Group mass values by assuming a linear relationship with the particle mass: $\sigma_{\Upsilon(nS)} = \sigma_{\Upsilon(1S)} \cdot M_{\Upsilon(nS)}/M_{\Upsilon(1S)}$. The power-law tail parameters are left as free, and are assumed to be identical for all

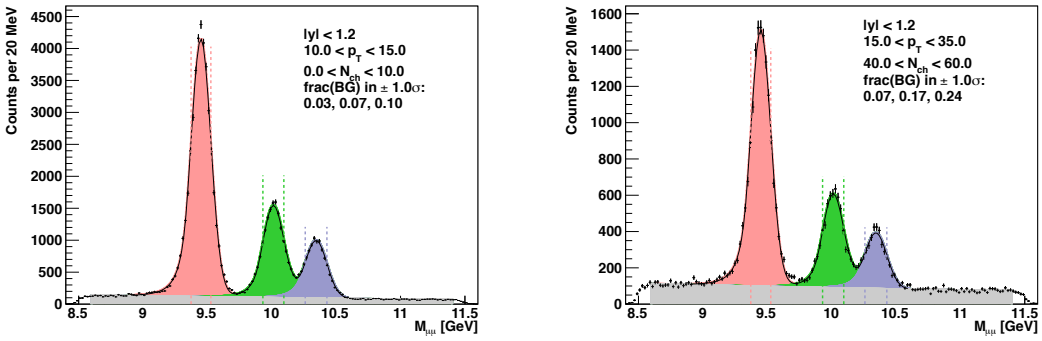

(a) (b)

Figure 5.11: The fitted $\Upsilon(nS)$ invariant mass spectrum for a low-p_{T}, low-N_{ch}bin ((a), $10 < p_{\mathrm{T}}^{\mu\mu} < 15$ GeV/c, $0 < N_{\mathrm{ch}} < 10$) and a high-p_{T}, high-N_{ch}bin ((b), $15 < p_{\mathrm{T}}^{\mu\mu} < 35$ GeV/c, $40 < N_{\mathrm{ch}} < 60$). The four different fit regions are indicated by color: $\Upsilon(1S)$ in red, $\Upsilon(2S)$ in green, $\Upsilon(3S)$ in blue, and background in gray. The dash, vertical lines indicate a 1 σ region surrounding each mass peak.

$\Upsilon(nS)$ states. Figure 5.11 shows each of the four distinct fits to the invariant mass spectrum, distinguished by color, for the lowest (a) and the highest (b) p_{T} and N_{ch} bins, clearly indicating that there is little change in resolution across the measured bins.

Once the mass peaks have been fitted, the sidebands and signal region (SR) may be defined:

$$\begin{aligned} LSB &: 8.6 < M_{\mu\mu} < M^{fit}_{\Upsilon(1S)} - n_{\sigma}^{LSB} \cdot \sigma_{\Upsilon(1S)} \text{ GeV}/c, \\ SR &: M^{fit}_{\Upsilon(nS)} - n_{\sigma}^{SR} \cdot \sigma_{\Upsilon(nS)} < M_{\mu\mu} < M^{fit}_{\Upsilon(nS)} + n_{\sigma}^{SR} \cdot \sigma_{\Upsilon(nS)} \text{ GeV}/c, \\ RSB &: M^{fit}_{\Upsilon(3S)} + n_{\sigma}^{RSB} \cdot \sigma_{\Upsilon(3S)} < M_{\mu\mu} < 11.4 \text{ GeV}/c, \end{aligned} \tag{5.8}$$

where $n_{\sigma}^{LSB} = 4$, $n_{\sigma}^{RSB} = 3$, and $n_{\sigma}^{SR} = 1$. The LSB is necessarily further away from the SR due to a greater amount of signal contamination stemming from the final-state radiation tail into the LSB. The rationale for using $n_{\sigma} = 1$ to define the

SR is twofold. The detector resolution is such that the $\Upsilon(2S)$ and $\Upsilon(3S)$ peaks overlap, and setting $n_\sigma = 3$ would increase the amount of cross-contamination of the states. With $n_\sigma = 1$, cross-contamination is minimized, never reaching a value greater than 2.5 %, as shown in Fig. 5.12. Furthermore, as discussed in Sec. 5.4.4.1, the uncertainty associated with the background model is generally the dominant systematic uncertainty, so maximizing the signal to background ratio is paramount to limiting the uncertainties in the measurement. Figure 5.13 shows curves of the signal yield (green), background amount (blue), and the signal to background ratio (red), as a function of n_σ, normalized to one, demonstrating the importance of restricting the width of the signal mass window. This restriction does, however, inject a kinematical bias, which is explained in Sec. 5.4.2.1.

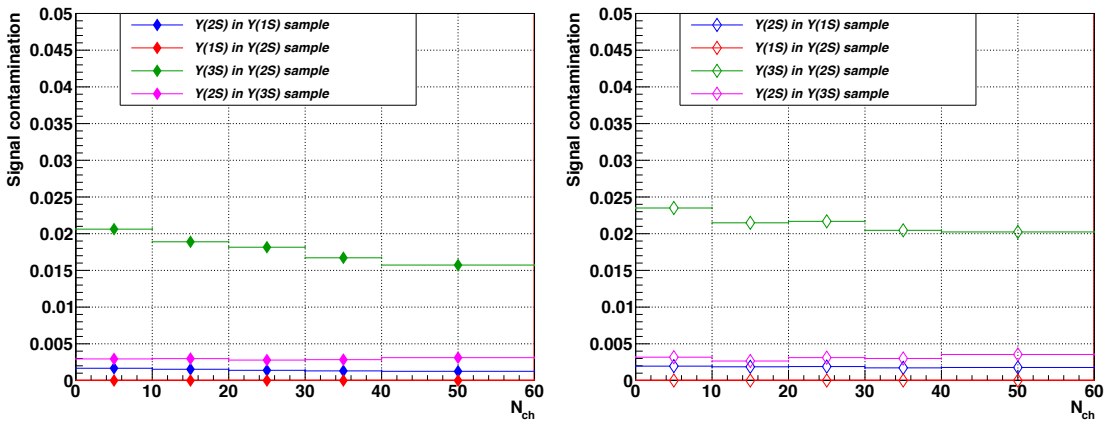

(a) (b)

Figure 5.12: The amount of cross-contamination of $\Upsilon(nS)$ in the $\Upsilon(mS)$ signal, for the low-p_{T} (a) and high-p_{T} (b) ranges, for each N_{ch} bin.

The background fraction is then extracted by integrating the signal and background functions within a 1σ window around the $\Upsilon(nS)$ pole masses. Similarly, the yield of each $\Upsilon(nS)$ within the SR is estimated. Figure 5.14a shows f_{BG} for all

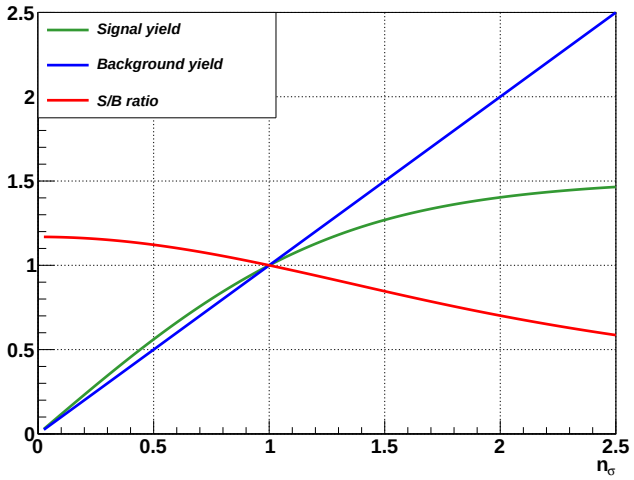

Figure 5.13: Signal (green) and background (blue) yields, along with the signal to background ratio (red) as a function of n_σ, normalized to $n_\sigma = 1$.

$\Upsilon(nS)$ states in both p_{T} ranges, which increases linearly with N_{ch}, and is larger in heavier $\Upsilon(nS)$ states and at lower p_{T}. The estimated yields are shown in Fig. 5.14b, in which the lowest statistic bin, the highest p_{T} and N_{ch} $\Upsilon(3S)$ bin, has greater than 2000 events, sufficient for a polarization measurement. In the case of the low-p_{T} $\Upsilon(3S)$ state, the fourth and fifth N_{ch} bins are ultimately merged in an effort to lessen the total systematic uncertainties.

5.4.2.1 Kinematical Correction

By setting $n_\sigma = 1$ and rejecting the tails of the dimuon mass peaks, a significant source of systematic uncertainty in the analysis is curtailed, yet this effectively cuts on the opening angle between the two muons. Naturally, this affects the decay angular distribution and introduces a bias in the polarization measurements. The bias was analyzed by the Quarkonia Polarization Group for the publication of the N_{ch}-integrated study and discussed in the thesis of Valentin Knünz [88]. This section

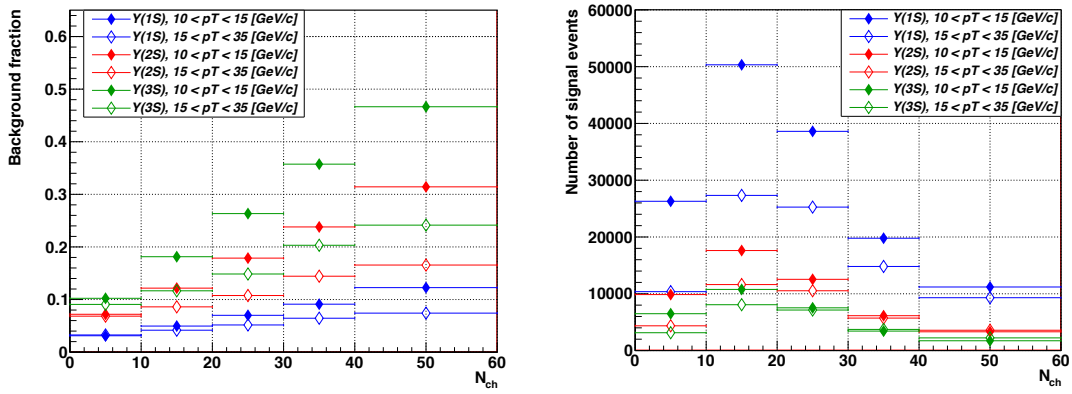

(a) (b)

Figure 5.14: The background fraction, f_{BG}, (a) and the estimated number of events within the defined SR (b), for the three $\Upsilon(nS)$ states, in each p_{T} range, plotted against N_{ch}.

presents a summary of the work.

This kinematic bias was studied using MC datasets to establish a kinematical correction, $\Delta\vec{\lambda}^{n_\sigma}$, of the initial polarization parameter measurement, $\vec{\lambda}^{n_\sigma}$, to produce the corrected parameter, $\vec{\lambda}'$:

$$\vec{\lambda}' = \vec{\lambda}^{n_\sigma} + \Delta\vec{\lambda}^{n_\sigma}. \tag{5.9}$$

The correction was obtained by measuring the polarization of a MC dataset and setting $n_\sigma = 10$, which effectively removes any cut on the dimuon mass, and then repeating the analysis with a more reasonable n_σ, such as $n_\sigma = 1$ for this particular analysis. The difference between the two values is set as $\Delta\vec{\lambda}^{n_\sigma}$. The corrections are calculated for the three $\Upsilon(nS)$ states, independently for each of the three reference frames, as a function of p_{T} and rapidity. The bias was found to be identical for the three $\Upsilon(nS)$ states, so the values are combined to increase the statistical accuracy of the correction parameter. The polarization parameters with the largest bias, λ_φ

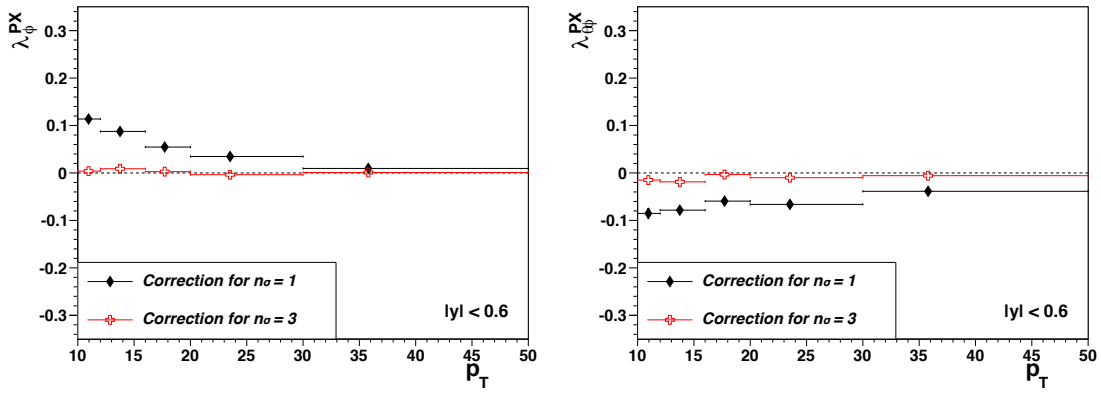

(a) (b)

Figure 5.15: The kinematical corrections of λ_φ (a) and $\lambda_{\vartheta\varphi}$ (b) for the $\Upsilon(nS)$ states as a function of p_{T}, for the $|y| < 0.6$ region. The red points show negligible corrections when $n_\sigma = 3$, the black points show larger corrections when $n_\sigma = 1$.

and $\lambda_{\vartheta\varphi}$ at mid-rapidity, are provided in Fig. 5.15 (a) and (b), respectively. The figure shows the correction for both $n_\sigma = 1$ and $n_\sigma = 3$, with the latter showing, as expected, negligible corrections.

As this bias is a kinematic effect, it is independent of N_{ch}, therefore, in this analysis the kinematical corrections are calculated by simply using the average dimuon p_{T} and $|y|$ in each N_{ch} bin to evaluate the bias correction from the previous analysis.

5.4.3 $\Upsilon(nS)$ Background Model

The general method of the background subtraction is introduced in Sec. 5.2.1. This section describes the construction of the background model from the sideband regions that is used as input for the background subtraction method. The process for building the model begins by defining the LSB and RSB according to Eq. 5.8 and filling histograms containing the kinematic and angular distributions of the

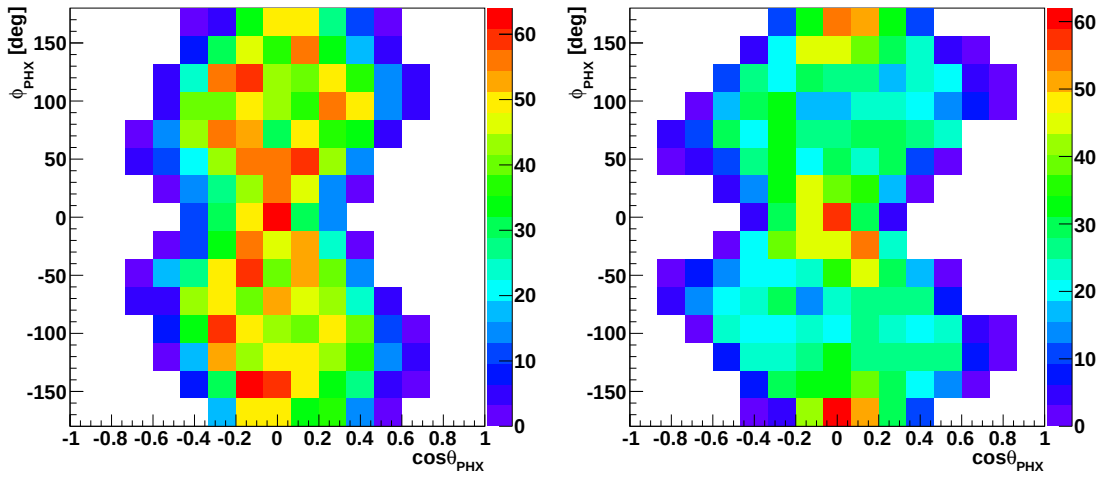

Figure 5.16: Angular distribution of muons in the LSB (a) and RSB (b) for the $\Upsilon(1S)$, for $10 < p_{\rm T}^{\mu\mu} < 15$ GeV/c and $0 < N_{\rm ch} < 10$.

sidebands to give the following four histograms: $h^{LSB}_{p_{\rm T},|y|,M_{\mu\mu}}$, $h^{RSB}_{p_{\rm T},|y|,M_{\mu\mu}}$, $h^{LSB}_{\cos\vartheta,\varphi}$, and $h^{RSB}_{\cos\vartheta,\varphi}$. An example of the $(\cos\vartheta,\varphi)$ distribution of the LSB (a) and RSB (b) of a particular $\Upsilon(1S)$ bin is shown in Fig. 5.16, showing that the background distribution clearly changes with $M_{\mu\mu}$.

To create a reliable mixture of the two sidebands, the simplest assumption is that the angular and kinematic distributions change monotonically between the LSB and RSB, so that the background model histograms $\mathcal{K}_{BG}(p_{\rm T},y,M_{\mu\mu})$ and $\mathcal{A}_{BG}(\cos\vartheta,\varphi)$ can be created from a linear combination of the normalized sideband histograms:

$$\mathcal{K}_{BG}(p_{\rm T},y,M_{\mu\mu}) = f_{LSB}\cdot h^{LSB}_{p_{\rm T},|y|,M_{\mu\mu}} + (1-f_{LSB})\cdot h^{RSB}_{p_{\rm T},|y|,M_{\mu\mu}},$$

$$\mathcal{A}_{BG}(\cos\vartheta,\varphi) = f_{LSB}\cdot h^{LSB}_{\cos\vartheta,\varphi} + (1-f_{LSB})\cdot h^{RSB}_{\cos\vartheta,\varphi},$$

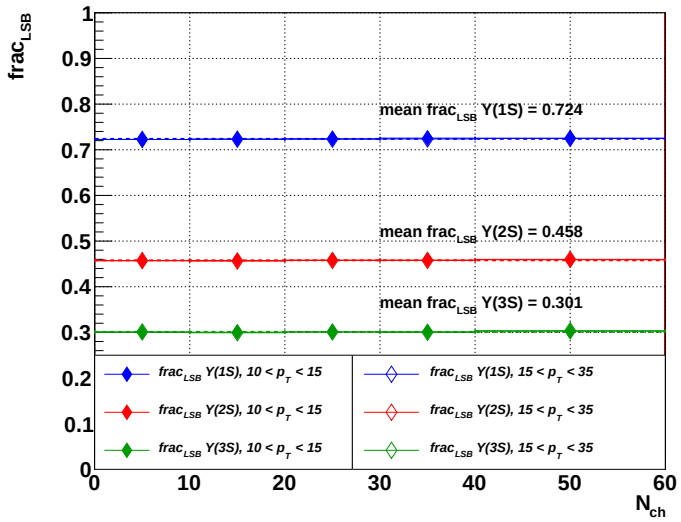

Figure 5.17: f_{LSB} of the $\Upsilon(1S)$ (blue), $\Upsilon(2S)$ (red), and $\Upsilon(3S)$ (green), in both p_{T} bins, against N_{ch}. The high p_{T} bin (open diamonds) lies exactly under the low p_{T} points, and so it cannot be seen.

where f_{LSB} represents the weighting of the LSB. This value varies for each $\Upsilon(nS)$ state so that $\Upsilon(1S)$, closest to the LSB, has the largest f_{LSB}, followed by the $\Upsilon(2S)$ and $\Upsilon(3S)$. The f_{LSB} values are calculated using the background mass fit to determine the mass median in the LSB (M_{LSB}) and RSB (M_{RSB}), and linearly interpolating the value based on the mass of each $\Upsilon(nS)$ state:

$$f_{LSB} = \frac{M_{LSB} - M_{\Upsilon(nS)}}{M_{RSB} - M_{LSB}}. \tag{5.10}$$

The values, shown in Fig. 5.17, are seen to be independent of kinematics and event multiplicity and the values are calculated to be $f_{LSB}^{\Upsilon(nS)} = 72, 46, 30\%$ for the three states.

The assumption of linearity was tested with data by treating the background regions as data and feeding it through the polarization framework, which allows

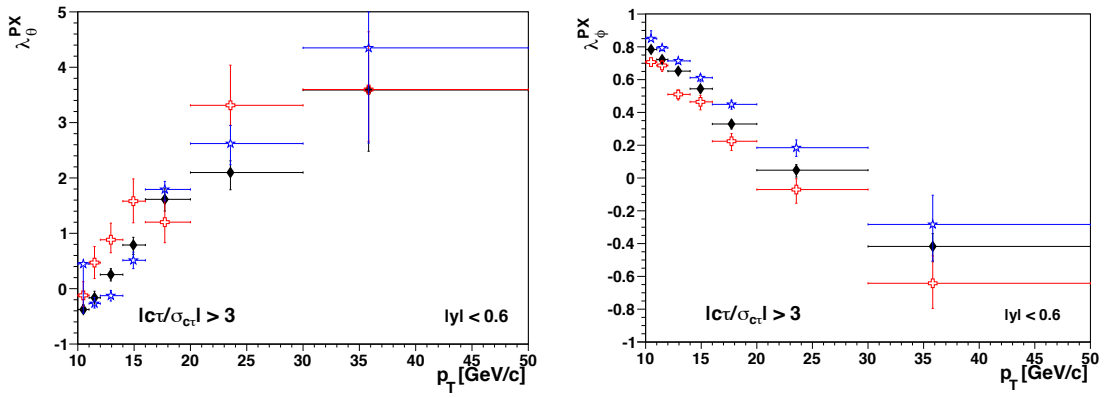

(a) (b)

Figure 5.18: The extracted λ_ϑ (a) and λ_φ (b) parameters of the LSB (red points), RSB (blue), and SR (black) as a function of p_{T}, with $|y| < 0.6$ for events with a lifetime significance $|c\tau/\sigma_{c\tau}| > 3$.

for a measurement of the $\vec{\lambda}$ parameters as a function of the background mass. To ensure the samples are not contaminated with data, the samples are restricted to events with $|c\tau/\sigma_{c\tau}| > 3$, which eliminates any signal, as the Υs decay promptly. The lifetime significance cut also allows for a SR test, since all signal is effectively cut. The measured $\vec{\lambda}$ parameters, though physically meaningless, do still represent a measurement of the $(\cos\vartheta, \varphi)$ distribution in the different mass regions. The extracted parameters are shown in Fig. 5.18, showing that the SR (black points) lies in between the LSB (red) and RSB (blue), though some bins that suffer from poor statistics buck this trend. The $\vec{\lambda}$ parameters are also extracted for sideband events with $|c\tau/\sigma_{c\tau}| < 3$, which exhibited a similar trend. As a further cross check, the $\vec{\lambda}$ parameters are extracted from samples with mass windows with $n_\sigma = 1$ and $n_\sigma = 3$ and compared. The results are compatible, showing that the background model and subtraction is quite reliable, even when presented with increased background fractions.

5.4.4 Evaluation of the $\Upsilon(nS)$ Systematic Uncertainties

There are several systematic uncertainties that must be considered in the $\Upsilon(nS)$ polarization analysis. The types of systematic uncertainties can be grouped into two categories: $N_{\rm ch}$-dependent uncertainties, that affect each bin to a different magnitude, and $N_{\rm ch}$-independent global uncertainties, that are dependent on event kinematics, but not by the event multiplicity. The background model uncertainty is calculated using data, but the remainder of the systematic uncertainties are evaluated with toy-MC experiments.

The toy-MC experiments are performed by generating pseudo-data with any desired polarization, and therefore a matching $(\cos\vartheta, \varphi)$ distribution, in a particular reference frame. The number of generated events and the background fractions are set by the user depending on the goals of a particular pseudo-experiment. The events are generated around the Particle Data Group mass peaks [44], assuming a Gaussian mass distribution with $\sigma = 0.1$ GeV/c^2. The distribution of the background mass and the dimuon rapidity are chosen to be flat. The $p_{\rm T}$ distribution is generated based on a fit to data [101]. The angular distribution is then adjusted to account for the measured detector efficiencies by looking up the total efficiency value for each event and comparing it to a randomly generated number, $r \in [0, 1]$. If the event efficiency is larger than r, it is considered efficient and stored. These pseudo-data are then propagated to the polarization framework to determine the $\vec{\lambda}$ parameters. The particular efficiency used for the polarization extraction may be different from the one used to adjust for detector effects, allowing for a study of any systematic

effects associated with each single muon or dimuon efficiency.

All of the systematic tests using toy-MC make use of $n_{toy} = 50$ individual pseudo-experiments, which includes the generation of a new psuedo-dataset for each iteration. Any potential bias is evaluated as the median of the difference between the injected and extracted polarizations from the 50 pseudo-experiments. For $N_{\rm ch}$-dependent systematics, each uncertainty is directly incorporated into the extracted PPD for each individual $\vec{\lambda}$ by interpreting the bias as the width of a Gaussian, centered around the most probable value of the $\vec{\lambda}$ PPD. The exception is the background model uncertainty, in which the probability distribution is assumed to be flat. Then, for each entry in the $\vec{\lambda}$ PPD, a value, $\Delta\vec{\lambda}$, is extracted from the systematic PPD and added to the original value of the $\vec{\lambda}$ PPD. This process, repeated individually for each systematic uncertainty, effectively smears the $\vec{\lambda}$ PPD. The $N_{\rm ch}$-independent uncertainties are treated more simply. As they are assumed to affect each point within a specific kinematic range identically, the global uncertainties are quadratically added and indicated by a common error band in the final results.

5.4.4.1 Background Model Uncertainty

The systematic uncertainty related to the background model uncertainty is related to the choice of f_{LSB}, and the test is performed using data. By varying f_{LSB}, the composition of the background model will change. As a rather conservative test of the background model, f_{LSB} is varied by $\pm 28\%$ to give a 100% closure limit result. The rationale for this variation is that $f_{LSB}^{\Upsilon(1S)} + 28\% = 1$. The $N_{\rm ch}$-dependent

background model uncertainty is generally the dominant systematic uncertainty in the analysis.

5.4.4.2 Uncertainty of the Polarization Extraction Framework

The uncertainty associated with the polarization extraction framework itself is studied through three tests to identify the effects of limited statistics, background polarizations, and the polarization itself. Toy-MC tests were devised to study these effects, separately for each $\Upsilon(nS)$ state as functions of $N_{\rm ch}$.

The first test is performed by generating events with zero signal and background polarization. The number of generated events is set to match the f_{BG} and event yields measured in data. The resulting bias is quite small, and is assigned as the systematic uncertainty. In the systematic summary plots in Sec. 5.4.4.4, this is labelled as Framework I.

The second test evaluates any bias associated with extracting different potential polarizations. For this test, 50,000 $\Upsilon(1S)$ events are generated with $f_{BG} = 0$, no background polarization, and injecting the following signal polarizations:

- $\lambda_\vartheta^{PX} = +0.5, \lambda_\varphi^{PX} = \lambda_{\vartheta\varphi}^{PX} = 0$
- $\lambda_\vartheta^{PX} = -0.5, \lambda_\varphi^{PX} = \lambda_{\vartheta\varphi}^{PX} = 0$

The bias is taken as the mean of the absolute values of the difference between the injected and extracted polarization. The systematic uncertainty is common for each $\Upsilon(nS)$ state, but individually evaluated for each experimental bin. This is called Framework II in the systematic summary plots in Sec. 5.4.4.4.

The final test is to ensure reliable background subtraction of different background polarization scenarios. For each $\Upsilon(nS)$ state and experimental bin, 50,000 events are generated with no signal polarization, f_{BG} values measured from data, and the following background scenarios:

- $\lambda_{\vartheta}^{PX} = 0, \lambda_{\varphi}^{PX} = +0.8, \lambda_{\vartheta\varphi}^{PX} = 0$
- $\lambda_{\vartheta}^{PX} = +2, \lambda_{\varphi}^{PX} = +0.4, \lambda_{\vartheta\varphi}^{PX} = 0$
- $\lambda_{\vartheta}^{PX} = +4, \lambda_{\varphi}^{PX} = -0.4, \lambda_{\vartheta\varphi}^{PX} = 0$

For the systematic bias, labelled as Framework III, the difference between the injected and extracted polarizations of each scenario is quadratically added.

5.4.4.3 Uncertainty Related to the Muon Efficiencies

All potential systematic biases related to the muon efficiencies are considered to be $N_{\rm ch}$-independent global uncertainties, and are treated differently than the $N_{\rm ch}$-dependent uncertainties. The different global uncertainties are initially evaluated as functions of $N_{\rm ch}$, then total global uncertainty is constructed by taking the largest value from each potential source of bias, for each $\vec{\lambda}$ parameter, in each $p_{\rm T}$ range, and quadratically adding the values.

The T&P model is evaluated by generating and reconstructing 50,000 background free toy-MC events using MC truth efficiencies, but then extracting the polarizations using MC T&P efficiencies. The resulting uncertainty is negligible, and treated as common across the three $\Upsilon(nS)$ states. The values fluctuate with

N_{ch}, and the largest value for each $\vec{\lambda}$ parameter, in each p_{T} range is used for the global uncertainty.

The parametrization of the T&P efficiencies is studied similarly to the T&P model, again generating 50,000 background free toy-MC events, this time using the central parametrization of the measured T&P efficiencies. The polarization is then extracted with each of the six different parameterizations mentioned in Sec. 5.1.1. The mean of the biases from the three positive and three negative parameterizations are separately averaged, and then the averages are quadratically added. Again, the biases fluctuated with N_{ch}, and the largest values are taken for the global uncertainty.

The dimuon correlation correction, the ρ-factor, which is not applied because it had only a small effect in the measured p_{T} range, is accounted for using a constant uncertainty. The maximum effect is taken to be $\delta\vec{\lambda} = (0.05, 0.01, 0.01)$, for λ_ϑ, λ_φ, $\lambda_{\vartheta\varphi}$, respectively.

5.4.4.4 Summary of Systematic Uncertainties

All potential systematic uncertainties, including those determined to be N_{ch}-independent, for the frame dependent $\vec{\lambda}$ parameters are presented in Figs. 5.19–5.21. In the figures, the individual biases have been differentiated by color, with the three separate framework uncertainties as blue, red, and light green, the parametrization of the muon efficiencies in yellow, the rho factor uncertainty in purple, the T&P model in magenta, and the background uncertainty in brown. The biases are stacked and compared to the statistical uncertainty, in dark green, for each mea-

sured bin. The systematic uncertainties generally have similar magnitudes, except in the highest $N_{\rm ch}$ bins and the lowest $p_{\rm T}$ range, where the background model uncertainty dominates, especially for the $\Upsilon(2S)$ and $\Upsilon(3S)$ states. For the $\Upsilon(1S)$ state and in the HX frame, the $N_{\rm ch}$-dependent systematic uncertainties are ~ 0.1 for λ_ϑ and $\sim 0.03 - 0.05$ for λ_φ and $\lambda_{\vartheta\varphi}$, slightly increasing with $N_{\rm ch}$. The corresponding $\Upsilon(2S)$ and $\Upsilon(3S)$ values are slightly larger: ~ 0.2 for λ_ϑ, ~ 0.04 for λ_φ, and $\sim 0.05 - 0.08$ for $\lambda_{\vartheta\varphi}$. The statistical uncertainties are negligible for the $\Upsilon(1S)$ state and become dominant for the $\Upsilon(2S)$ and $\Upsilon(3S)$ states, as $N_{\rm ch}$ increases. The values of the $N_{\rm ch}$-dependent systematic uncertainties in the PX frame were quadratically added and listed in the Appendix, in Tables A.1-A.3. The global uncertainties are given in Table A.4.

As an additional cross check to ensure that the systematic uncertainties are sufficiently under control, the differences between the $\tilde{\lambda}$ measurements in the three measured frames are compared to the *total* systematic uncertainty, which is calculated by quadratically adding all $N_{\rm ch}$-dependent and global systematics. The $\tilde{\lambda}$ parameter is frame independent, and so any difference between frames should be limited to within the systematic uncertainty of the measurement. This closure test is presented in Fig. 5.22 for the three $\Upsilon(nS)$ states, showing no evidence that there are any unidentified sources of systematic uncertainty.

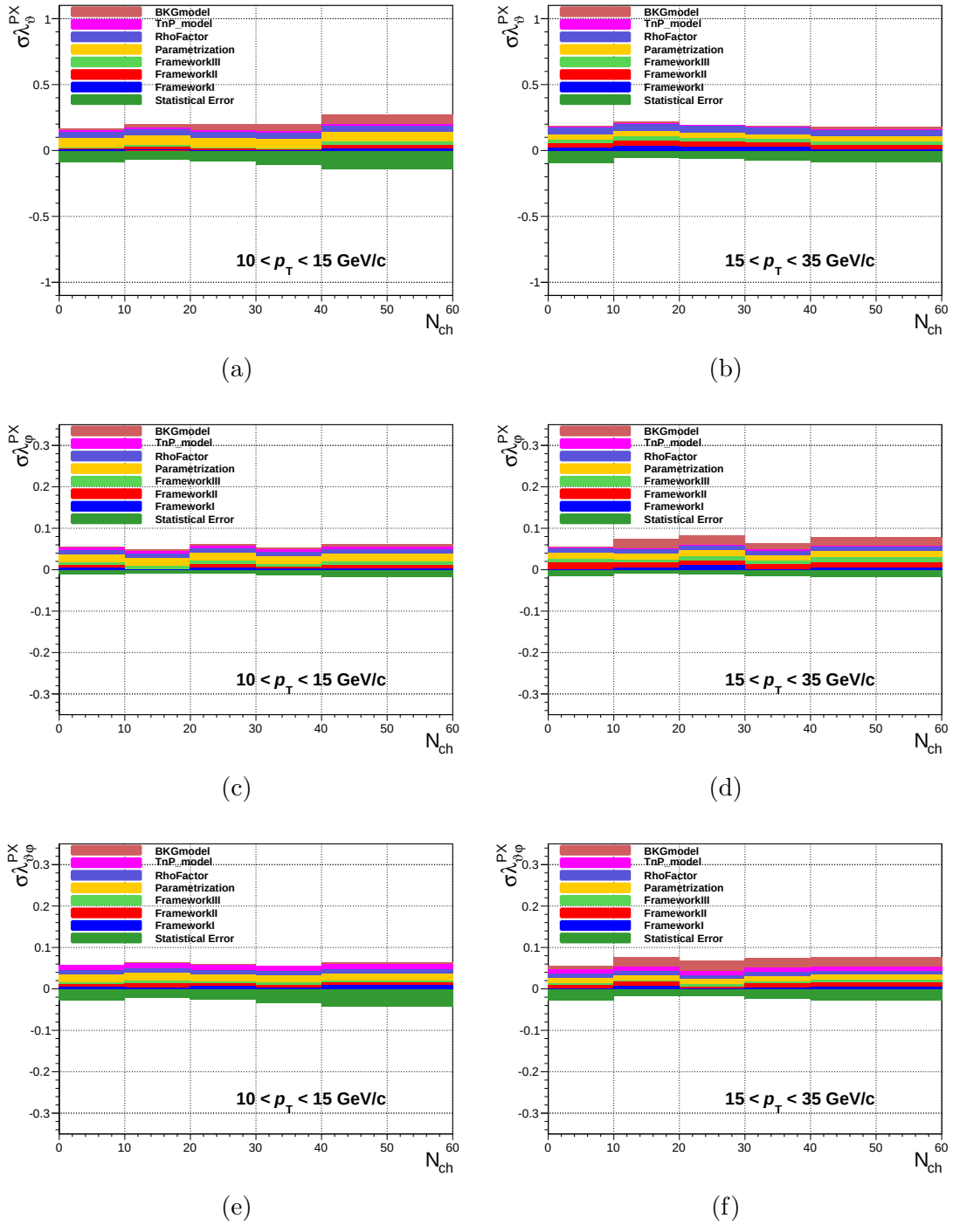

Figure 5.19: Systematic uncertainties, stacked on the positive side, affecting the $\Upsilon(1S)$ λ_{ϑ}^{PX} (a, b), λ_{φ}^{PX} (c, d), and $\lambda_{\vartheta\varphi}^{PX}$ (e, f) parameters, for $10 < p_{\mathrm{T}} < 15$ GeV/c (left column) and $15 < p_{\mathrm{T}} < 35$ GeV/c (right column), compared to the statistical uncertainties on the negative side.

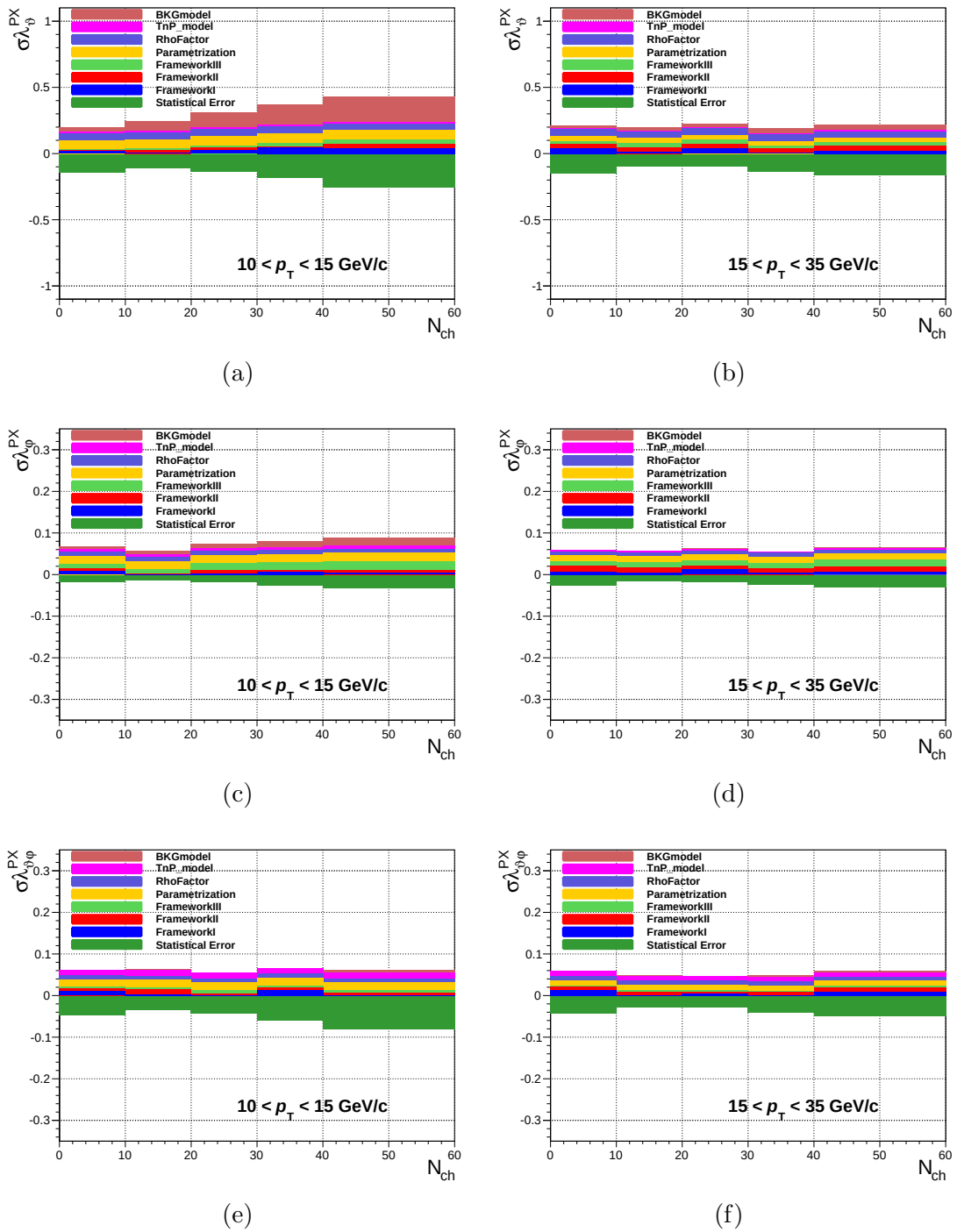

Figure 5.20: Same as Fig. 5.19, except for the $\Upsilon(2S)$.

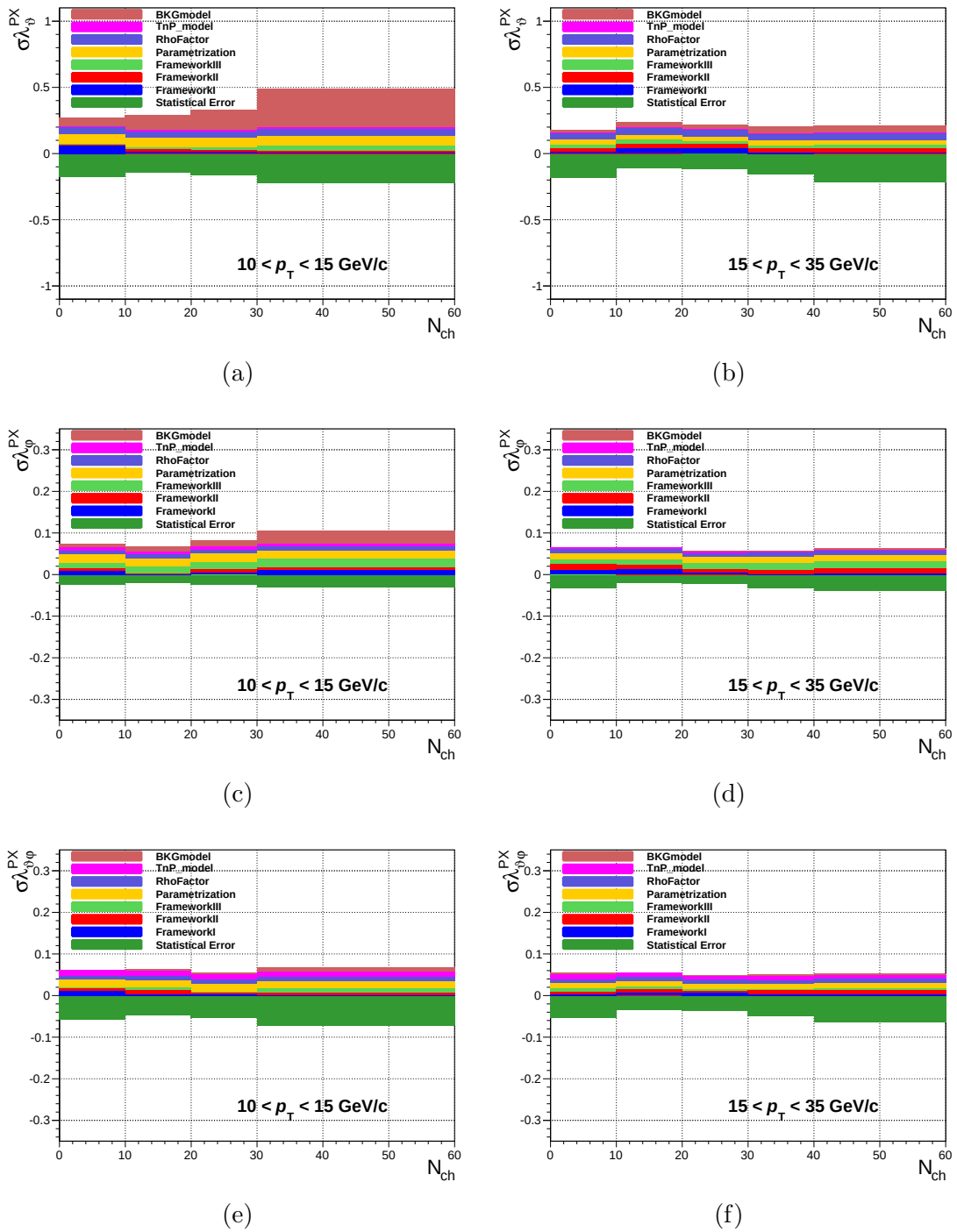

Figure 5.21: Same as Fig. 5.19, except for the $\Upsilon(3S)$.

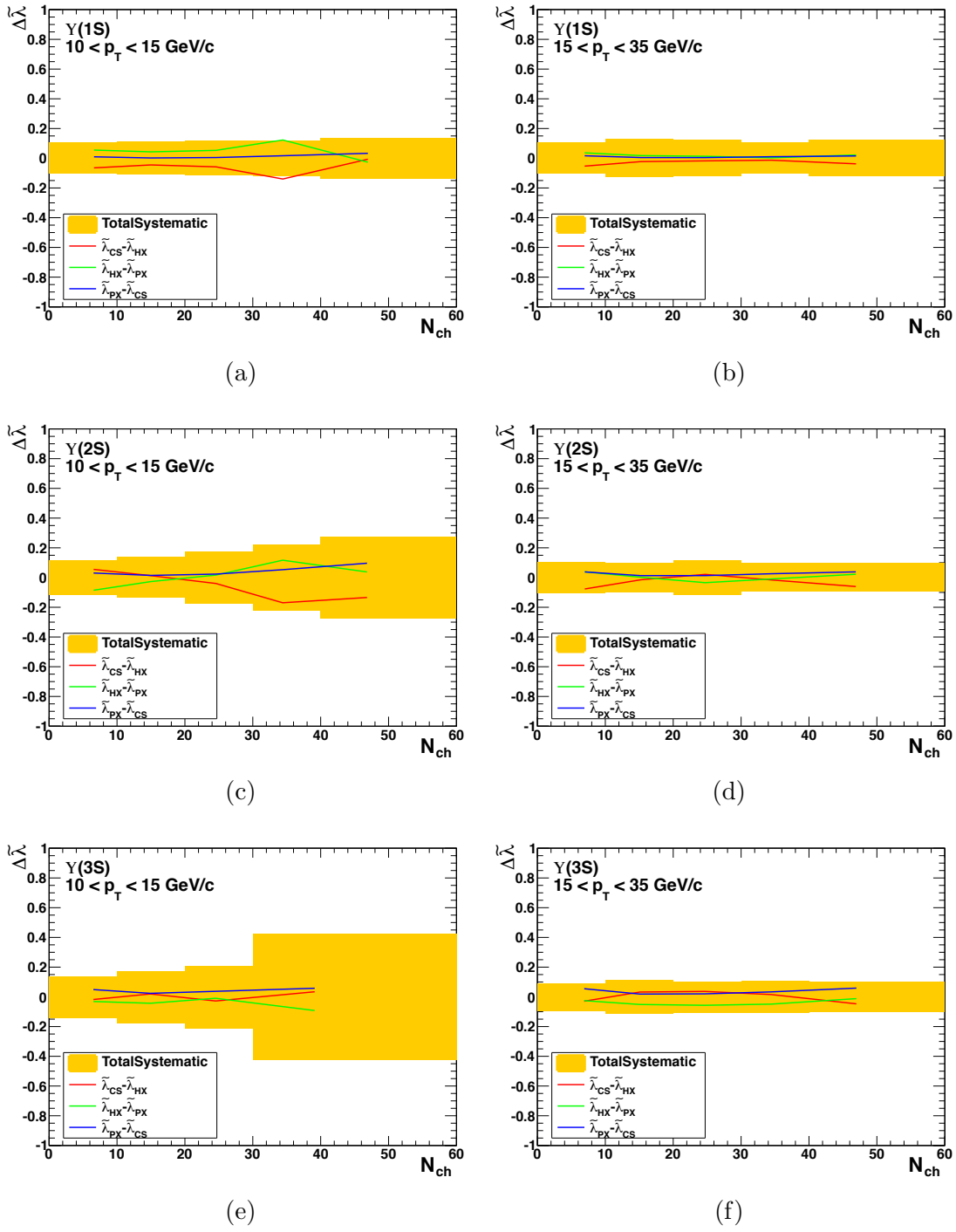

Figure 5.22: Comparison of the total systematic uncertainties to the difference between the $\tilde{\lambda}$ parameters from the different reference frames. The $\Upsilon(nS)$ states are listed top to bottom from lightest to heaviest, in the p_{T} ranges $10 < p_{\mathrm{T}} < 15$ GeV/c (left column) and $15 < p_{\mathrm{T}} < 35$ GeV/c (right column).

5.5 Measurement of the $\psi(nS)$ Polarizations

In this section, the measurement of the polarizations of the $\psi(nS)$ mesons is presented measured against $N_{\rm ch}$. This analysis is an extension of the rapidity- and $p_{\rm T}$-differentiated analysis of [63]. The $\psi(nS)$ mesons suffer from a large non-prompt contribution, originating from the decay of B-mesons, which makes preparation of the analysis data files more complicated, as now a lifetime fit must be performed. This complexity propagates through to the creation of the background model, which must additionally remove non-prompt $\psi(nS)$ events from the sample. The polarization extraction is then identical to the $\Upsilon(nS)$ analysis, as described in Sec. 5.2.

5.5.1 Event Selection

The data used for the $\psi(nS)$ analysis was collected alongside the $\Upsilon(nS)$ dataset already described, with a total integrated luminosity of 4.9 fb^{-1} collected during the 2011 LHC pp run. The online triggers were described in Sec. 4.2.2.1, requiring an opposite sign dimuon pair to be within $2.8 < M_{\mu\mu} < 3.35$ or $3.35 < M < 4.05$ GeV/c^2, respectively for the J/ψ and $\psi(2S)$. Offline, the same standard muon selections used for the $\Upsilon(nS)$ dataset were applied to each of the $\psi(nS)$ datasets. The $\psi(nS)$ datasets *did not* include the additional lifetime significance cut that was applied to the $\Upsilon(nS)$ dataset. Like the $\Upsilon(nS)$ analysis, to prevent any potential event migration between $N_{\rm ch}$ bins, an offline cut is also performed for any event with more than 16 primary vertices.

These selections create a single muon 2-dimensional ($p_{\rm T}$,$|\eta|$) distribution that

is very similar to that from the $\Upsilon(nS)$ dataset, which intuitively makes sense. The distributions are shown in Fig. 5.23. Naturally, the muon threshold is apparent in these datasets as well, and so the analysis is again restricted to the single muon safe fiducial region given in Eq. 5.4. Recall that this cut on low-p_{T} muons induces restrictions in the $(\cos\vartheta, \phi)$ phase space, resulting in a similar effect on the $\psi(nS)$ angular distributions to what was seen in Fig. 5.9, though the effect is increased due to the lower mass of the $\psi(nS)$ states. For this reason, the $\psi(nS)$ analysis is restricted to $p_{\mathrm{T}}^{\mu\mu} > 14$ GeV/c.

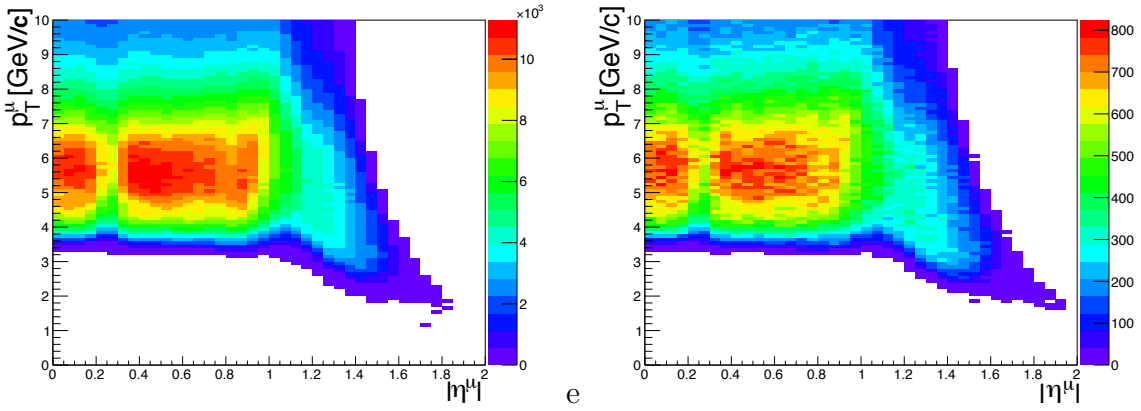

(a) e (b)

Figure 5.23: The 2-dimensional $p_{\mathrm{T}} - |\eta|$ distributions of single muons composed of dimuon events around the mass poles of the J/ψ (a) and $\psi(2S)$ (b).

5.5.1.1 Definition of $\psi(nS)$ Experimental Bins

Analogously to the $\Upsilon(nS)$ analysis, the rapidity and p_{T} variables are integrated relative to the N_{ch}-integrated study. The J/ψ analysis is integrated over the full available rapidity range, $|y| < 1.2$. For the $\psi(2S)$, which did not have a rapidity restriction imposed on the trigger, the range extends out to $|y| < 1.5$. To stay

within the measured rapidity range from the N_{ch}-integrated study, higher rapidity events are not considered. The $\psi(nS)$ is again integrated into two p_{T} ranges, though the low end of the range is necessarily higher due to $(\cos\vartheta, \varphi)$ limitations caused by the fiducial cuts. The edges of the p_{T} bins for the $\psi(nS)$ states are set at p_{T} $= 14, 20$, and 35 GeV/c. The maximum value is chosen to coincide with where the ρ-factor begins to have a significant effect on J/ψ measurements, so by staying below this value, the ρ-factor can be treated as a systematic uncertainty, simplifying the measurement with an insignificant loss of statistics. The high statistic J/ψ could be differentiated into 12 narrow N_{ch} bins, with edges at $N_{\mathrm{ch}} = 0$, 10, 16, 20, 24, 28, 32, 36, 40, 44, 50, 60, and 100. The $\psi(2S)$ had five bins, with edges at $N_{\mathrm{ch}} = 0$, 15, 25, 35, 45, and 100. The bins are shown in the N_{ch} distribution presented in Fig. 5.7.

5.5.2 $\psi(nS)$ Mass and Lifetime Fit

The measurements of J/ψ and $\psi(2S)$ are complicated by a large amount of feed-down from B-mesons, necessitating a mass-lifetime analysis to remove non-prompt $\psi(nS)$ from the sample along with the continuum background. To do this, a background model is developed using contributions from both mass and lifetime fits. The long-lived B-mesons travel much further in the detector than prompt $\psi(nS)$ states, which immediately decay. This property naturally leads to a distribution of how far a particle travels prior to decaying, which can be measured with very good precision at CMS.

The dimuon mass spectrum is fitted with two CB functions, detailed in Sec. 5.5.2.1,

which defines the mass signal and sideband regions, and obtains the fraction of continuum background. Then, a maximum likelihood fit is applied to the pseudo-proper lifetime distribution simultaneously in the mass signal region and the mass sidebands, described further in Sec. 5.5.2.2. This gives the fraction of non-prompt events in the signal region. This produces high quality fits for both the mass and lifetime distributions. This portion of the analysis was developed by Ilse Krätschmer and is covered more thoroughly in her Ph.D. thesis [87].

5.5.2.1 $\psi(nS)$ Mass Fit

In general, the $\psi(nS)$ mass fits are quite similar to the fits of the Υ mass spectrum described in Sec. 5.4.2. The biggest difference is that the $\psi(nS)$ mass distribution is fit with two Crystal Ball functions instead of one. The decision to have a second CB function is in order to maintain as much in common as possible with the N_{ch}-integrated analysis, which required the second function to accommodate for the changing dimuon mass resolution within the rapidity cells.

The CB functions are described by four parameters: μ_{CB} and σ_{CB} describe the Gaussian core of the distribution; n_{CB} and α_{CB} describe the non-Gaussian tail. The same mean, μ_{CB}, is imposed on both CB functions, and the width of each is fixed to the values established in the N_{ch}-integrated analysis as constant values $\sigma_{CB1} = 0.021$ and $\sigma_{CB2} = 0.034$ for J/ψ and 3.686/3.097[2] times those values for $\psi(2S)$ [87]. As in [87], n_{CB} is set to 2.5, but now additionally α_{CB} is fixed to 1.85, again as established in the previous analysis.

[2]The $\psi(2S)$ to J/ψ mass ratio.

As in the $\Upsilon(nS)$ mass fit, the continuum background is described using an exponential, but now the signal M_{sig} is described by the two CBs, added together and weighted by the relative normalization, f_{CB_1}, so that

$$M_{sig}(m_{\mu\mu}) = f_{CB_1} \cdot CB_1(m_{\mu\mu}|\mu_{CB}, \sigma_{CB_1}, \alpha_{CB}) + (1 - f_{CB_1}) \cdot CB_2(m_{\mu\mu}|\mu_{CB}, \sigma_{CB_2}, \alpha_{CB}). \tag{5.11}$$

f_{CB_1} is a free parameter of the fit, allowing some freedom in establishing the effective width of the mass fit, σ_m, which is defined as the weighted average of the widths of the two CB functions:

$$\sigma_m = \sqrt{f_{CB_1} \cdot (\sigma_{CB_1})^2 + (1 - f_{CB_1}) \cdot (\sigma_{CB_2})^2}. \tag{5.12}$$

This process produces very good fits. The extreme cases are shown in Fig. 5.24 for the low-p_{T}, low-N_{ch} J/ψ (a) and high-p_{T}, high-N_{ch} $\psi(2S)$ (b) bins.

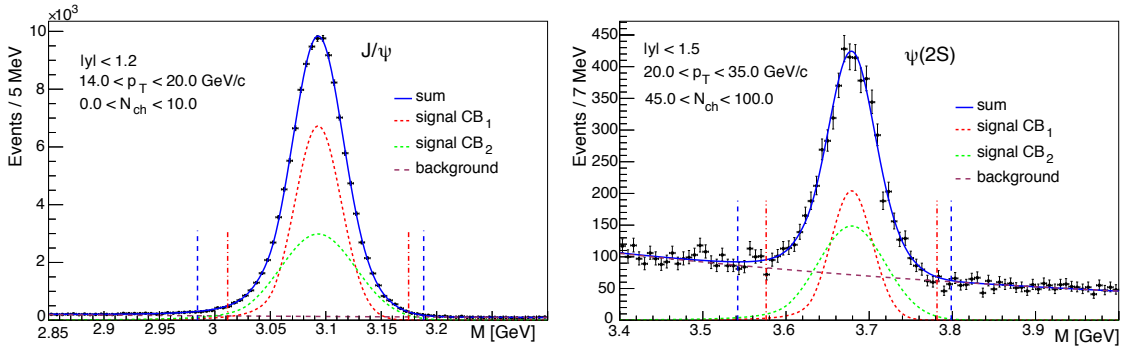

(a) (b)

Figure 5.24: Fitted mass spectra for the J/ψ for $14 < p_{\mathrm{T}} < 20$ GeV/c and $0 < N_{\mathrm{ch}} < 10$ (a) and $\psi(2S)$ for $20 < p_{\mathrm{T}} < 35$ GeV/c and $45 < N_{\mathrm{ch}} < 100$ (b). The two CB functions are drawn with the dashed red and green curves. The continuum background fit is shown with larger, purple dashes. The total fit is shown in blue. The vertical dashed lines represent the signal region (in between the red dashed lines) and the sideband regions (to the left and right of the blue dashed lines).

The mass SR and sidebands are described as in Eq. 5.8, except in this case where $n_\sigma^{LSB} = 4$, $n_\sigma^{RSB} = 3.5$, and $n_\sigma^{SR} = 3$. Again, the LSB is set further away from the RSB to decrease contamination from the final-state radiation tail in the LSB. Unlike the $\Upsilon(nS)$ SR, the $\psi(nS)$ is allowed a larger window because the background model systematic uncertainty is quite small compared to the $\Upsilon(nS)$ uncertainty. The uncertainty is greatly diminished because the mass region between the two $\psi(nS)$ is large enough that the RSB of the J/ψ does not even overlap with the LSB of the $\psi(2S)$, and the mass sidebands are much closer to their respective $\psi(nS)$ states, allowing for an interpolation across a much narrower mass range to create the background model.

5.5.2.2 $\psi(nS)$ Lifetime Fit

To separate the prompt and non-prompt contributions, a fit is made to the pseudo-proper lifetime (ℓ) distribution. The pseudo-proper lifetime is a measure of the distance between the dimuon and the primary vertex, calculated by:

$$l = L_{xy} \cdot M_{\mu\mu}/p_{\mathrm{T}}, \tag{5.13}$$

where L_{xy} is transverse decay length in the laboratory frame, determined after calculating the primary vertex excluding the muon tracks, and $M_{\mu\mu}$ is the dimuon mass. The value is deemed "pseudo" because the lifetime is measured assuming the ψ kinematics, instead of the B-meson kinematics, so the boost from laboratory to center-of-mass frame is only approximate.

The distribution of ℓ is modeled by a Gaussian with an exponential tail, and the distribution is filled very differently by prompt and non-prompt events. The former contribution is found only within the initial Gaussian peak, while non-prompt events are the sole contributor to the exponential tail, but are also present under the Gaussian. The Gaussian behavior is modeled by building a lifetime PDF using the per-event error information provided by the vertex reconstruction algorithm:

$$\mathcal{L}_{Res}(\ell) = \sum_{\text{data}} \Big[\frac{1 - f_{G_2}}{\sigma_i \cdot \sigma_{\ell_1}^{\text{scale}}} G_1(\ell | \mu_\ell, \sigma_{\ell_1}^{\text{scale}} \cdot \sigma_i) + \frac{f_{G_2}}{\sigma_i \cdot \sigma_{\ell_2}^{\text{scale}}} G_2(\ell | \mu_\ell, \sigma_{\ell_2}^{\text{scale}} \cdot \sigma_i) \Big]. \quad (5.14)$$

This function represents a full expansion of a set of Gaussian (G) functions representing the vertex reconstruction uncertainty, σ_i, over every event (i) in the data sample. The mean lifetime, μ_ℓ, is fixed to zero, and σ^{scale} is a free parameter allowing for a scaling of the Gaussian contributions. A single Gaussian did not sufficiently model the distribution, so two Gaussians (G_1 and G_2) are used instead, with a relative normalization f_{G_2} term left as a free parameter to properly weight each Gaussian. The non-prompt portion is modeled with

$$\mathcal{L}_{NP}(\ell) = \mathcal{L}_{Res}(\ell' - \ell) \otimes e^{-\frac{\ell'}{\tau_{NP}}}, \quad (5.15)$$

where τ_{NP} is a free variable essentially denoting the average B-meson decay constant from the mixture present in the dataset.

In addition to the lifetime distribution of charmonia events, the dimuon con-

tinuum background is modeled:

$$\mathcal{L}_{BG}(\ell) = \mathcal{L}_{Res}(\ell' - \ell) \otimes \left[\frac{f_{BG_L}}{\tau_\ell^{BG_L}} \cdot e^{\frac{\ell'}{\tau_\ell^{BG_L}}} \cdot \Theta(-\ell') + \frac{f_{BG_R}}{\tau_\ell^{BG_R}} \cdot e^{-\frac{\ell'}{\tau_\ell^{BG_R}}} \cdot \Theta(\ell') + \frac{f_{BG_D}}{2\tau_\ell^{BG_D}} \cdot e^{-\frac{|\ell'|}{\tau_\ell^{BG_D}}} \right], \tag{5.16}$$

which convolutes three exponential functions, the single-sided right (R), modeling the non-prompt background contribution, the double sided (D) describing the background prompt component, and the single-sided left (L), which is included to model an exponential tail on the negative side of μ_ℓ. The slopes of these exponentials are described by the parameters $\tau_\ell^{BG_R}$, $\tau_\ell^{BG_D}$, and $\tau_\ell^{BG_L}$, respectively. The three f_{BG} parameters represent the relative normalization of each term's exponential, and the sum of which must equal unity. $\Theta(\ell')$ and $\Theta(-\ell')$ are step functions.

The final, composite model of each different region, the prompt, non-prompt, and background regions is

$$\mathcal{L}(\ell) = (1 - f_{NP}^{SR} - f_{BG}^{SR}) \cdot \mathcal{L}_{PR}(\ell) + f_{NP}^{SR} \cdot \mathcal{L}_{NP}(\ell) + f_{BG}^{SR} \cdot \mathcal{L}_{BG}(\ell), \tag{5.17}$$

with f_{BG}^{SR} and f_{NP}^{SR} the fraction of background and non-prompt events in the signal region.

With this model, the LSB, RSB, and SR are fitted simultaneously. Results of the fits from the SR from the extreme bins are shown in Figs. 5.25. Contributions from prompt, non-prompt, and background events are all identified. The SB fits, along with the individual contribution of each term, are shown in Fig. 5.26 for the same extreme bins as the SR.

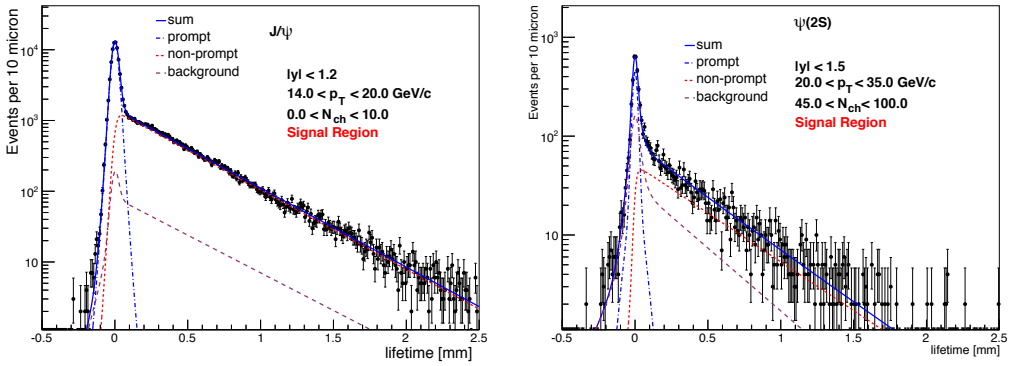

(a) (b)

Figure 5.25: The fitted ℓ distributions of the SR of the J/ψ $14 < p_{\mathrm{T}} < 20$ GeV/c and $0 < N_{\mathrm{ch}} < 10$ bin (a) and the $\psi(2S)$ $20 < p_{\mathrm{T}} < 35$ GeV/c and $40 < N_{\mathrm{ch}} < 100$ bin (b),The dashed blue line represents the prompt contribution to the signal, the dashed red line the non-prompt contribution, and the dashed purple is the continuum background contribution. The total contribution is shown in solid blue.

These fits are used to define two regions, separating prompt and non-prompt events, with the prompt region defined as $[n_{\sigma_\ell} \cdot \sigma_\ell,\ +n_{\sigma_\ell} \cdot \sigma_\ell]$ and the non-prompt as $[+n_{\sigma_\ell} \cdot \sigma_\ell, \infty]$, with $n_{\sigma_\ell} = 3$. This choice allows for a very clean prompt sample J/ψ, which at least 80 % of the prompt-SR attributed to actual signal, never more than 15 % non-prompt contribution, and a few percent background. The $\psi(2S)$ suffers from much more background, up to approximately 35 %, and approximately 10 % non-prompt contribution. Fig. 5.27 shown the prompt, non-prompt, and background fractions for the J/ψ (a) and $\psi(2S)$ (b) for the low-p_{T} bin, the trends in the high-p_{T} bin are similar.

5.5.3 $\psi(nS)$ Background Subtraction

These fits provide two separate distinctions: prompt and non-prompt events from the lifetime fit, and either signal or sideband events from the mass fit, from which we create six distinct regions: prompt signal region (PRSR), prompt left

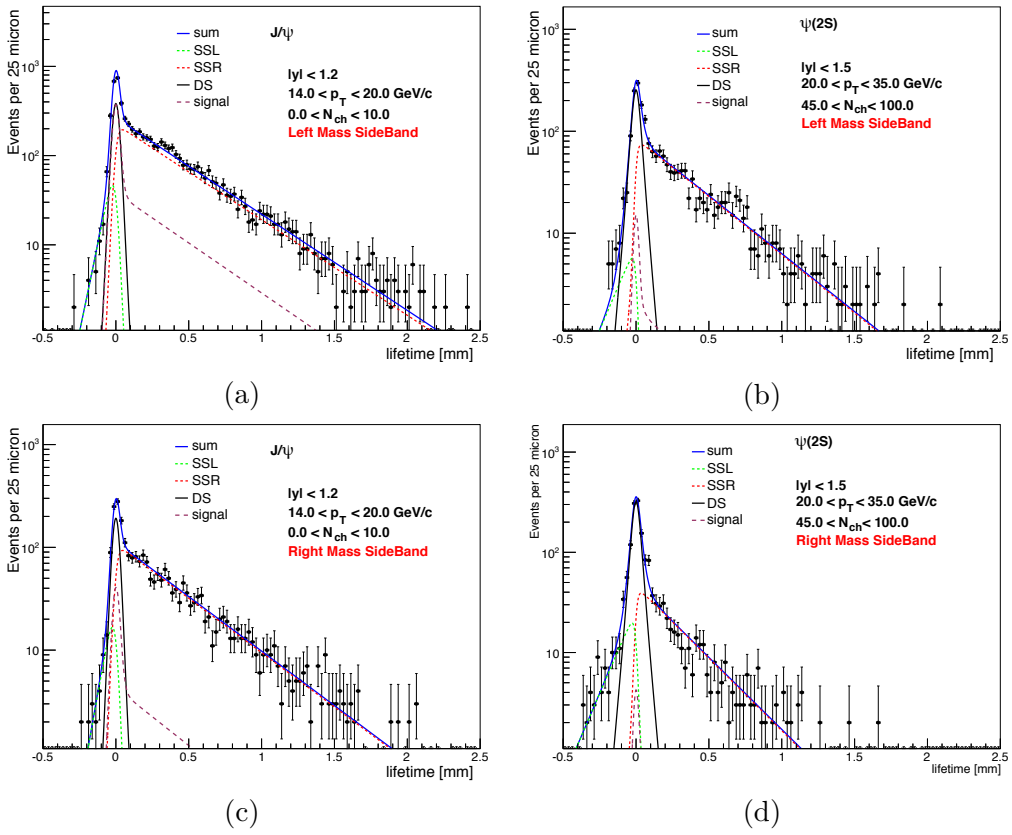

Figure 5.26: The fitted ℓ distributions of the J/ψ LSB (a) and RSB (c) for the $14 < p_{\mathrm{T}} < 20$ GeV/c and $0 < N_{\mathrm{ch}} < 10$ bin, and the $\psi(2S)$ LSB (b) and RSB (d) for the $20 < p_{\mathrm{T}} < 35$ GeV/c and $40 < N_{\mathrm{ch}} < 100$ bin. The single-sided left (SSL) is represented by a dashed green line, the single-sided right (SSR) by a dashed red line, the double-sided (DS) by a solid black line, and contribution from signal contamination by a purple dashed line. The sum of all the contributions is shown in solid blue.

sideband (PRLSB), prompt right sideband (PRRSB), non-prompt "signal" region (NPSR), non-prompt left sideband (NPLSB), and non-prompt right sideband (NPRSB). A visualization of these regions is shown in Fig. 5.28.

The five regions excluding the PRSR are used to develop a total background model, comprised of non-prompt events as well as events in the background mass continuum. In each region, background histograms of the 2D angular distributions and $(p_{\mathrm{T}}, |y|, M)$ 3D distributions are built. For the model of the background contin-

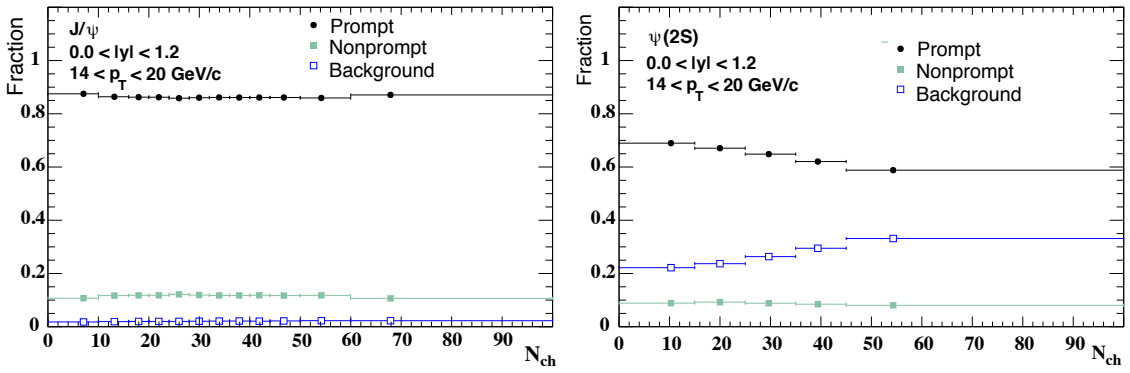

(a) (b)

Figure 5.27: The prompt (black), non-prompt (green), and background (blue) fractions of the J/ψ (a) and $\psi(2S)$ (b) against $N_{\rm ch}$, for the $14 < p_{\rm T} < 20$ GeV/c bin, in the prompt signal region.

uum, a linear combination of the PRLSB and PRRSB histograms is used, assuming that the background changes monotonically with dimuon mass.

The continuum background histogram for the PRSR is determined by

$$h_{BG}^{PRSR} = f_{LSB} \cdot \bar{h}^{PRLSB} + (1 - f_{LSB}) \cdot \bar{h}^{PRRSB}, \tag{5.18}$$

where $\bar{h}$ is the histogram of the identified region normalized to 1. The term f_{LSB}, which defines the weight of the left side band (LSB) continuum background in the signal region, is calculated as $f_{LSB} = (M_R - M_S)/(M_R - M_L)$, where M_X is the median dimuon mass of the RSB, LSB, or signal region.

To build the non-prompt background model, we must account for significant contamination from the continuum background in the NPSR, which must be subtracted before it can be used as the non-prompt background model. This process is similar to defining the background model histogram, differing only in using a linear combination of NPLSB and NPRSB (as opposed to PRLSB and PRRSB) to define

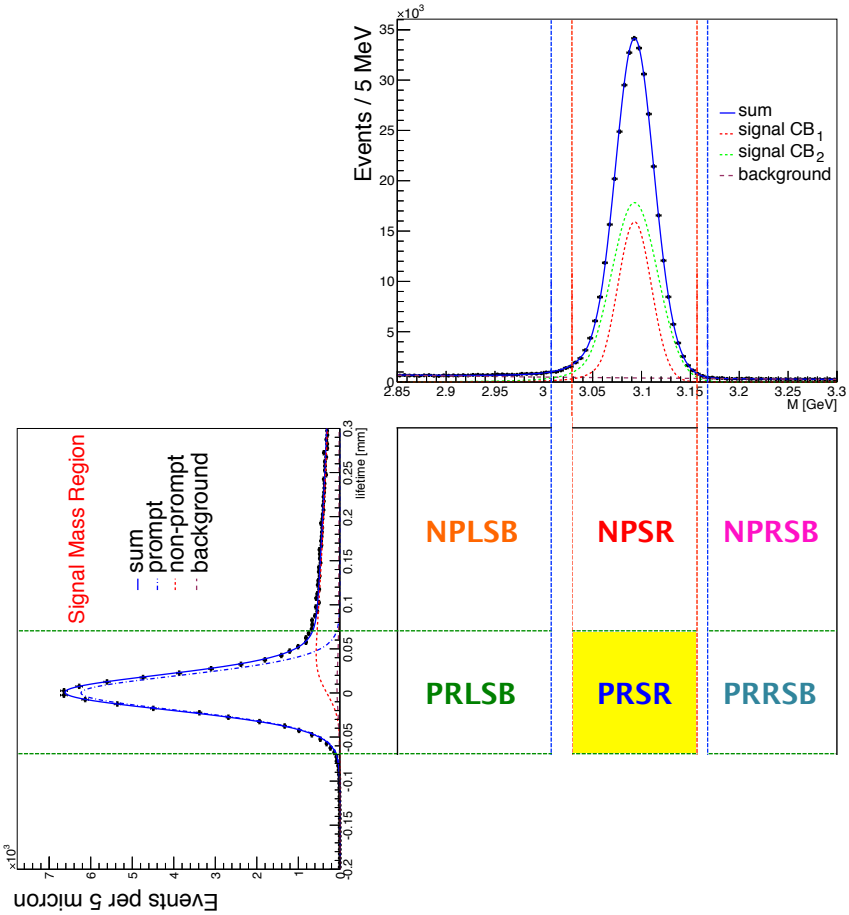

Figure 5.28: The regions defined by the mass and lifetime fits.

and subtract continuum events (Eq. 5.19). Once the continuum events have been subtracted from the NPSR, it can be used to determine the non-prompt background model (Eq. 5.20):

$$h_{BG}^{NPSR} = f_{LSB} \cdot \bar{h}^{NPLSB} + (1 - f_{LSB}) \cdot \bar{h}^{NPRSB}, \tag{5.19}$$

$$h_{NP}^{PRSR} = \bar{h}^{NPSR} - f_{BG}^{NPSR} \cdot \bar{h}_{BG}^{NPSR}, \tag{5.20}$$

where $\bar{h}$ is again the normalized histogram of the indicated region, h_{BG}^{NPSR} is the linear combination of the NPRSB and NPLSB (the mass continuum background

contamination), and f_{BG}^{NPSR} is the fraction of non-prompt events in the bin being analyzed.

The continuum background histogram and non-prompt histogram are then renormalized to one, weighted by the fraction of continuum background and non-prompt background, respectively, and combined to form the total background model.

$$h_{totBG}^{PRSR} = f_{BG}^{PRSR} \cdot \bar{h}_{BG}^{PRSR} + f_{NP}^{PRSR} \cdot \bar{h}_{NP}^{PRSR} \tag{5.21}$$

Once the background is subtracted, the $(\cos\vartheta, \phi)$ distribution of the remaining events is fed into the extraction framework described in Sec. 5.2.2.

5.5.4 Evaluation of the $\psi(nS)$ Systematic Uncertainties

The systematic uncertainties for the $\psi(nS)$ analysis are largely analogous to those already presented in Sec. 5.4.4, for the $\Upsilon(nS)$ analysis. Again, the uncertainties are grouped into N_{ch}-dependent and N_{ch}-independent global uncertainties. The N_{ch}-dependent uncertainties are due to the definition of the background model and from the polarization extraction framework. The global uncertainties contain all uncertainties related to muon efficiencies.

5.5.4.1 Background Model Uncertainty

Evaluation of the background model uncertainty is performed similarly to the $\Upsilon(nS)$ analysis described in Sec. 5.4.4.1, except in this case f_{LSB} is varied by $\pm 25\%$. Again this result is assumed to give a 100% closure limit result. Unlike the $\Upsilon(nS)$

analysis, the background model uncertainty for the $\psi(nS)$ states is very small, as a result of the sidebands being much closer to the $\psi(nS)$ mass poles.

5.5.4.2 Uncertainty of the Polarization Extraction Framework

Any potential bias associated with the extraction framework is established using similar methods to those described in Sec. 5.4.4.2. There are differences in the selection of the injected signal and background polarizations, which is selected as follows. To test how well the framework extracted the correct signal polarization, the injected signal is tested with the following four scenarios:

- $\lambda_{\vartheta}^{PX} = +1, \lambda_{\varphi}^{PX} = \lambda_{\vartheta\varphi}^{PX} = 0$
- $\lambda_{\vartheta}^{PX} = +0.5, \lambda_{\varphi}^{PX} = \lambda_{\vartheta\varphi}^{PX} = 0$
- $\lambda_{\vartheta}^{PX} = -0.5, \lambda_{\varphi}^{PX} = \lambda_{\vartheta\varphi}^{PX} = 0$
- $\lambda_{\vartheta}^{PX} = -1, \lambda_{\varphi}^{PX} = \lambda_{\vartheta\varphi}^{PX} = 0$

The mean of the absolute values of the four scenarios are quadratically added to obtain the systematic uncertainty.

To test the reliability of the background subtraction, unpolarized signal is generated with the following background polarization scenarios:

- J/ψ: $\lambda_{\vartheta}^{CS} = -0.25, \lambda_{\varphi}^{CS} = 0.15, \lambda_{\vartheta\varphi}^{CS} = 0$
- $\psi(2S)$: $\lambda_{\vartheta}^{CS} = -0.25, \lambda_{\varphi}^{CS} = 0.25, \lambda_{\vartheta\varphi}^{CS} = 0$

The three framework polarizations are represented, quadratically added together, in Figs. 5.29 and 5.30, labelled as "Frameworks."

5.5.4.3 Uncertainty Related to the Muon Efficiencies

All potential uncertainties related to the application of the efficiencies are treated as global uncertainties, calculated by taking the largest value from each potential source of bias, for each $\vec{\lambda}$ parameter, in each p_{T} range, and quadratically adding the values. The uncertainties related to the T&P model and the parametrization of the T&P efficiencies are established as described in Sec. 5.4.4.3. The uncertainty related to the ρ-factor, however, is calculated by applying the ρ-factor corrections while generating and reconstructing unpolarized events, and then extracting the polarization without applying the corrections. The divergence from $\vec{\lambda} = 0$ is assigned as the systematic uncertainty. The $\psi(nS)$ analysis also assigned a small uncertainty related to the applied dimuon vertex cut, which was negligible in the $\Upsilon(nS)$ analysis. The uncertainty remained small, though not negligible, and is calculated by applying a vertex efficiency correction while generating and reconstructing unpolarized events, then extracting the polarization without the efficiency. Again, the bias is the difference between the unpolarized injected $\vec{\lambda}$ and the measured $\vec{\lambda}$.

5.5.4.4 Uncertainty Related to the Lifetime Region Definition

The $\psi(nS)$ analysis had an additional uncertainty, induced by the definition of the lifetime regions when setting n_{σ}, which essentially introduces a kinematic cut on the data sample, creating a bias. In the N_{ch}-integrated analysis [87], for $n_{\sigma} = 3$, this bias is determined to be small, but becoming non-negligible as p_{T} increased.

The bias is covered by defining a systematic uncertainty, established using MC data, and assigning the bias as the difference between the extracted $\vec{\lambda}$ when using $n_\sigma = 3$, compared to no lifetime cut. In the p_{T} ranges considered, the resulting bias is negligible, and therefore is not included in the global uncertainty.

5.5.4.5 Summary of Systematic Uncertainties

All potential systematic uncertainties, including those determined to be N_{ch}-independent, for the frame dependent $\vec{\lambda}$ parameters are presented in Figs. 5.29 and 5.30. The individual biases are colored, with the framework uncertainties combined in blue, the background model in red, the parametrization of the muon efficiencies in light green, the T&P model in yellow, ρ-factor in purple, and the vertex correction in magenta. The biases have been stacked and are compared to the statistical uncertainty, in dark green, for each measured bin. For the J/ψ, the N_{ch}-dependent uncertainty of λ_ϑ in the HX frame is ~ 0.1, dominated by statistical uncertainties for all bins, and increasing slightly with N_{ch}. The uncertainties of λ_φ and $\lambda_{\vartheta\varphi}$ are approximately 0.02-0.03, again slightly increasing with N_{ch} and dominated by statistical uncertainties. The $\psi(2S)$ uncertainties are larger, ranging from $\sim 0.15 - 0.3$ for λ_ϑ, and from $\sim 0.02 - 0.08$ for λ_φ and $\lambda_{\vartheta\varphi}$, generally increasing with N_{ch}. The values of the N_{ch}-dependent systematic uncertainties in the PX frame were quadratically added and listed in the Appendix, in Tables A.5-A.6. The global uncertainties are given in Table A.7.

As in the case of the $\Upsilon(nS)$ analysis, a final closure test is performed to

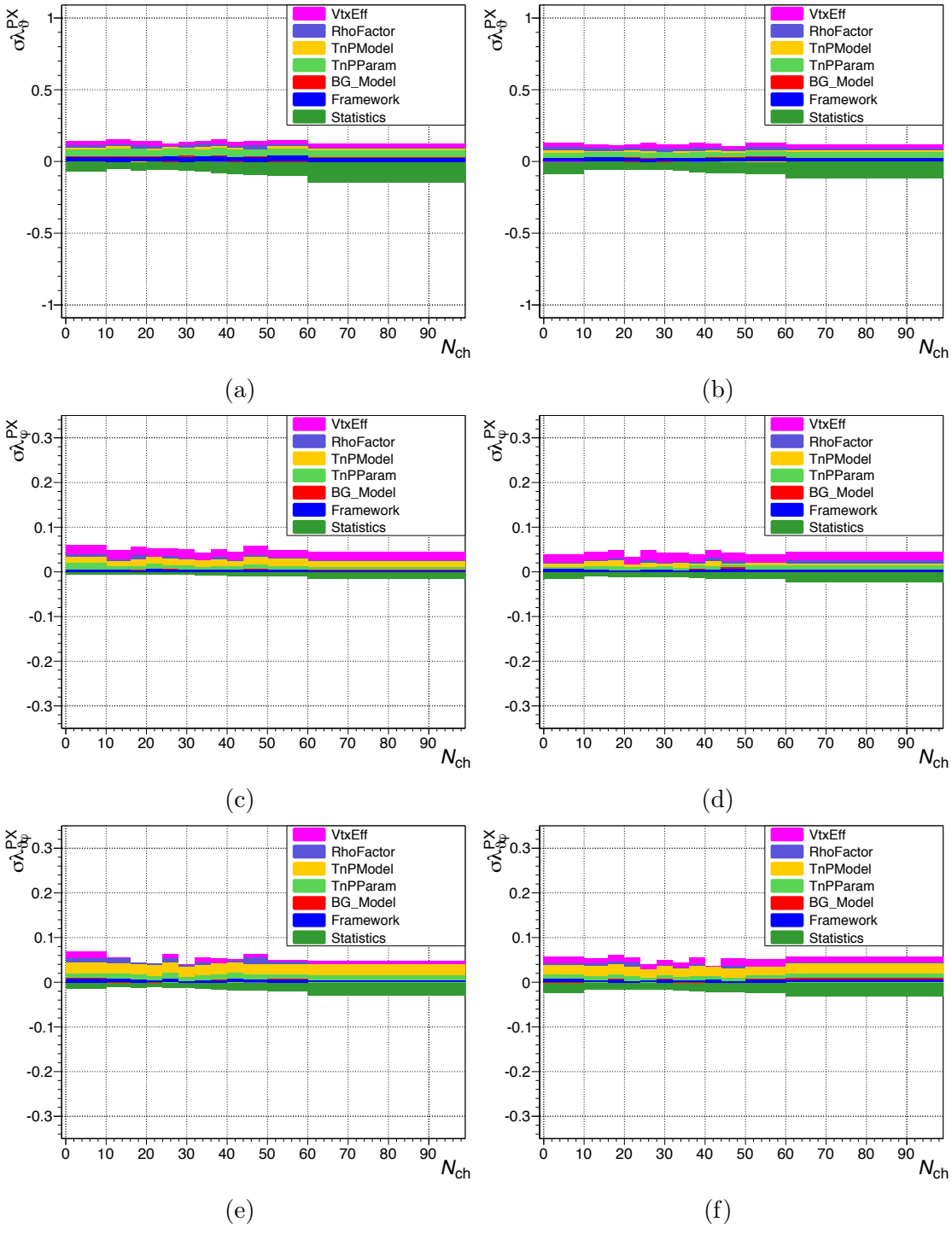

Figure 5.29: Systematic uncertainties, stacked on the positive side, affecting the J/ψ λ_ϑ^{PX} (a, b), λ_φ^{PX} (c, d), and $\lambda_{\vartheta\varphi}^{PX}$ (e, f) parameters, for $14 < p_{\mathrm{T}} < 20$ GeV/c (left column) and $20 < p_{\mathrm{T}} < 35$ GeV/c (right column), compared to the statistical uncertainties on the negative side.

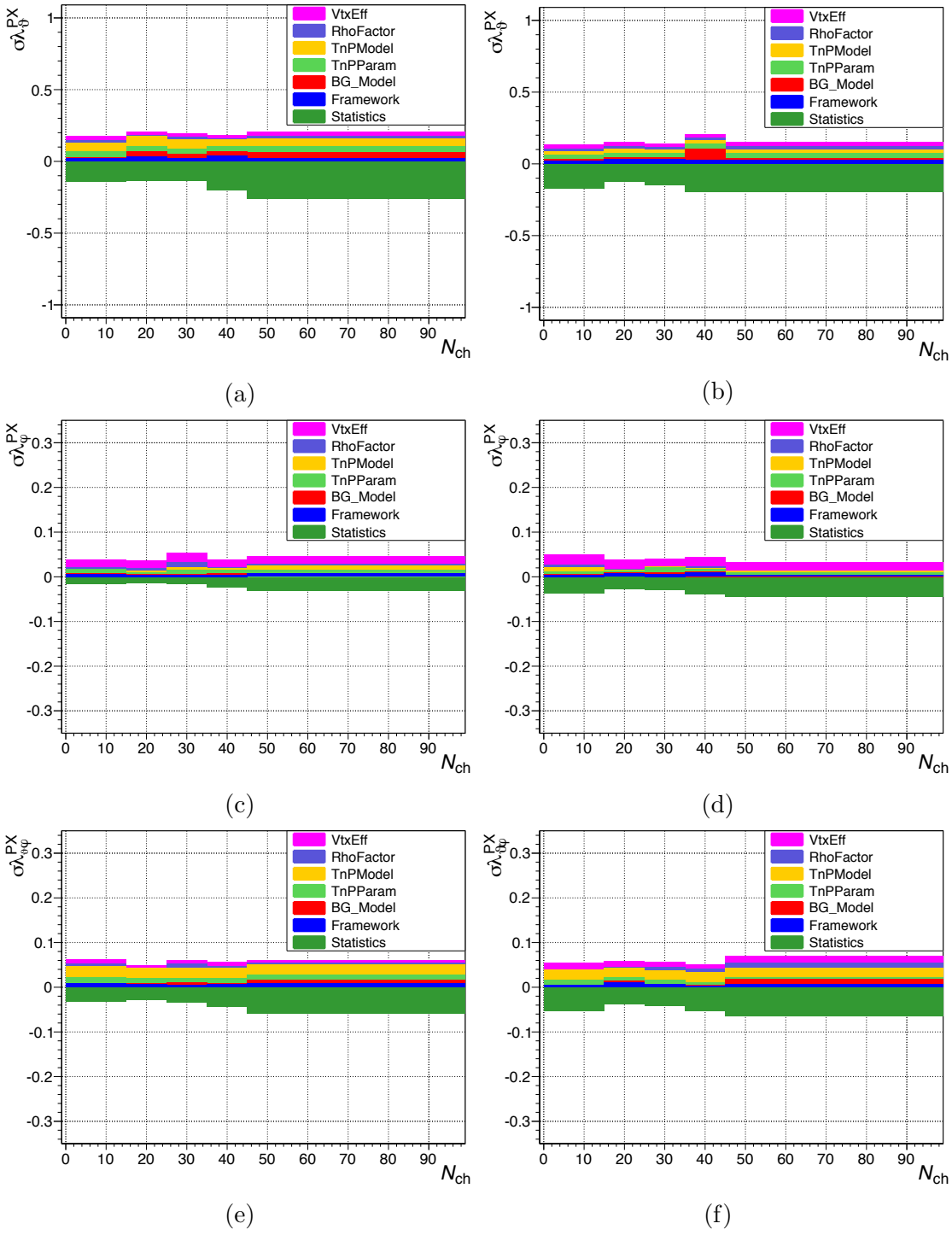

Figure 5.30: Same as Fig. 5.29, except for the $\psi(2S)$.

ensure that the systematic uncertainties are sufficiently under control by calculating the differences between the $\tilde{\lambda}$ measurements and comparing to the *total* systematic uncertainty, calculated by quadratically adding the global uncertainty to the N_{ch}-dependent uncertainties. This closure test is presented in Fig. 5.31 for the two $\psi(nS)$ states, showing the systematic uncertainties are well accounted for.

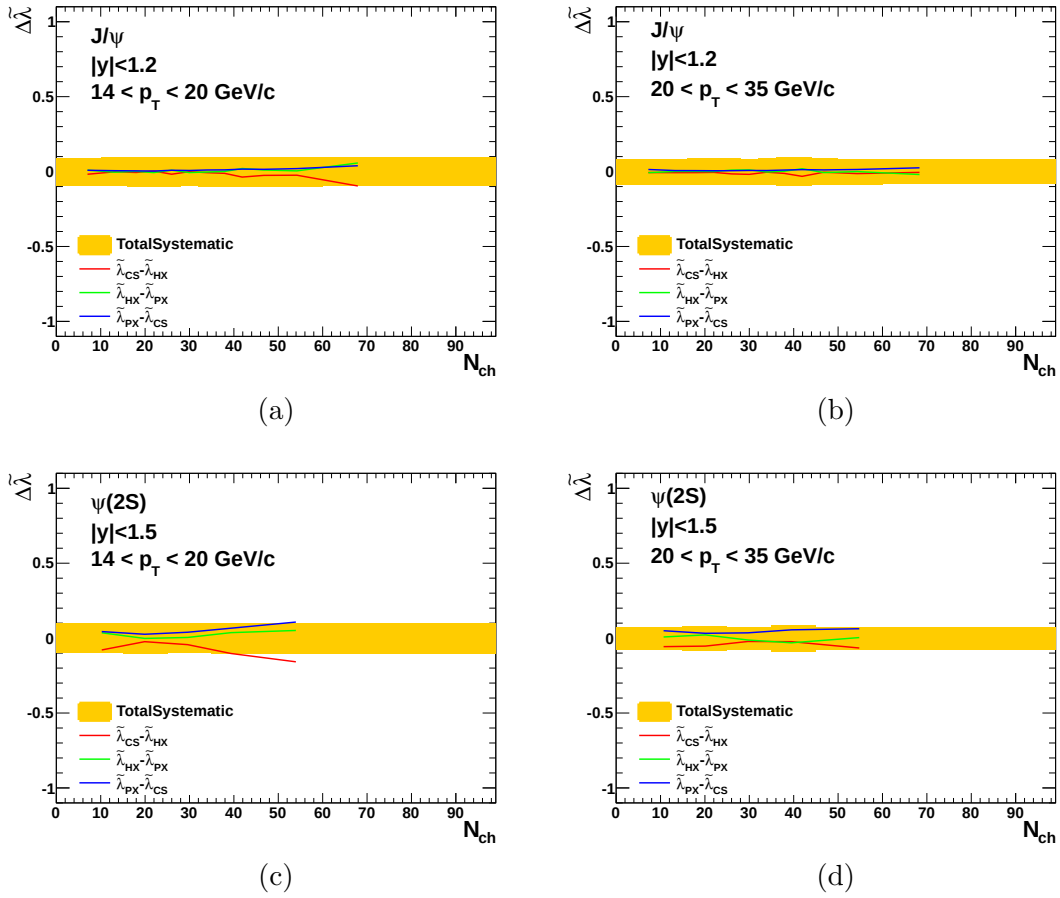

Figure 5.31: Comparison of the total systematic uncertainties to the difference between the $\tilde{\lambda}$ parameters from the different reference frames. The J/ψ is listed first in the p_{T} ranges $14 < p_{\mathrm{T}} < 20$ GeV/c (a) and $20 < p_{\mathrm{T}} < 35$ GeV/c (b), followed by the $\psi(2S)$ in the same ranges (c and d).

Chapter 6: Results and Discussion

6.1 Presentation of Polarization Results

The event multiplicity dependence of quarkonia polarization was studied by measuring the polarization parameters, $\vec{\lambda}$, against charged multiplicity, N_{ch}. The measurements were performed fully integrated over the available rapidity range, and partially integrated in p_{T}. The results from the $\Upsilon(nS)$ analysis were published in [89]; the $\psi(nS)$ analysis remains unpublished as of writing.

The final results of the $\Upsilon(nS)$ analysis are shown in Fig. 6.1 for the three $\Upsilon(nS)$ states. The polarizations are presented as measurements of λ_ϑ, λ_φ, $\lambda_{\vartheta\varphi}$, and $\tilde{\lambda}$, as measured in the HX frame, in the two p_{T} ranges. The $\tilde{\lambda}$ values have also been presented in the CS frame for comparison, showing values nearly identical to those from the HX. The values of the $\vec{\lambda}$ parameters are given in the Appendix, in Tables A.8-A.16, for the HX, CS, and PX reference frames.

The $\Upsilon(1S)$ polarization is precisely measured and is shown to be unvarying with N_{ch}. The near zero polarization is consistent with the previously published cpm-integrated values [64]. The $\Upsilon(2S)$ and $\Upsilon(3S)$ show slightly transverse polarizations, again consistent with the previous analysis, but the precision of the measurement is too low to make a conclusive statement about the multiplicity de-

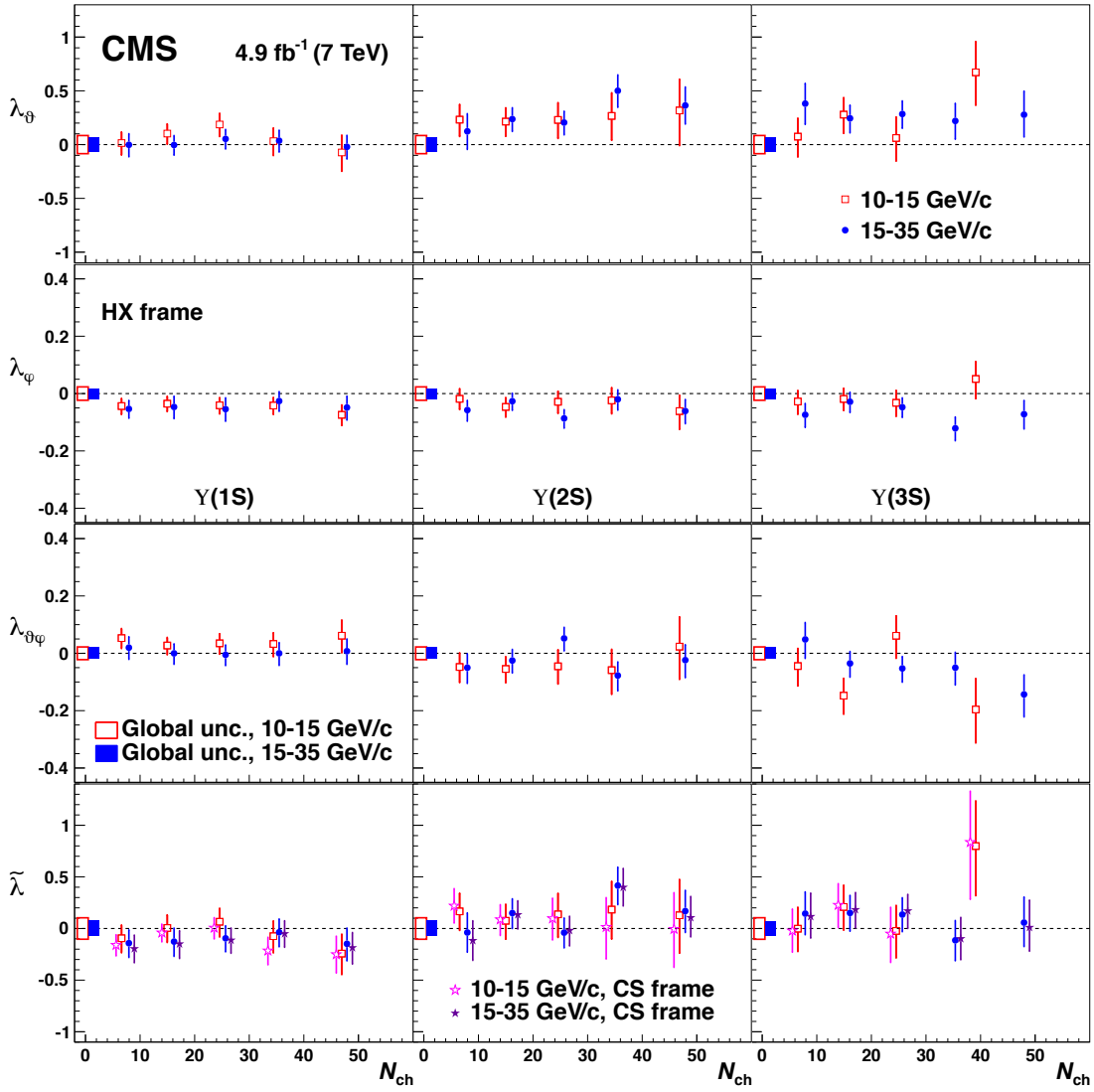

Figure 6.1: The final polarization measurements of the $\Upsilon(1S)$ (left column), $\Upsilon(2S)$ (middle), and $\Upsilon(3S)$ (right), in the p_{T} ranges $10 < p_{\mathrm{T}} < 15$ (red points) and $15 < p_{\mathrm{T}} < 35$ (blue points) GeV/c, against N_{ch}. The frame-dependent parameters λ_{ϑ} (top row), λ_{φ} (second row), $\lambda_{\vartheta\varphi}$ (third row), and the frame-independent $\tilde{\lambda}$ are presented in the HX frame. Additionally, measurements of $\tilde{\lambda}$ in the CS frame are shown, indicated with star symbols. The error bars represent the 68.3 % confidence limit, including statistical and systematic N_{ch}-dependent uncertainties. The global uncertainties are shown as the boxes near N_{ch}=0.

pendence. It should again be noted that all $\Upsilon(nS)$ states suffer from a significant amount of feed-down from the bottomonium P-wave χ_b states, and so a full interpretation of these results is difficult without analogous measurements of the χ_b polarization. Furthermore, the multiplicity range in this analysis is quite low, and collective behavior is not expected to occur in collisions of this nature. As more data is collected at CMS, an extension of these results to higher multiplicities in pp collisions, and especially into the heavy-ion collision system would be fruitful.

The multiplicity dependence of the $\psi(nS)$ polarizations is shown in Fig. 6.2. The polarizations are quantified by the $\vec{\lambda}$ parameters in the HX frame in two p_{T} ranges. The $\tilde{\lambda}$ values from the CS frame are also included, showing that the results are compatible across multiple frames. The $\vec{\lambda}$ values for the HX, PX, and CS frames are given in the Appendix, in Tables A.17-A.22.

The J/ψ was measured very precisely in twelve narrow N_{ch} bins, showing values the flucuate around unpolarized, consistent with the previous analysis [63]. The values do not show a dependence on N_{ch}. As in the case of the $\Upsilon(nS)$ states, the J/ψ suffers from a significant amount of feed-down from P-wave states. The $\psi(2S)$, with no feed-down from higher states, should be regarded as the most interesting quarkonium state for studies of quarkonium production. Unfortunately, the present dataset is too statistically limited to give precise results, and the multiplicity dependence remains inconclusive.

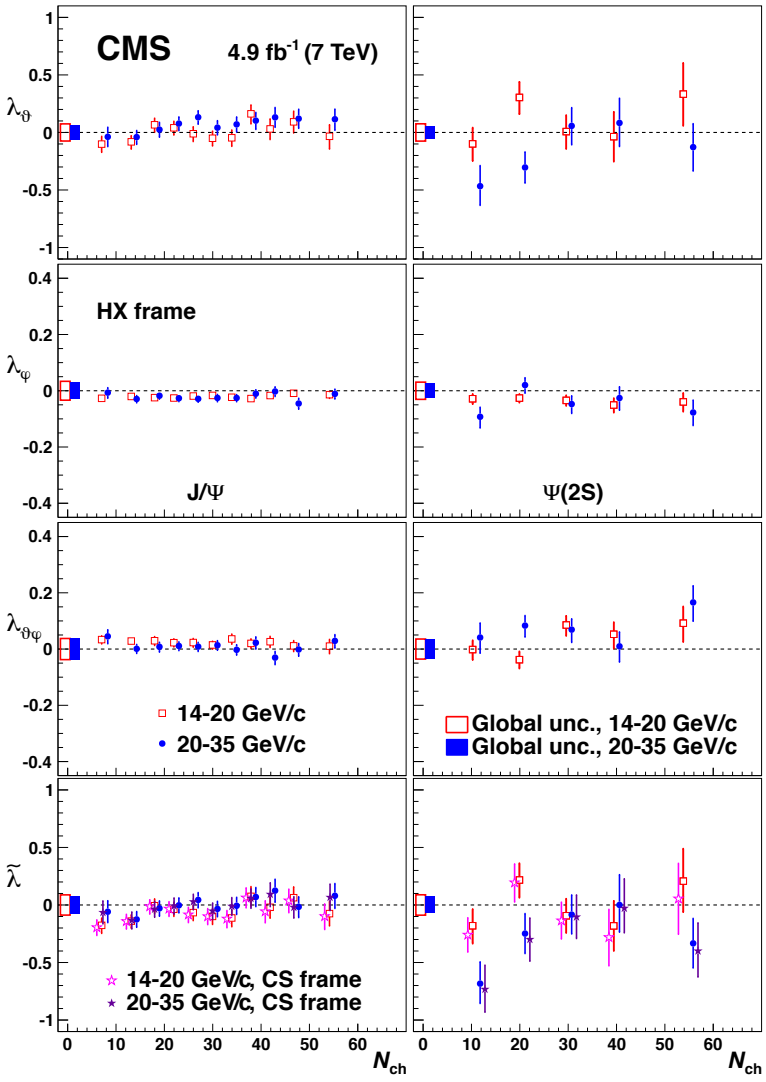

Figure 6.2: Same as Fig. 6.1, except for the J/ψ (left column) and $\Psi(2S)$ (right), in the indicated p_{T} ranges.

6.2 Interpretation of Polarization Results

The small measured polarizations for the five quarkonium states indicates that these quarkonia states are dominantly produced through the unpolarized ${}^1S_0^{[8]}$ pre-resonant octet state. The $\Upsilon(2S)$ and $\Upsilon(3S)$ measurements are slightly above zero, indicating a slight transverse polarization, compatible with a non-negligible amount of those states being produced via the transversely polarized ${}^3S_1^{[8]}$ octet. These results are consistent with the N_{ch}-integrated studies from [63] and [64]. The J/ψ and $\Upsilon(1S)$ terms are precisely measured, and with fine bins for the J/ψ. There is no trend seen as a function of N_{ch} in J/ψ or $\Upsilon(1S)$ polarizations, indicating that production between low- and high-multiplicity pp collisions is consistent. These states, however, suffer from a large amount of feed-down from their radial excitations and from χ states, muddling the interpretation of the results. More interesting are the excited states, especially the $\psi(2S)$, which, aside from the subtracted non-prompt contribution, is expected to completely be produced directly, with no feed-down. Unfortunately, the present uncertainties preclude a definitive statement regarding changes of their polarization with N_{ch}.

A potential change in polarization with N_{ch} has two potential sources, either from an actual change in production between low- and high-multiplicity, or as a result of a change in the amount of feed-down from P-wave states. These separate effects are contextualized in Fig. 6.3, which shows how the λ_ϑ parameter would change as a function of N_{ch} in various scenarios. The scenarios presented in the figure assume that there are two contributing production processes, each with a

distinct polarization, and that the proportion of the dominant process changes with N_{ch}, effectively changing the λ_ϑ value. The measured λ_ϑ of a dilepton distribution produced through two separate process is an average of the λ_ϑ value of the two processes, with the measured λ_ϑ dependent on the fraction of events, f, produced through each process [102]:

$$\lambda(f) = \Big[\frac{(1-f)\lambda_0}{3+\lambda_0} + \frac{f\lambda_1}{3+\lambda_1}\Big] \Big/ \Big[\frac{1-f}{3+\lambda_0} + \frac{f}{3+\lambda_1}\Big], \tag{6.1}$$

where λ_0 and λ_1 are set to the polarizations of the distinct processes.

In Fig. 6.3a, production of the quarkonium is assumed to be directly produced and dominated by two pre-resonant states, the unpolarized ${}^1S_0^{[8]}$ octet, corresponding to $\lambda_\vartheta = 0$ and the transversely polarized ${}^3S_1^{[8]}$ octet, with $\lambda_\vartheta = +1$. Using the solid green line as an example, this scenario assumes that at $N_{\mathrm{ch}} = 0$, the ${}^1S_0^{[8]}$ octet is completely dominant, producing all the bound quarkonia. As N_{ch} increases, the ${}^3S_1^{[8]}$ becomes dominant, until at $N_{\mathrm{ch}} = 60$, it is the only pre-resonant octet state contributing to quarkonia production. It should be noted that this is an extreme example, and that any actual effect should be expected to be much more subtle, more like those represented by the dashed lines. The most interesting study will be to compare the results presented in this thesis to measurements in heavy-ion collisions, which produce thousands of particles per collision, as opposed to the dozens created in pp collisions. The $\Upsilon(3S)$ results are shown overlaying the potential scenarios.

The second source of change in polarization stems from differences in polarization between the S-wave and P-wave states, and the fraction of feed-down changing

along with $N_{\rm ch}$. Currently, the measured polarizations are for *inclusive* $\Upsilon(nS)$ and $\psi(nS)$ samples, and the polarizations of the P-wave states have not yet been measured, though are predicted to be restricted to $\lambda_\vartheta > -1/3$ and $\lambda_\vartheta > -3/5$, for the $\chi_{c(b)1}$ and $\chi_{c(b)2}$, respectively [103]. This means that feed-down from P-wave states can significantly alter the measured polarization of the S-wave state, assuming that the polarization of the two is not identical. This effect will be especially significant for the $\Upsilon(1S)$ and the J/ψ. However, the only state *not* affected by feed-down is the $\psi(2S)$. In Fig. 6.3b, various scenarios showing different polarizations for the S- and P-wave states have been calculated. The lines always indicate a change from 50% P-wave contribution to 0%, over the range of the measured $N_{\rm ch}$. As an example, the dotted blue line is assigned a directly produced component $\lambda_0 = 0$ and a feed-down component $\lambda_1 = +1$. At $N_{\rm ch} = 0$, the processes producing each polarization are equally weighted, so the measured polarization would be $\lambda_\vartheta = +0.5$. As $N_{\rm ch}$ increases, the feed-down contribution is decreasing, trending towards $\lambda_\vartheta = 0$ at $N_{\rm ch} = 60$. The various scenarios are shown against the $\Upsilon(1S)$ results.

6.3 Future Analyses

The most precisely measured states, the J/ψ and the $\Upsilon(1S)$, are unfortunately the most complicated, due to feed-down from excited states, and the excited S-wave states suffer from large uncertainties. Thus, the polarization measurements against $N_{\rm ch}$ are far from definitive. The simplest method for reducing many of the uncertainties is simply to use newer datasets, which contain a tremendous improvement

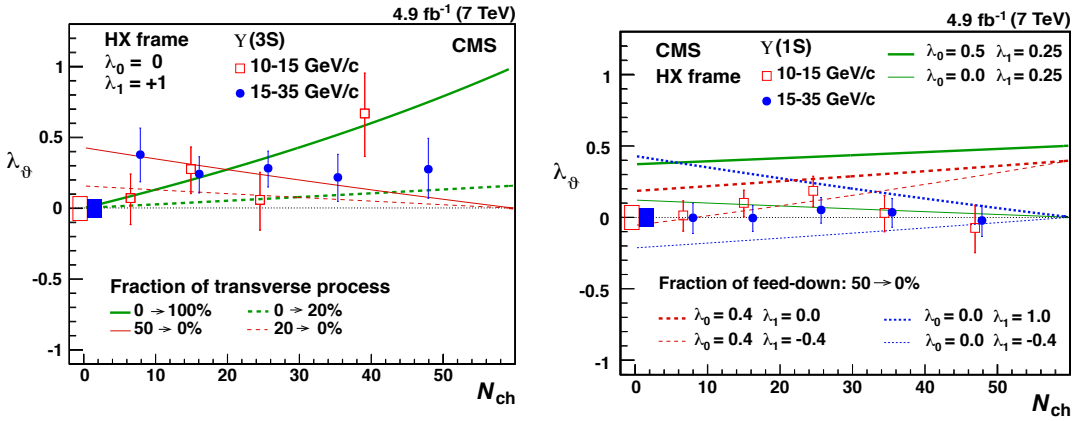

(a) (b)

Figure 6.3: Various scenarios are presented for the effect of varying the dominant pre-resonant state in (a), with each line representing a different initial and final percentage of the transverse process, compared to the $\Upsilon(3S)$ results. In (b), each line represents a potential feed-down effect, with differing S- and P-wave polarizations, compared to the $\Upsilon(1S)$ results.

in the statistics available for analysis, and would allow for more precise results, extending up to higher multiplicities. An increase in statistics, however, would not account for the complications of P-wave feed-down, and so a measurement of the χ_c and χ_b polarizations must be performed. This measurement is quite difficult, as it requires the reconstruction of low-energy photons. Furthermore, the feed-down fractions must be measured more precisely, especially in the case of the bottomonia, with its complicated feed-down structure.

Longer term, this line of study should be extended to the pPb and PbPb collision systems. With the unique tracking and resolution capabilities of the CMS detector, the higher luminosities from upcoming heavy-ion runs, a measurement of polarization would provide valuable information to understand the hadronization process of mesons in a colored medium, providing a stringent test of the NRQCD universality theorem. Further, as outlined in [104], it is possible to use dilepton event

samples to measure the polarization of vector quarkonia as an instrument to probe χ_c and χ_b suppression in heavy-ion collisions, where the overwhelming background from π^0 decays prevents direct determination of the P-wave signal yields. A term, $R(P)$, describes the feed-down fraction of P-wave to S-wave, which can be calculated using polarization measurements:

$$R(P) = \frac{(3 + \lambda_\vartheta^P)(\lambda_\vartheta^{2S} - \lambda_\vartheta^{1S})}{(3 + \lambda_\vartheta^{1S})(\lambda_\vartheta^{2S} - \lambda_\vartheta^P)}. \tag{6.2}$$

The fraction of feed-down, assuming simplistic quarkonium melting models, should decrease tremendously at a high enough centrality for the χ state to dissociate, but low enough that the S-wave state would remain intact. This behavior would produce the trend with N_{part} (or any other centrality variable) in Fig. 6.4a, which shows a hypothetical calculation of $R(\chi_c)^{PbPb}/R(\chi_c)^{pp}$, which can be thought of as analogous to an R_{AA} measurement. The suppression of the χ_c states would be observed through a change in the J/ψ polarization, such as that shown in Fig. 6.4b, which shows a change from a small longitudinal polarization to a strong longitudinal polarization. This indicates that in this *hypothetical* scenario, the more transverse χ states dissociated so that only the longitudinal, directly produced J/ψ states are left. To perform this analysis, the polarization of excited S-wave and P-wave states must be determined in *pp* collisions, and the inclusive prompt-1S polarization is measured in PbPb collisions as a function of N_{part}. In ultra-peripheral nuclear collisions when $N_{part} = 2$, the collision is expected to mimic a *pp* event, so $R(P)^{PbPb}$ should equal $R(P)^{pp}$ and the ratio of the former to the latter would be unity. As

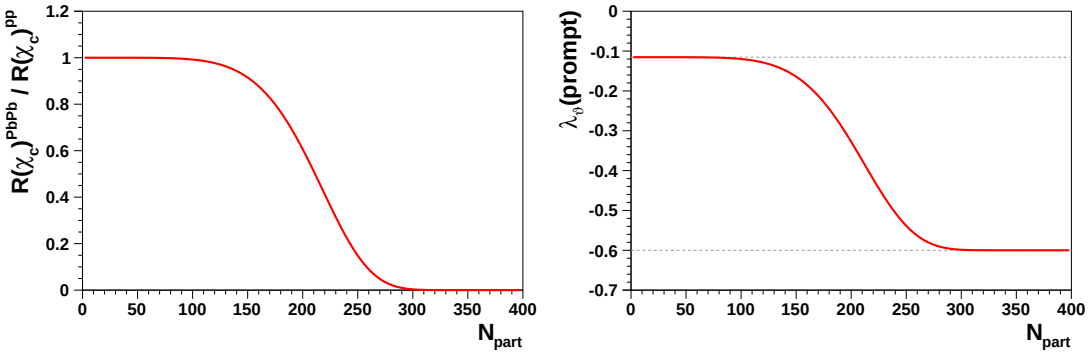

(a) (b)

Figure 6.4: A hypothetical scenario depicting the dissociation of χ_c states in heavy-ion collisions through a calculation of $R(\chi_c)^{PbPb}/R(\chi_c)^{pp}$ versus N_{part} (a), and the observable change in λ_ϑ (b) used to measure the suppression. Figures taken from [104].

N_{part} increases and a hot nuclear medium forms, this ratio is expected to dip below unity, indicating χ suppression. When N_{part} is low, the anisotropy parameter would represent an average of the polarizations of the S and P-wave particles, but as N_{part} increases and P-wave particles are suppressed, the anisotropy parameter would trend to the value of a directly produced quarkonium. This average anisotropy parameter is used in Eq. 6.2, along with the S- and P-wave polarization parameters measured in pp collisions, to calculate $R(P)$ as a function of N_{part}. This value indicates how much χ suppression is present in nuclear collisions, which would greatly enhance the interpretation of quarkonia suppression results, and advance theoretical arguments.

Finally, a confirmation of polarization can also help mitigate detector-level uncertainties in certain measurements. For example, in quarkonia yield studies such as [57], [105], and many others, Monte Carlo tests used to establish detector efficiencies generally assume unpolarized quarkonia production. While the measured small polarizations (at least in low multiplicity pp collisions) suggest this assump-

tion should not greatly affect yield results, measurements of J/ψ particles created in ultra-peripheral collisions are potentially greatly influenced by assumptions about polarizations. In the case of coherent production, the quarkonia are expected to inherit the polarization of the incoming photon and to therefore be transversely polarized, though this assumption has never been tested. In non-coherent production, the quarkonia are produced alongside other particles, and it is possible that the polarization of the photon would not fully transfer to the quarkonium. Non-coherent measurements are key to understanding the initial state gluon distribution in nuclear collisions, and without knowledge of the quarkonia polarization, these measurements would be ambiguous.

Chapter 7: Summary

"The truth is rarely pure and never simple."

~Oscar Wilde

When the LHC came online in 2010, a new era of ultra-relativistic heavy-ion physics began. The LHC could deliver, and CMS could record, record luminosities at an order of magnitude higher energy than previously achieved. After the possibility of an asymptotically free state of matter called the quark-gluon plasma (QGP) was proposed in 1973, most of the ensuing years have been spent proving its existence. In this new era, the question of existence has been answered affirmatively, and a period of precision physics has begun.

Of the potential tools used to study the QGP, this thesis described the role of quarkonia mesons, which are produced in abundance at the LHC. The suppression of quarkonia particles in heavy-ion collisions, relative to scaled *pp* yields, is one of the signature indications of the presence of a QGP. Indeed, experiments at RHIC and the LHC (discussed in Ch. 3) have seen strong evidence of sequential suppression of the various quarkonium states. Yet, these measurements are complicated by complex feed-down chains, as well as by potential regeneration as the QGP expands, cools, and reforms into hadrons. In fact, even the basic production mechanism of quarkonia

is still not fully understood, adding to the intricacies of all possible interpretations of the measurements.

The analyses presented in this thesis, and the future work stemming from it, strives to disentangle the complexities of quarkonia suppression in heavy-ion collisions. The polarization of five quarkonium states was measured against the particle multiplicity of events produced in pp collisions, at a center-of-mass energy of $\sqrt{s} = 7$ TeV, with the CMS detector at the LHC. In the first part of the analysis (Sec. 5.4), and in the first study of its kind, the polarizations of the $\Upsilon(1S)$, $\Upsilon(2S)$, and $\Upsilon(3S)$ were measured against charged particle multiplicity (N_{ch}), integrated in rapidity, $|y| < 1.2$, and in two p_{T} ranges, $10 < p_{\mathrm{T}} < 15$ and $15 < p_{\mathrm{T}} < 35$ GeV/c. The second part of the analysis was dedicated to an analogous study of the $\psi(nS)$ mesons, which are more difficult to study because a significant amount of their yield comes from the decay of long-lived B-mesons. The $\psi(nS)$ states were also measured in two p_{T} ranges, $14 < p_{\mathrm{T}} < 20$ and $20 < p_{\mathrm{T}} < 35$ GeV/c, integrated in rapidity to $|y| < 1.2$ for the J/ψ and $|y| < 1.5$ for the $\psi(2S)$.

The results show that the $\Upsilon(1S)$ polarization does not vary with N_{ch}, and the uncertainties on the $\Upsilon(2S)$ and $\Upsilon(3S)$ measurements preclude making a definitive statement about their trends. These results have been published in Physics Letters B [89] and the main result is shown in Fig. 6.1. The polarizations of the $\psi(nS)$ states are shown in Fig. 6.2, and are yet to be published. The J/ψ polarization is measured to be unvarying with N_{ch}, and the uncertainties on the $\psi(2S)$ make a definitive statement impossible.

The work in this thesis should be taken as the first step into a broad analysis

of the effect of a colored medium on the production of quarkonia mesons, and so the impact of the study stems more from opening new avenues worthy of attention than from providing definitive physics answers. The analysis would significantly benefit from the increased statistics from datasets that have already been collected, immediately driving down the largest source of uncertainty in the measurements. Eventually, the use of polarization measurements against N_{ch} will be able to more persuasively answer the of NRQCD universality, but for now, the measured multiplicity ranges, which number only in the dozens, do not provide nearly the strength of a test of a polarization measurement in heavy-ion collisions, where multiplicities number in the thousands. Once polarization measurements are established in heavy-ion datasets, a measurement of the χ suppression can be attempted. While this final step will likely not be possible until the high-luminosity PbPb runs planned for Run III of the LHC, a successful measurement would truly be a precision result.

Appendix A: Data Tables

Table A.1: N_{ch}-dependent systematic uncertainties for $\Upsilon(1S)$ state in the PX frame.

$\Upsilon(1S)$, PX Frame				
N_{ch}	$\sigma^{syst}(\lambda_\vartheta)$	$\sigma^{syst}(\lambda_\varphi)$	$\sigma^{syst}(\lambda_{\vartheta\varphi})$	$\sigma^{syst}(\tilde{\lambda})$
$10 < p_{\mathrm{T}} < 15$ GeV/c				
$0-10$	0.016	0.018	0.011	0.040
$10-20$	0.022	0.025	0.013	0.045
$20-30$	0.022	0.025	0.011	0.055
$30-40$	0.023	0.034	0.009	0.068
$40-60$	0.035	0.049	0.015	0.101
$15 < p_{\mathrm{T}} < 35$ GeV/c				
$0-10$	0.024	0.033	0.010	0.086
$10-20$	0.039	0.042	0.025	0.118
$20-30$	0.042	0.035	0.025	0.104
$30-40$	0.035	0.032	0.025	0.090
$40-60$	0.031	0.040	0.025	0.114

Table A.2: N_{ch}-dependent systematic uncertainties for $\Upsilon(2S)$ state in the PX frame.

$\Upsilon(2S)$, PX Frame				
N_{ch}	$\sigma^{syst}(\lambda_\vartheta)$	$\sigma^{syst}(\lambda_\varphi)$	$\sigma^{syst}(\lambda_{\vartheta\varphi})$	$\sigma^{syst}(\tilde{\lambda})$
$10 < p_{\mathrm{T}} < 15$ GeV/c				
$0-10$	0.014	0.023	0.015	0.067
$10-20$	0.024	0.036	0.013	0.094
$20-30$	0.032	0.055	0.012	0.137
$30-40$	0.064	0.091	0.020	0.217
$40-60$	0.046	0.093	0.015	0.240
$15 < p_{\mathrm{T}} < 35$ GeV/c				
$0-10$	0.035	0.041	0.015	0.105
$10-20$	0.024	0.036	0.010	0.082
$20-30$	0.031	0.035	0.009	0.099
$30-40$	0.028	0.031	0.010	0.081
$40-60$	0.030	0.037	0.012	0.079

Table A.3: N_{ch}-dependent systematic uncertainties for $\Upsilon(3S)$ state in the PX frame.

$\Upsilon(3S)$, PX Frame				
N_{ch}	$\sigma^{syst}(\lambda_\vartheta)$	$\sigma^{syst}(\lambda_\varphi)$	$\sigma^{syst}(\lambda_{\vartheta\varphi})$	$\sigma^{syst}(\tilde{\lambda})$
$10 < p_{\mathrm{T}} < 15$ GeV/c				
$0-10$	0.013	0.035	0.011	0.085
$10-20$	0.034	0.052	0.013	0.146
$20-30$	0.053	0.087	0.012	0.189
$30-60$	0.055	0.102	0.013	0.426
$15 < p_{\mathrm{T}} < 35$ GeV/c				
$0-10$	0.028	0.034	0.009	0.091
$10-20$	0.031	0.042	0.012	0.112
$20-30$	0.028	0.037	0.009	0.096
$30-40$	0.026	0.041	0.010	0.109
$40-60$	0.039	0.048	0.013	0.107

Table A.4: Global uncertainties for each $\Upsilon(nS)$ state in the PX frame

p_{T} (GeV/c)	λ_ϑ	λ_φ	$\lambda_{\vartheta\varphi}$	$\tilde{\lambda}$
$\Upsilon(1S)$				
$10-15$	0.014	0.043	0.025	0.112
$15-35$	0.048	0.028	0.020	0.076
$\Upsilon(2S)$				
$10-15$	0.068	0.044	0.025	0.112
$15-35$	0.062	0.028	0.020	0.076
$\Upsilon(3S)$				
$10-15$	0.068	0.044	0.025	0.113
$15-35$	0.064	0.028	0.020	0.076

Table A.5: N_{ch}-dependent systematic uncertainties for J/ψ state in the PX frame.

J/ψ, PX Frame				
N_{ch}	$\sigma^{syst}(\lambda_\vartheta)$	$\sigma^{syst}(\lambda_\varphi)$	$\sigma^{syst}(\lambda_{\vartheta\varphi})$	$\sigma^{syst}(\tilde{\lambda})$
$14 < p_{\mathrm{T}} < 20$ GeV/c				
$0-10$	0.034	0.032	0.014	0.060
$10-16$	0.040	0.041	0.011	0.068
$16-20$	0.039	0.038	0.006	0.059
$20-24$	0.034	0.037	0.007	0.065
$24-28$	0.036	0.037	0.012	0.067
$28-32$	0.040	0.040	0.007	0.069
$32-36$	0.042	0.043	0.006	0.068
$36-40$	0.041	0.043	0.009	0.066
$40-44$	0.036	0.038	0.014	0.067
$44-50$	0.042	0.045	0.013	0.067
$50-60$	0.043	0.041	0.008	0.076
$60-100$	0.038	0.036	0.008	0.085
$20 < p_{\mathrm{T}} < 35$ GeV/c				
$0-10$	0.027	0.027	0.010	0.041
$10-16$	0.030	0.028	0.004	0.053
$16-20$	0.031	0.032	0.010	0.043
$20-24$	0.028	0.027	0.006	0.049
$24-28$	0.029	0.028	0.004	0.041
$28-32$	0.029	0.026	0.007	0.045
$32-36$	0.025	0.029	0.007	0.047
$36-40$	0.026	0.026	0.006	0.044
$40-44$	0.025	0.027	0.009	0.040
$44-50$	0.028	0.028	0.008	0.044
$50-60$	0.033	0.032	0.011	0.070
$60-100$	0.028	0.031	0.013	0.075

Table A.6: N_{ch}-dependent systematic uncertainties for $\psi(2S)$ state in the PX frame.

$\psi(2S)$, PX Frame				
N_{ch}	$\sigma^{syst}(\lambda_\vartheta)$	$\sigma^{syst}(\lambda_\varphi)$	$\sigma^{syst}(\lambda_{\vartheta\varphi})$	$\sigma^{syst}(\tilde{\lambda})$
$14 < p_{\mathrm{T}} < 20$ GeV/c				
$0-15$	0.042	0.042	0.014	0.062
$15-25$	0.045	0.048	0.012	0.102
$25-35$	0.042	0.046	0.012	0.083
$35-45$	0.072	0.071	0.015	0.147
$45-100$	0.059	0.072	0.016	0.169
$20 < p_{\mathrm{T}} < 35$ GeV/c				
$0-15$	0.029	0.038	0.012	0.111
$15-25$	0.043	0.050	0.022	0.125
$25-35$	0.055	0.050	0.010	0.091
$35-45$	0.053	0.047	0.008	0.077
$45-100$	0.035	0.036	0.017	0.092

Table A.7: Global uncertainties for each $\psi(nS)$ state in the PX frame

p_{T} (GeV/c)	λ_ϑ	λ_φ	$\lambda_{\vartheta\varphi}$	$\tilde{\lambda}$
J/ψ				
$14-20$	0.074	0.032	0.035	0.092
$20-35$	0.064	0.029	0.032	0.082
$\psi(2S)$				
$14-20$	0.088	0.027	0.030	0.096
$20-35$	0.059	0.027	0.032	0.072

Table A.8: Measured $\Upsilon(1S)$ polarization parameters, in the HX frame. The errors represent the total statistical plus $N_{\rm ch}$-dependent systematic uncertainties.

$\Upsilon(1S)$, HX Frame				
$N_{\rm ch}$	λ_ϑ	λ_φ	$\lambda_{\vartheta\varphi}$	$\tilde{\lambda}$
$10-15$ GeV/c				
$0-10$	$0.015^{+0.126}_{-0.141}$	$-0.044^{+0.034}_{-0.038}$	$0.053^{+0.040}_{-0.042}$	$-0.094^{+0.158}_{-0.173}$
$10-20$	$0.103^{+0.121}_{-0.134}$	$-0.035^{+0.032}_{-0.036}$	$0.027^{+0.034}_{-0.040}$	$0.005^{+0.158}_{-0.170}$
$20-30$	$0.187^{+0.131}_{-0.143}$	$-0.041^{+0.035}_{-0.037}$	$0.035^{+0.039}_{-0.043}$	$0.065^{+0.166}_{-0.182}$
$30-40$	$0.033^{+0.148}_{-0.161}$	$-0.042^{+0.036}_{-0.040}$	$0.033^{+0.046}_{-0.051}$	$-0.073^{+0.176}_{-0.195}$
$40-60$	$-0.073^{+0.176}_{-0.197}$	$-0.074^{+0.040}_{-0.044}$	$0.061^{+0.057}_{-0.064}$	$-0.242^{+0.206}_{-0.226}$
$15-35$ GeV/c				
$0-10$	$-0.001^{+0.124}_{-0.129}$	$-0.053^{+0.035}_{-0.039}$	$0.020^{+0.041}_{-0.046}$	$-0.141^{+0.144}_{-0.157}$
$10-20$	$-0.004^{+0.106}_{-0.116}$	$-0.047^{+0.041}_{-0.044}$	$-0.000^{+0.038}_{-0.042}$	$-0.127^{+0.147}_{-0.165}$
$20-30$	$0.053^{+0.101}_{-0.114}$	$-0.054^{+0.043}_{-0.046}$	$-0.005^{+0.039}_{-0.042}$	$-0.095^{+0.139}_{-0.148}$
$30-40$	$0.037^{+0.111}_{-0.122}$	$-0.026^{+0.037}_{-0.041}$	$-0.000^{+0.040}_{-0.046}$	$-0.036^{+0.145}_{-0.161}$
$40-60$	$-0.020^{+0.119}_{-0.133}$	$-0.049^{+0.042}_{-0.048}$	$0.007^{+0.045}_{-0.051}$	$-0.148^{+0.161}_{-0.179}$

Table A.9: Measured $\Upsilon(1S)$ polarization parameters, in the PX frame. The errors represent the total statistical plus $N_{\rm ch}$-dependent systematic uncertainties.

$\Upsilon(1S)$, PX Frame				
$N_{\rm ch}$	λ_ϑ	λ_φ	$\lambda_{\vartheta\varphi}$	$\tilde{\lambda}$
$10-15$ GeV/c				
$0-10$	$0.013^{+0.076}_{-0.083}$	$-0.063^{+0.061}_{-0.072}$	$-0.038^{+0.036}_{-0.040}$	$-0.159^{+0.142}_{-0.160}$
$10-20$	$-0.025^{+0.072}_{-0.081}$	$-0.005^{+0.056}_{-0.066}$	$-0.051^{+0.032}_{-0.036}$	$-0.040^{+0.135}_{-0.145}$
$20-30$	$-0.041^{+0.073}_{-0.081}$	$0.018^{+0.059}_{-0.065}$	$-0.087^{+0.032}_{-0.037}$	$0.007^{+0.142}_{-0.155}$
$30-40$	$0.029^{+0.083}_{-0.089}$	$-0.091^{+0.079}_{-0.088}$	$-0.028^{+0.040}_{-0.044}$	$-0.213^{+0.168}_{-0.176}$
$40-60$	$-0.017^{+0.094}_{-0.102}$	$-0.087^{+0.090}_{-0.114}$	$-0.045^{+0.049}_{-0.053}$	$-0.249^{+0.200}_{-0.211}$
$15-35$ GeV/c				
$0-10$	$-0.026^{+0.081}_{-0.086}$	$-0.063^{+0.063}_{-0.075}$	$-0.035^{+0.033}_{-0.039}$	$-0.194^{+0.146}_{-0.161}$
$10-20$	$-0.044^{+0.075}_{-0.082}$	$-0.040^{+0.055}_{-0.063}$	$-0.014^{+0.036}_{-0.038}$	$-0.149^{+0.148}_{-0.161}$
$20-30$	$-0.078^{+0.076}_{-0.084}$	$-0.013^{+0.050}_{-0.059}$	$-0.020^{+0.036}_{-0.039}$	$-0.113^{+0.135}_{-0.154}$
$30-40$	$-0.037^{+0.080}_{-0.085}$	$-0.005^{+0.054}_{-0.062}$	$-0.015^{+0.038}_{-0.041}$	$-0.049^{+0.143}_{-0.153}$
$40-60$	$-0.028^{+0.080}_{-0.088}$	$-0.060^{+0.065}_{-0.075}$	$-0.016^{+0.040}_{-0.044}$	$-0.185^{+0.165}_{-0.176}$

Table A.10: Measured $\Upsilon(1S)$ polarization parameters, in the CS frame. The errors represent the total statistical plus $N_{\rm ch}$-dependent systematic uncertainties.

$\Upsilon(1S)$, CS Frame				
$N_{\rm ch}$	λ_ϑ	λ_φ	$\lambda_{\vartheta\varphi}$	$\tilde{\lambda}$
$10-15$ GeV/c				
$0-10$	$-0.076^{+0.124}_{-0.132}$	$-0.028^{+0.026}_{-0.030}$	$0.041^{+0.036}_{-0.041}$	$-0.149^{+0.134}_{-0.144}$
$10-20$	$0.028^{+0.116}_{-0.129}$	$-0.022^{+0.024}_{-0.028}$	$0.061^{+0.034}_{-0.036}$	$-0.038^{+0.124}_{-0.141}$
$20-30$	$0.078^{+0.122}_{-0.131}$	$-0.021^{+0.027}_{-0.030}$	$0.103^{+0.035}_{-0.039}$	$0.012^{+0.135}_{-0.146}$
$30-40$	$-0.118^{+0.145}_{-0.161}$	$-0.032^{+0.027}_{-0.030}$	$0.029^{+0.039}_{-0.045}$	$-0.196^{+0.157}_{-0.171}$
$40-60$	$-0.075^{+0.186}_{-0.198}$	$-0.057^{+0.031}_{-0.035}$	$0.050^{+0.048}_{-0.054}$	$-0.216^{+0.193}_{-0.204}$
$15-35$ GeV/c				
$0-10$	$-0.056^{+0.117}_{-0.127}$	$-0.048^{+0.028}_{-0.032}$	$0.034^{+0.035}_{-0.037}$	$-0.178^{+0.139}_{-0.152}$
$10-20$	$-0.026^{+0.101}_{-0.113}$	$-0.045^{+0.033}_{-0.036}$	$0.014^{+0.036}_{-0.039}$	$-0.145^{+0.139}_{-0.148}$
$20-30$	$0.032^{+0.096}_{-0.108}$	$-0.052^{+0.035}_{-0.039}$	$0.023^{+0.036}_{-0.039}$	$-0.108^{+0.133}_{-0.147}$
$30-40$	$0.029^{+0.106}_{-0.116}$	$-0.025^{+0.030}_{-0.032}$	$0.016^{+0.038}_{-0.041}$	$-0.039^{+0.128}_{-0.139}$
$40-60$	$-0.051^{+0.114}_{-0.124}$	$-0.046^{+0.037}_{-0.041}$	$0.016^{+0.040}_{-0.046}$	$-0.170^{+0.155}_{-0.162}$

Table A.11: Measured $\Upsilon(2S)$ polarization parameters, in the HX frame. The errors represent the total statistical plus $N_{\rm ch}$-dependent systematic uncertainties.

$\Upsilon(2S)$, HX Frame				
$N_{\rm ch}$	λ_ϑ	λ_φ	$\lambda_{\vartheta\varphi}$	$\tilde{\lambda}$
$10-15$ GeV/c				
$0-10$	$0.233^{+0.167}_{-0.178}$	$-0.018^{+0.041}_{-0.045}$	$-0.048^{+0.053}_{-0.059}$	$0.167^{+0.201}_{-0.214}$
$10-20$	$0.214^{+0.153}_{-0.165}$	$-0.046^{+0.038}_{-0.043}$	$-0.055^{+0.047}_{-0.053}$	$0.075^{+0.187}_{-0.207}$
$20-30$	$0.230^{+0.180}_{-0.198}$	$-0.029^{+0.041}_{-0.046}$	$-0.045^{+0.058}_{-0.066}$	$0.138^{+0.222}_{-0.245}$
$30-40$	$0.267^{+0.229}_{-0.245}$	$-0.024^{+0.049}_{-0.052}$	$-0.059^{+0.077}_{-0.083}$	$0.184^{+0.279}_{-0.307}$
$40-60$	$0.317^{+0.302}_{-0.335}$	$-0.061^{+0.060}_{-0.067}$	$0.023^{+0.105}_{-0.116}$	$0.128^{+0.352}_{-0.384}$
$15-35$ GeV/c				
$0-10$	$0.124^{+0.170}_{-0.183}$	$-0.058^{+0.039}_{-0.044}$	$-0.050^{+0.052}_{-0.058}$	$-0.038^{+0.196}_{-0.210}$
$10-20$	$0.238^{+0.125}_{-0.132}$	$-0.027^{+0.032}_{-0.037}$	$-0.025^{+0.042}_{-0.047}$	$0.150^{+0.153}_{-0.165}$
$20-30$	$0.205^{+0.118}_{-0.136}$	$-0.086^{+0.036}_{-0.038}$	$0.052^{+0.042}_{-0.047}$	$-0.040^{+0.154}_{-0.165}$
$30-40$	$0.501^{+0.151}_{-0.160}$	$-0.020^{+0.038}_{-0.042}$	$-0.077^{+0.051}_{-0.059}$	$0.417^{+0.197}_{-0.200}$
$40-60$	$0.365^{+0.179}_{-0.190}$	$-0.061^{+0.043}_{-0.049}$	$-0.024^{+0.057}_{-0.066}$	$0.170^{+0.213}_{-0.212}$

Table A.12: Measured $\Upsilon(2S)$ polarization parameters, in the PX frame. The errors represent the total statistical plus $N_{\rm ch}$-dependent systematic uncertainties.

$\Upsilon(2S)$, PX Frame				
$N_{\rm ch}$	λ_ϑ	λ_φ	$\lambda_{\vartheta\varphi}$	$\tilde{\lambda}$
$10-15$ GeV/c				
$0-10$	$-0.112^{+0.078}_{-0.085}$	$0.111^{+0.068}_{-0.081}$	$-0.054^{+0.044}_{-0.049}$	$0.222^{+0.200}_{-0.211}$
$10-20$	$-0.130^{+0.077}_{-0.084}$	$0.075^{+0.068}_{-0.078}$	$-0.021^{+0.039}_{-0.044}$	$0.088^{+0.177}_{-0.192}$
$20-30$	$-0.093^{+0.082}_{-0.091}$	$0.066^{+0.084}_{-0.095}$	$-0.010^{+0.044}_{-0.047}$	$0.098^{+0.219}_{-0.241}$
$30-40$	$-0.054^{+0.110}_{-0.122}$	$0.025^{+0.126}_{-0.145}$	$-0.029^{+0.059}_{-0.063}$	$0.014^{+0.305}_{-0.324}$
$40-60$	$-0.073^{+0.129}_{-0.124}$	$0.025^{+0.141}_{-0.176}$	$-0.070^{+0.072}_{-0.082}$	$-0.006^{+0.372}_{-0.380}$
$15-35$ GeV/c				
$0-10$	$-0.101^{+0.093}_{-0.097}$	$-0.003^{+0.080}_{-0.100}$	$0.019^{+0.046}_{-0.052}$	$-0.115^{+0.206}_{-0.208}$
$10-20$	$-0.114^{+0.071}_{-0.081}$	$0.085^{+0.057}_{-0.067}$	$-0.035^{+0.031}_{-0.035}$	$0.135^{+0.152}_{-0.161}$
$20-30$	$-0.154^{+0.076}_{-0.085}$	$0.048^{+0.059}_{-0.065}$	$-0.086^{+0.032}_{-0.035}$	$-0.018^{+0.149}_{-0.168}$
$30-40$	$-0.206^{+0.082}_{-0.088}$	$0.190^{+0.057}_{-0.069}$	$-0.022^{+0.037}_{-0.040}$	$0.401^{+0.193}_{-0.197}$
$40-60$	$-0.172^{+0.088}_{-0.094}$	$0.098^{+0.071}_{-0.087}$	$-0.043^{+0.046}_{-0.050}$	$0.110^{+0.208}_{-0.206}$

Table A.13: Measured $\Upsilon(2S)$ polarization parameters, in the CS frame. The errors represent the total statistical plus N_{ch}-dependent systematic uncertainties.

$\Upsilon(2S)$, CS Frame				
N_{ch}	λ_ϑ	λ_φ	$\lambda_{\vartheta\varphi}$	$\tilde{\lambda}$
$10-15$ GeV/c				
$0-10$	$0.326^{+0.162}_{-0.175}$	$-0.016^{+0.032}_{-0.036}$	$0.085^{+0.052}_{-0.057}$	$0.253^{+0.189}_{-0.200}$
$10-20$	$0.255^{+0.156}_{-0.173}$	$-0.047^{+0.030}_{-0.033}$	$0.042^{+0.044}_{-0.048}$	$0.102^{+0.171}_{-0.186}$
$20-30$	$0.219^{+0.196}_{-0.211}$	$-0.028^{+0.034}_{-0.038}$	$0.026^{+0.049}_{-0.054}$	$0.121^{+0.214}_{-0.238}$
$30-40$	$0.152^{+0.262}_{-0.282}$	$-0.026^{+0.040}_{-0.043}$	$0.045^{+0.064}_{-0.072}$	$0.067^{+0.288}_{-0.308}$
$40-60$	$0.202^{+0.323}_{-0.346}$	$-0.034^{+0.048}_{-0.052}$	$0.098^{+0.083}_{-0.087}$	$0.091^{+0.375}_{-0.394}$
$15-35$ GeV/c				
$0-10$	$0.093^{+0.164}_{-0.175}$	$-0.062^{+0.035}_{-0.038}$	$-0.016^{+0.048}_{-0.052}$	$-0.077^{+0.184}_{-0.189}$
$10-20$	$0.222^{+0.123}_{-0.133}$	$-0.023^{+0.029}_{-0.032}$	$0.046^{+0.033}_{-0.038}$	$0.148^{+0.140}_{-0.150}$
$20-30$	$0.183^{+0.124}_{-0.137}$	$-0.066^{+0.029}_{-0.033}$	$0.103^{+0.034}_{-0.038}$	$-0.005^{+0.145}_{-0.155}$
$30-40$	$0.507^{+0.153}_{-0.163}$	$-0.021^{+0.033}_{-0.037}$	$0.044^{+0.043}_{-0.048}$	$0.426^{+0.184}_{-0.187}$
$40-60$	$0.308^{+0.182}_{-0.189}$	$-0.051^{+0.040}_{-0.043}$	$0.060^{+0.053}_{-0.057}$	$0.148^{+0.202}_{-0.206}$

Table A.14: Measured $\Upsilon(3S)$ polarization parameters, in the HX frame. The errors represent the total statistical plus $N_{\rm ch}$-dependent systematic uncertainties.

$\Upsilon(3S)$, HX Frame				
$N_{\rm ch}$	λ_ϑ	λ_φ	$\lambda_{\vartheta\varphi}$	$\tilde{\lambda}$
$10-15$ GeV/c				
$0-10$	$0.075^{+0.195}_{-0.206}$	$-0.028^{+0.044}_{-0.049}$	$-0.045^{+0.063}_{-0.074}$	$-0.001^{+0.227}_{-0.249}$
$10-20$	$0.279^{+0.183}_{-0.192}$	$-0.019^{+0.043}_{-0.047}$	$-0.148^{+0.062}_{-0.067}$	$0.208^{+0.234}_{-0.251}$
$20-30$	$0.062^{+0.211}_{-0.228}$	$-0.032^{+0.046}_{-0.052}$	$0.061^{+0.074}_{-0.082}$	$-0.023^{+0.262}_{-0.283}$
$30-60$	$0.671^{+0.299}_{-0.313}$	$0.051^{+0.064}_{-0.070}$	$-0.196^{+0.109}_{-0.118}$	$0.802^{+0.453}_{-0.488}$
$15-35$ GeV/c				
$0-10$	$0.382^{+0.196}_{-0.197}$	$-0.074^{+0.043}_{-0.049}$	$0.048^{+0.062}_{-0.071}$	$0.148^{+0.218}_{-0.226}$
$10-20$	$0.245^{+0.134}_{-0.153}$	$-0.029^{+0.039}_{-0.043}$	$-0.035^{+0.045}_{-0.051}$	$0.151^{+0.178}_{-0.193}$
$20-30$	$0.285^{+0.140}_{-0.148}$	$-0.047^{+0.036}_{-0.040}$	$-0.053^{+0.046}_{-0.050}$	$0.136^{+0.171}_{-0.182}$
$30-40$	$0.221^{+0.173}_{-0.179}$	$-0.121^{+0.044}_{-0.048}$	$-0.050^{+0.058}_{-0.063}$	$-0.113^{+0.202}_{-0.204}$
$40-60$	$0.281^{+0.226}_{-0.218}$	$-0.072^{+0.049}_{-0.053}$	$-0.143^{+0.068}_{-0.078}$	$0.058^{+0.260}_{-0.246}$

Table A.15: Measured $\Upsilon(3S)$ polarization parameters, in the PX frame. The errors represent the total statistical plus N_{ch}-dependent systematic uncertainties.

$\Upsilon(3S)$, PX Frame				
N_{ch}	λ_ϑ	λ_φ	$\lambda_{\vartheta\varphi}$	$\tilde{\lambda}$
$10-15$ GeV/c				
$0-10$	$-0.068^{+0.095}_{-0.097}$	$0.022^{+0.085}_{-0.109}$	$0.030^{+0.056}_{-0.059}$	$-0.019^{+0.229}_{-0.239}$
$10-20$	$-0.168^{+0.084}_{-0.090}$	$0.130^{+0.081}_{-0.093}$	$0.034^{+0.045}_{-0.049}$	$0.228^{+0.232}_{-0.252}$
$20-30$	$0.015^{+0.108}_{-0.113}$	$-0.024^{+0.120}_{-0.137}$	$-0.080^{+0.053}_{-0.058}$	$-0.051^{+0.273}_{-0.299}$
$30-60$	$-0.187^{+0.100}_{-0.107}$	$0.276^{+0.127}_{-0.139}$	$-0.020^{+0.055}_{-0.061}$	$0.836^{+0.517}_{-0.577}$
$15-35$ GeV/c				
$0-10$	$-0.165^{+0.099}_{-0.100}$	$0.103^{+0.078}_{-0.100}$	$-0.125^{+0.049}_{-0.054}$	$0.118^{+0.236}_{-0.224}$
$10-20$	$-0.142^{+0.080}_{-0.085}$	$0.109^{+0.062}_{-0.073}$	$-0.027^{+0.035}_{-0.038}$	$0.184^{+0.184}_{-0.199}$
$20-30$	$-0.186^{+0.079}_{-0.084}$	$0.120^{+0.059}_{-0.072}$	$-0.027^{+0.034}_{-0.038}$	$0.172^{+0.177}_{-0.186}$
$30-40$	$-0.242^{+0.085}_{-0.092}$	$0.054^{+0.077}_{-0.094}$	$-0.034^{+0.046}_{-0.050}$	$-0.097^{+0.210}_{-0.217}$
$40-60$	$-0.225^{+0.106}_{-0.107}$	$0.090^{+0.090}_{-0.115}$	$0.061^{+0.057}_{-0.062}$	$0.011^{+0.268}_{-0.245}$

Table A.16: Measured $\Upsilon(3S)$ polarization parameters, in the CS frame. The errors represent the total statistical plus N_{ch}-dependent systematic uncertainties.

$\Upsilon(3S)$, CS Frame				
N_{ch}	λ_ϑ	λ_φ	$\lambda_{\vartheta\varphi}$	$\tilde{\lambda}$
$10-15$ GeV/c				
$0-10$	$0.142^{+0.211}_{-0.218}$	$-0.036^{+0.037}_{-0.040}$	$-0.021^{+0.060}_{-0.067}$	$0.030^{+0.223}_{-0.235}$
$10-20$	$0.409^{+0.195}_{-0.215}$	$-0.044^{+0.035}_{-0.040}$	$-0.020^{+0.051}_{-0.058}$	$0.251^{+0.228}_{-0.241}$
$20-30$	$0.016^{+0.230}_{-0.252}$	$-0.009^{+0.039}_{-0.043}$	$0.090^{+0.054}_{-0.061}$	$-0.014^{+0.265}_{-0.281}$
$30-60$	$0.825^{+0.374}_{-0.424}$	$0.033^{+0.052}_{-0.059}$	$0.067^{+0.074}_{-0.082}$	$0.894^{+0.502}_{-0.570}$
$15-35$ GeV/c				
$0-10$	$0.327^{+0.197}_{-0.201}$	$-0.047^{+0.041}_{-0.046}$	$0.157^{+0.057}_{-0.061}$	$0.173^{+0.218}_{-0.212}$
$10-20$	$0.292^{+0.138}_{-0.152}$	$-0.027^{+0.033}_{-0.036}$	$0.041^{+0.040}_{-0.044}$	$0.203^{+0.167}_{-0.175}$
$20-30$	$0.345^{+0.140}_{-0.155}$	$-0.048^{+0.032}_{-0.035}$	$0.044^{+0.040}_{-0.043}$	$0.192^{+0.158}_{-0.174}$
$30-40$	$0.273^{+0.178}_{-0.185}$	$-0.120^{+0.039}_{-0.043}$	$0.052^{+0.052}_{-0.057}$	$-0.064^{+0.197}_{-0.205}$
$40-60$	$0.343^{+0.236}_{-0.225}$	$-0.090^{+0.044}_{-0.049}$	$-0.058^{+0.064}_{-0.072}$	$0.070^{+0.255}_{-0.238}$

Table A.17: Measured J/ψ polarization parameters, in the HX frame. The errors represent the total statistical plus N_{ch}-dependent systematic uncertainties.

J/ψ, HX Frame				
N_{ch}	λ_ϑ	λ_φ	$\lambda_{\vartheta\varphi}$	$\tilde{\lambda}$
$14-20$ GeV/c				
$0-10$	$-0.101^{+0.066}_{-0.071}$	$-0.027^{+0.009}_{-0.010}$	$0.034^{+0.013}_{-0.015}$	$-0.177^{+0.062}_{-0.069}$
$10-16$	$-0.082^{+0.053}_{-0.062}$	$-0.020^{+0.005}_{-0.006}$	$0.028^{+0.010}_{-0.011}$	$-0.140^{+0.054}_{-0.061}$
$16-20$	$0.067^{+0.056}_{-0.065}$	$-0.025^{+0.010}_{-0.011}$	$0.030^{+0.014}_{-0.017}$	$-0.007^{+0.059}_{-0.067}$
$20-24$	$0.040^{+0.056}_{-0.062}$	$-0.026^{+0.006}_{-0.006}$	$0.023^{+0.013}_{-0.015}$	$-0.037^{+0.059}_{-0.062}$
$24-28$	$-0.011^{+0.060}_{-0.067}$	$-0.019^{+0.007}_{-0.008}$	$0.023^{+0.014}_{-0.016}$	$-0.066^{+0.062}_{-0.069}$
$28-32$	$-0.050^{+0.060}_{-0.066}$	$-0.017^{+0.009}_{-0.010}$	$0.015^{+0.013}_{-0.015}$	$-0.099^{+0.067}_{-0.069}$
$32-36$	$-0.046^{+0.067}_{-0.073}$	$-0.023^{+0.007}_{-0.008}$	$0.036^{+0.017}_{-0.018}$	$-0.113^{+0.067}_{-0.075}$
$36-40$	$0.162^{+0.076}_{-0.086}$	$-0.028^{+0.008}_{-0.009}$	$0.020^{+0.016}_{-0.018}$	$0.075^{+0.084}_{-0.085}$
$40-44$	$0.031^{+0.086}_{-0.092}$	$-0.017^{+0.010}_{-0.010}$	$0.026^{+0.019}_{-0.020}$	$-0.020^{+0.091}_{-0.094}$
$44-50$	$0.092^{+0.092}_{-0.096}$	$-0.009^{+0.009}_{-0.010}$	$0.011^{+0.018}_{-0.020}$	$0.063^{+0.093}_{-0.096}$
$50-60$	$-0.033^{+0.100}_{-0.110}$	$-0.014^{+0.012}_{-0.013}$	$0.010^{+0.024}_{-0.027}$	$-0.075^{+0.105}_{-0.106}$
$60-100$	$0.262^{+0.142}_{-0.149}$	$-0.031^{+0.015}_{-0.016}$	$-0.004^{+0.029}_{-0.033}$	$0.162^{+0.150}_{-0.149}$
$20-35$ GeV/c				
$0-10$	$-0.038^{+0.082}_{-0.084}$	$-0.007^{+0.017}_{-0.020}$	$0.045^{+0.023}_{-0.026}$	$-0.059^{+0.095}_{-0.093}$
$10-16$	$-0.040^{+0.056}_{-0.063}$	$-0.029^{+0.012}_{-0.013}$	$0.001^{+0.015}_{-0.016}$	$-0.125^{+0.067}_{-0.068}$
$16-20$	$0.024^{+0.063}_{-0.065}$	$-0.018^{+0.011}_{-0.012}$	$0.008^{+0.016}_{-0.018}$	$-0.029^{+0.064}_{-0.068}$
$20-24$	$0.077^{+0.057}_{-0.060}$	$-0.027^{+0.011}_{-0.012}$	$0.011^{+0.014}_{-0.016}$	$-0.003^{+0.064}_{-0.065}$
$24-28$	$0.132^{+0.056}_{-0.060}$	$-0.029^{+0.011}_{-0.012}$	$0.009^{+0.015}_{-0.017}$	$0.044^{+0.063}_{-0.068}$
$28-32$	$0.042^{+0.060}_{-0.062}$	$-0.026^{+0.012}_{-0.013}$	$0.014^{+0.016}_{-0.018}$	$-0.034^{+0.065}_{-0.068}$
$32-36$	$0.070^{+0.064}_{-0.066}$	$-0.026^{+0.012}_{-0.013}$	$-0.003^{+0.018}_{-0.019}$	$-0.007^{+0.073}_{-0.074}$
$36-40$	$0.103^{+0.070}_{-0.075}$	$-0.011^{+0.014}_{-0.015}$	$0.022^{+0.021}_{-0.022}$	$0.069^{+0.082}_{-0.083}$
$40-44$	$0.131^{+0.085}_{-0.086}$	$-0.002^{+0.016}_{-0.018}$	$-0.030^{+0.022}_{-0.025}$	$0.125^{+0.098}_{-0.101}$
$44-50$	$0.120^{+0.081}_{-0.083}$	$-0.045^{+0.018}_{-0.020}$	$-0.001^{+0.021}_{-0.024}$	$-0.016^{+0.087}_{-0.092}$
$50-60$	$0.115^{+0.087}_{-0.096}$	$-0.011^{+0.017}_{-0.018}$	$0.029^{+0.022}_{-0.025}$	$0.080^{+0.106}_{-0.109}$
$60-100$	$0.090^{+0.119}_{-0.119}$	$-0.018^{+0.024}_{-0.025}$	$-0.016^{+0.032}_{-0.034}$	$0.037^{+0.139}_{-0.139}$

Table A.18: Measured J/ψ polarization parameters, in the PX frame. The errors represent the total statistical plus N_{ch}-dependent systematic uncertainties.

J/ψ, PX Frame				
N_{ch}	λ_ϑ	λ_φ	$\lambda_{\vartheta\varphi}$	$\tilde{\lambda}$
$14-20$ GeV/c				
$0-10$	$0.028^{+0.040}_{-0.043}$	$-0.078^{+0.033}_{-0.043}$	$-0.022^{+0.016}_{-0.017}$	$-0.195^{+0.065}_{-0.069}$
$10-16$	$0.018^{+0.034}_{-0.036}$	$-0.055^{+0.032}_{-0.039}$	$-0.021^{+0.012}_{-0.013}$	$-0.142^{+0.060}_{-0.067}$
$16-20$	$-0.055^{+0.031}_{-0.032}$	$0.015^{+0.025}_{-0.032}$	$-0.036^{+0.011}_{-0.013}$	$-0.013^{+0.058}_{-0.066}$
$20-24$	$-0.054^{+0.030}_{-0.028}$	$0.008^{+0.026}_{-0.033}$	$-0.026^{+0.011}_{-0.012}$	$-0.033^{+0.061}_{-0.065}$
$24-28$	$-0.007^{+0.035}_{-0.037}$	$-0.025^{+0.032}_{-0.038}$	$-0.021^{+0.013}_{-0.013}$	$-0.084^{+0.062}_{-0.069}$
$28-32$	$0.003^{+0.035}_{-0.035}$	$-0.035^{+0.033}_{-0.040}$	$-0.010^{+0.013}_{-0.015}$	$-0.100^{+0.068}_{-0.070}$
$32-36$	$0.001^{+0.040}_{-0.039}$	$-0.041^{+0.033}_{-0.041}$	$-0.033^{+0.013}_{-0.015}$	$-0.120^{+0.071}_{-0.077}$
$36-40$	$-0.101^{+0.037}_{-0.036}$	$0.055^{+0.034}_{-0.041}$	$-0.033^{+0.015}_{-0.016}$	$0.063^{+0.085}_{-0.087}$
$40-44$	$-0.016^{+0.047}_{-0.046}$	$-0.012^{+0.041}_{-0.051}$	$-0.028^{+0.017}_{-0.018}$	$-0.056^{+0.092}_{-0.098}$
$44-50$	$-0.043^{+0.047}_{-0.047}$	$0.028^{+0.041}_{-0.053}$	$-0.018^{+0.020}_{-0.022}$	$0.038^{+0.099}_{-0.104}$
$50-60$	$0.009^{+0.062}_{-0.060}$	$-0.035^{+0.049}_{-0.066}$	$-0.005^{+0.020}_{-0.022}$	$-0.099^{+0.107}_{-0.114}$
$60-100$	$-0.118^{+0.064}_{-0.060}$	$0.064^{+0.056}_{-0.073}$	$-0.016^{+0.025}_{-0.027}$	$0.068^{+0.159}_{-0.161}$
$20-35$ GeV/c				
$0-10$	$0.018^{+0.052}_{-0.051}$	$-0.027^{+0.040}_{-0.048}$	$-0.041^{+0.024}_{-0.026}$	$-0.065^{+0.100}_{-0.099}$
$10-16$	$-0.020^{+0.035}_{-0.037}$	$-0.039^{+0.031}_{-0.036}$	$0.002^{+0.015}_{-0.017}$	$-0.132^{+0.071}_{-0.076}$
$16-20$	$-0.034^{+0.038}_{-0.037}$	$-0.000^{+0.031}_{-0.036}$	$-0.008^{+0.015}_{-0.017}$	$-0.036^{+0.067}_{-0.070}$
$20-24$	$-0.070^{+0.032}_{-0.033}$	$0.021^{+0.027}_{-0.032}$	$-0.017^{+0.014}_{-0.015}$	$-0.008^{+0.068}_{-0.072}$
$24-28$	$-0.091^{+0.029}_{-0.030}$	$0.040^{+0.025}_{-0.030}$	$-0.016^{+0.014}_{-0.016}$	$0.028^{+0.064}_{-0.070}$
$28-32$	$-0.044^{+0.034}_{-0.036}$	$-0.002^{+0.028}_{-0.033}$	$-0.016^{+0.015}_{-0.017}$	$-0.052^{+0.068}_{-0.073}$
$32-36$	$-0.070^{+0.036}_{-0.035}$	$0.020^{+0.031}_{-0.035}$	$-0.003^{+0.016}_{-0.019}$	$-0.011^{+0.075}_{-0.078}$
$36-40$	$-0.055^{+0.040}_{-0.041}$	$0.038^{+0.031}_{-0.037}$	$-0.025^{+0.018}_{-0.020}$	$0.057^{+0.083}_{-0.086}$
$40-44$	$-0.055^{+0.045}_{-0.046}$	$0.049^{+0.037}_{-0.045}$	$0.024^{+0.021}_{-0.023}$	$0.093^{+0.099}_{-0.107}$
$44-50$	$-0.117^{+0.042}_{-0.043}$	$0.034^{+0.036}_{-0.044}$	$-0.009^{+0.020}_{-0.021}$	$-0.020^{+0.092}_{-0.093}$
$50-60$	$-0.059^{+0.050}_{-0.050}$	$0.042^{+0.039}_{-0.047}$	$-0.035^{+0.021}_{-0.024}$	$0.067^{+0.114}_{-0.114}$
$60-100$	$-0.072^{+0.063}_{-0.060}$	$0.036^{+0.051}_{-0.065}$	$0.010^{+0.031}_{-0.035}$	$0.033^{+0.148}_{-0.149}$

Table A.19: Measured J/ψ polarization parameters, in the CS frame. The errors represent the total statistical plus N_{ch}-dependent systematic uncertainties.

J/ψ, CS Frame				
N_{ch}	λ_ϑ	λ_φ	$\lambda_{\vartheta\varphi}$	$\tilde{\lambda}$
$14-20$ GeV/c				
$0-10$	$-0.119^{+0.065}_{-0.069}$	$-0.024^{+0.010}_{-0.011}$	$0.022^{+0.015}_{-0.017}$	$-0.186^{+0.063}_{-0.068}$
$10-16$	$-0.084^{+0.053}_{-0.061}$	$-0.018^{+0.006}_{-0.007}$	$0.020^{+0.013}_{-0.014}$	$-0.136^{+0.056}_{-0.062}$
$16-20$	$0.055^{+0.056}_{-0.065}$	$-0.021^{+0.007}_{-0.007}$	$0.037^{+0.014}_{-0.016}$	$-0.008^{+0.057}_{-0.065}$
$20-24$	$0.041^{+0.056}_{-0.061}$	$-0.023^{+0.006}_{-0.007}$	$0.027^{+0.011}_{-0.012}$	$-0.030^{+0.056}_{-0.063}$
$24-28$	$-0.027^{+0.059}_{-0.066}$	$-0.016^{+0.009}_{-0.010}$	$0.021^{+0.013}_{-0.014}$	$-0.076^{+0.060}_{-0.066}$
$28-32$	$-0.047^{+0.061}_{-0.064}$	$-0.016^{+0.008}_{-0.009}$	$0.010^{+0.012}_{-0.014}$	$-0.093^{+0.064}_{-0.067}$
$32-36$	$-0.052^{+0.065}_{-0.073}$	$-0.020^{+0.007}_{-0.008}$	$0.033^{+0.013}_{-0.014}$	$-0.110^{+0.066}_{-0.075}$
$36-40$	$0.153^{+0.078}_{-0.083}$	$-0.025^{+0.008}_{-0.009}$	$0.036^{+0.015}_{-0.017}$	$0.075^{+0.080}_{-0.084}$
$40-44$	$0.001^{+0.085}_{-0.092}$	$-0.014^{+0.010}_{-0.010}$	$0.028^{+0.017}_{-0.019}$	$-0.040^{+0.091}_{-0.093}$
$44-50$	$0.076^{+0.089}_{-0.095}$	$-0.007^{+0.011}_{-0.012}$	$0.019^{+0.020}_{-0.022}$	$0.052^{+0.094}_{-0.095}$
$50-60$	$-0.040^{+0.102}_{-0.107}$	$-0.013^{+0.010}_{-0.011}$	$0.005^{+0.020}_{-0.023}$	$-0.079^{+0.102}_{-0.111}$
$60-100$	$0.199^{+0.144}_{-0.148}$	$-0.030^{+0.014}_{-0.017}$	$0.018^{+0.028}_{-0.030}$	$0.105^{+0.146}_{-0.147}$
$20-35$ GeV/c				
$0-10$	$-0.037^{+0.081}_{-0.084}$	$-0.004^{+0.017}_{-0.020}$	$0.040^{+0.023}_{-0.027}$	$-0.051^{+0.092}_{-0.094}$
$10-16$	$-0.042^{+0.059}_{-0.064}$	$-0.029^{+0.013}_{-0.014}$	$-0.001^{+0.014}_{-0.017}$	$-0.126^{+0.067}_{-0.071}$
$16-20$	$0.022^{+0.062}_{-0.067}$	$-0.017^{+0.011}_{-0.012}$	$0.008^{+0.015}_{-0.017}$	$-0.030^{+0.064}_{-0.070}$
$20-24$	$0.074^{+0.057}_{-0.061}$	$-0.026^{+0.011}_{-0.012}$	$0.018^{+0.014}_{-0.016}$	$-0.003^{+0.063}_{-0.066}$
$24-28$	$0.119^{+0.055}_{-0.062}$	$-0.027^{+0.011}_{-0.012}$	$0.017^{+0.015}_{-0.017}$	$0.034^{+0.062}_{-0.068}$
$28-32$	$0.025^{+0.059}_{-0.063}$	$-0.024^{+0.013}_{-0.014}$	$0.016^{+0.016}_{-0.017}$	$-0.045^{+0.065}_{-0.066}$
$32-36$	$0.074^{+0.064}_{-0.066}$	$-0.026^{+0.012}_{-0.013}$	$0.003^{+0.018}_{-0.019}$	$-0.004^{+0.071}_{-0.075}$
$36-40$	$0.095^{+0.072}_{-0.076}$	$-0.009^{+0.014}_{-0.016}$	$0.026^{+0.018}_{-0.020}$	$0.067^{+0.079}_{-0.083}$
$40-44$	$0.115^{+0.082}_{-0.086}$	$-0.003^{+0.016}_{-0.018}$	$-0.025^{+0.022}_{-0.025}$	$0.106^{+0.094}_{-0.103}$
$44-50$	$0.128^{+0.082}_{-0.086}$	$-0.046^{+0.017}_{-0.018}$	$0.010^{+0.022}_{-0.024}$	$-0.011^{+0.088}_{-0.090}$
$50-60$	$0.109^{+0.087}_{-0.091}$	$-0.009^{+0.016}_{-0.018}$	$0.037^{+0.022}_{-0.025}$	$0.080^{+0.102}_{-0.110}$
$60-100$	$0.115^{+0.114}_{-0.120}$	$-0.019^{+0.022}_{-0.026}$	$-0.011^{+0.032}_{-0.036}$	$0.056^{+0.136}_{-0.141}$

Table A.20: Measured $\psi(2S)$ polarization parameters, in the HX frame. The errors represent the total statistical plus N_{ch}-dependent systematic uncertainties.

$\psi(2S)$, HX Frame				
N_{ch}	λ_ϑ	λ_φ	$\lambda_{\vartheta\varphi}$	$\tilde{\lambda}$
$14-20$ GeV/c				
$0-15$	$-0.099^{+0.141}_{-0.148}$	$-0.028^{+0.017}_{-0.019}$	$-0.002^{+0.032}_{-0.037}$	$-0.181^{+0.144}_{-0.154}$
$15-25$	$0.304^{+0.135}_{-0.145}$	$-0.026^{+0.014}_{-0.016}$	$-0.038^{+0.029}_{-0.031}$	$0.217^{+0.144}_{-0.152}$
$25-35$	$0.007^{+0.141}_{-0.149}$	$-0.034^{+0.017}_{-0.019}$	$0.086^{+0.032}_{-0.038}$	$-0.094^{+0.148}_{-0.148}$
$35-45$	$-0.037^{+0.215}_{-0.216}$	$-0.051^{+0.024}_{-0.026}$	$0.053^{+0.042}_{-0.051}$	$-0.182^{+0.217}_{-0.216}$
$45-100$	$0.333^{+0.270}_{-0.274}$	$-0.040^{+0.031}_{-0.034}$	$0.092^{+0.059}_{-0.066}$	$0.207^{+0.281}_{-0.269}$
$20-35$ GeV/c				
$0-15$	$-0.467^{+0.178}_{-0.166}$	$-0.093^{+0.034}_{-0.040}$	$0.041^{+0.051}_{-0.056}$	$-0.683^{+0.188}_{-0.172}$
$15-25$	$-0.304^{+0.134}_{-0.135}$	$0.020^{+0.026}_{-0.029}$	$0.083^{+0.035}_{-0.041}$	$-0.248^{+0.173}_{-0.173}$
$25-35$	$0.057^{+0.158}_{-0.163}$	$-0.047^{+0.029}_{-0.033}$	$0.069^{+0.038}_{-0.045}$	$-0.084^{+0.171}_{-0.167}$
$35-45$	$0.083^{+0.213}_{-0.204}$	$-0.026^{+0.040}_{-0.043}$	$0.010^{+0.051}_{-0.056}$	$0.000^{+0.263}_{-0.236}$
$45-100$	$-0.128^{+0.203}_{-0.207}$	$-0.077^{+0.044}_{-0.046}$	$0.166^{+0.059}_{-0.067}$	$-0.333^{+0.216}_{-0.213}$

Table A.21: Measured $\psi(2S)$ polarization parameters, in the PX frame. The errors represent the total statistical plus N_{ch}-dependent systematic uncertainties.

$\psi(2S)$, PX Frame				
N_{ch}	λ_ϑ	λ_φ	$\lambda_{\vartheta\varphi}$	$\tilde{\lambda}$
$14-20$ GeV/c				
$0-15$	$0.041^{+0.092}_{-0.078}$	$-0.104^{+0.067}_{-0.102}$	$0.019^{+0.033}_{-0.037}$	$-0.259^{+0.148}_{-0.149}$
$15-25$	$-0.163^{+0.059}_{-0.053}$	$0.114^{+0.053}_{-0.068}$	$-0.002^{+0.024}_{-0.025}$	$0.195^{+0.161}_{-0.168}$
$25-35$	$-0.008^{+0.083}_{-0.071}$	$-0.041^{+0.068}_{-0.094}$	$-0.091^{+0.033}_{-0.034}$	$-0.136^{+0.159}_{-0.159}$
$35-45$	$0.006^{+0.140}_{-0.117}$	$-0.096^{+0.107}_{-0.161}$	$-0.043^{+0.045}_{-0.048}$	$-0.281^{+0.242}_{-0.247}$
$45-100$	$-0.111^{+0.143}_{-0.112}$	$0.063^{+0.098}_{-0.158}$	$-0.113^{+0.050}_{-0.059}$	$0.055^{+0.306}_{-0.309}$
$20-35$ GeV/c				
$0-15$	$0.147^{+0.176}_{-0.131}$	$-0.377^{+0.116}_{-0.187}$	$-0.009^{+0.065}_{-0.069}$	$-0.733^{+0.209}_{-0.199}$
$15-25$	$0.275^{+0.123}_{-0.108}$	$-0.210^{+0.086}_{-0.117}$	$-0.064^{+0.048}_{-0.051}$	$-0.299^{+0.186}_{-0.189}$
$25-35$	$-0.070^{+0.097}_{-0.093}$	$-0.008^{+0.073}_{-0.095}$	$-0.073^{+0.038}_{-0.041}$	$-0.104^{+0.190}_{-0.187}$
$35-45$	$-0.071^{+0.117}_{-0.106}$	$0.022^{+0.089}_{-0.114}$	$-0.017^{+0.049}_{-0.054}$	$-0.028^{+0.255}_{-0.213}$
$45-100$	$0.016^{+0.158}_{-0.118}$	$-0.146^{+0.098}_{-0.163}$	$-0.171^{+0.066}_{-0.072}$	$-0.400^{+0.244}_{-0.226}$

Table A.22: Measured $\psi(2S)$ polarization parameters, in the CS frame. The errors represent the total statistical plus N_{ch}-dependent systematic uncertainties.

$\psi(2S)$, CS Frame				
N_{ch}	λ_ϑ	λ_φ	$\lambda_{\vartheta\varphi}$	$\tilde{\lambda}$
$14-20$ GeV/c				
$0-15$	$-0.135^{+0.135}_{-0.145}$	$-0.029^{+0.016}_{-0.017}$	$-0.017^{+0.032}_{-0.033}$	$-0.216^{+0.140}_{-0.149}$
$15-25$	$0.313^{+0.134}_{-0.148}$	$-0.028^{+0.013}_{-0.016}$	$0.002^{+0.027}_{-0.030}$	$0.219^{+0.144}_{-0.155}$
$25-35$	$-0.028^{+0.138}_{-0.143}$	$-0.024^{+0.016}_{-0.018}$	$0.090^{+0.032}_{-0.035}$	$-0.098^{+0.149}_{-0.148}$
$35-45$	$-0.094^{+0.207}_{-0.209}$	$-0.044^{+0.025}_{-0.026}$	$0.042^{+0.043}_{-0.045}$	$-0.217^{+0.215}_{-0.221}$
$45-100$	$0.237^{+0.271}_{-0.261}$	$-0.025^{+0.030}_{-0.035}$	$0.127^{+0.056}_{-0.061}$	$0.153^{+0.281}_{-0.260}$
$20-35$ GeV/c				
$0-15$	$-0.480^{+0.183}_{-0.161}$	$-0.090^{+0.034}_{-0.040}$	$0.008^{+0.050}_{-0.055}$	$-0.691^{+0.187}_{-0.161}$
$15-25$	$-0.341^{+0.133}_{-0.128}$	$0.026^{+0.027}_{-0.029}$	$0.052^{+0.039}_{-0.045}$	$-0.270^{+0.176}_{-0.169}$
$25-35$	$0.055^{+0.149}_{-0.157}$	$-0.042^{+0.030}_{-0.032}$	$0.076^{+0.039}_{-0.044}$	$-0.071^{+0.173}_{-0.165}$
$35-45$	$0.115^{+0.218}_{-0.210}$	$-0.026^{+0.038}_{-0.044}$	$0.018^{+0.051}_{-0.055}$	$0.031^{+0.258}_{-0.243}$
$45-100$	$-0.167^{+0.199}_{-0.195}$	$-0.064^{+0.044}_{-0.047}$	$0.158^{+0.064}_{-0.066}$	$-0.340^{+0.223}_{-0.210}$

Bibliography

[1] P. A. R. Ade et al. Planck 2015 results. XIII. Cosmological parameters. *Astron. Astrophys.*, 594:A13, 2016.

[2] Bharat Ratra, Michael S. Vogeley, and Michael S. Vogeley. The Beginning and Evolution of the Universe. *Publ. Astron. Soc. Pac.*, 120:235–265, 2008.

[3] H. Hahn et al. The RHIC design overview. *Nucl. Instrum. Meth.*, A499:245–263, 2003.

[4] Sheldon L. Glashow. Partial-symmetries of weak interactions. *Nuclear Physics*, 22(4):579 – 588, 1961.

[5] Georges Aad et al. Combined Measurement of the Higgs Boson Mass in pp Collisions at $\sqrt{s} = 7$ and 8 TeV with the ATLAS and CMS Experiments. *Phys. Rev. Lett.*, 114:191803, 2015.

[6] W. Heisenberg. Über den bau der atomkerne. i. *Zeitschrift für Physik*, 77(1):1–11, 1932.

[7] Hideki Yukawa. On the Interaction of Elementary Particles I. *Proc. Phys. Math. Soc. Jap.*, 17:48–57, 1935. [Prog. Theor. Phys. Suppl.1,1(1935)].

[8] Seth H. Neddermeyer and Carl D. Anderson. Note on the nature of cosmic-ray particles. *Phys. Rev.*, 51:884–886, May 1937.

[9] C. M. G. Lattes, H. Muirhead, G. P. S. Occhialini, and C. F. Powell. Processing involving charged mesons. *Nature*, 159:694–697, 1947.

[10] Tadao Nakano and Kazuhiko Nishijima. Charge independence for v-particles*. *Progress of Theoretical Physics*, 10(5):581, 1953.

[11] M. Gell-Mann. Isotopic spin and new unstable particles. *Phys. Rev.*, 92:833–834, Nov 1953.

[12] Murray Gell-Mann. The Eightfold Way: A Theory of strong interaction symmetry. 1961.

[13] Y. Ne'eman. Derivation of strong interactions from a gauge invariance. *Nuclear Physics*, 26(2):222 – 229, 1961.

[14] A. Pevsner, R. Kraemer, M. Nussbaum, C. Richardson, P. Schlein, R. Strand, T. Toohig, M. Block, A. Engler, R. Gessaroli, and C. Meltzer. Evidence for a three-pion resonance near 550 mev. *Phys. Rev. Lett.*, 7:421–423, Dec 1961.

[15] V. E. Barnes et al. Observation of a Hyperon with Strangeness -3. *Phys. Rev. Lett.*, 12:204–206, 1964.

[16] Murray Gell-Mann. A Schematic Model of Baryons and Mesons. *Phys. Lett.*, 8:214–215, 1964.

[17] G. Zweig. An SU(3) model for strong interaction symmetry and its breaking. Version 1. 1964.

[18] Jerome I. Friedman and Henry W. Kendall. Deep inelastic electron scattering. *Ann. Rev. Nucl. Part. Sci.*, 22:203–254, 1972.

[19] O. W. Greenberg. Spin and unitary-spin independence in a paraquark model of baryons and mesons. *Phys. Rev. Lett.*, 13:598–602, Nov 1964.

[20] William A. Bardeen, H. Fritzsch, and Murray Gell-Mann. Light cone current algebra, pi0 decay, and e+ e- annihilation. In *Topical Meeting on the Outlook for Broken Conformal Symmetry in Elementary Particle Physics Frascati, Italy, May 4-5, 1972*, 1972.

[21] D. Griffiths. *Introduction to Elementary Particles*. Physics textbook. Wiley, 2008.

[22] David J. Gross and Frank Wilczek. Ultraviolet Behavior of Nonabelian Gauge Theories. *Phys. Rev. Lett.*, 30:1343–1346, 1973.

[23] H. David Politzer. Reliable perturbative results for strong interactions? *Phys. Rev. Lett.*, 30:1346–1349, Jun 1973.

[24] R. Hagedorn. Statistical thermodynamics of strong interactions at high-energies. *Nuovo Cim. Suppl.*, 3:147–186, 1965.

[25] N. Cabibbo and G. Parisi. Exponential Hadronic Spectrum and Quark Liberation. *Phys. Lett.*, B59:67–69, 1975.

[26] J. D. Bjorken. Highly Relativistic Nucleus-Nucleus Collisions: The Central Rapidity Region. *Phys. Rev.*, D27:140–151, 1983.

[27] Grazyna Odyniec. The RHIC beam energy scan program in star and what's next... *Journal of Physics: Conference Series*, 455(1):012037, 2013.

[28] Jeffery T. Mitchell. The RHIC beam energy scan program: Results from the phenix experiment. *Nuclear Physics A*, 904:903c – 906c, 2013.

[29] Michael L. Miller, Klaus Reygers, Stephen J. Sanders, and Peter Steinberg. Glauber modeling in high energy nuclear collisions. *Ann. Rev. Nucl. Part. Sci.*, 57:205–243, 2007.

[30] S. Voloshin and Y. Zhang. Flow study in relativistic nuclear collisions by Fourier expansion of Azimuthal particle distributions. *Z. Phys.*, C70:665–672, 1996.

[31] Jean-Yves Ollitrault. Determination of the reaction plane in ultrarelativistic nuclear collisions. *Phys. Rev.*, D48:1132–1139, 1993.

[32] S. S. Adler et al. Elliptic flow of identified hadrons in Au+Au collisions at $\sqrt{s_{NN}} = 200$ GeV. *Phys. Rev. Lett.*, 91:182301, 2003.

[33] Charles Gale, Sangyong Jeon, and Bjoern Schenke. Hydrodynamic Modeling of Heavy-Ion Collisions. *Int. J. Mod. Phys.*, A28:1340011, 2013.

[34] Miklos Gyulassy and Michael Plümer. Jet quenching in dense matter. *Physics Letters B*, 243(4):432 – 438, 1990.

[35] C. Adler et al. Disappearance of back-to-back high p_T hadron correlations in central Au+Au collisions at $\sqrt{s_{NN}} = 200$ GeV. *Phys. Rev. Lett.*, 90:082302, 2003.

[36] Vardan Khachatryan et al. Observation of Long-Range Near-Side Angular Correlations in Proton-Proton Collisions at the LHC. *JHEP*, 09:091, 2010.

[37] Serguei Chatrchyan et al. Observation of long-range near-side angular correlations in proton-lead collisions at the LHC. *Phys. Lett.*, B718:795–814, 2013.

[38] J. E. Augustin et al. Discovery of a Narrow Resonance in e^+e^- Annihilation. *Phys. Rev. Lett.*, 33:1406–1408, 1974. [Adv. Exp. Phys.5,141(1976)].

[39] J. J. Aubert et al. Experimental Observation of a Heavy Particle J. *Phys. Rev. Lett.*, 33:1404–1406, 1974.

[40] G. S. Abrams et al. The Discovery of a Second Narrow Resonance in e+ e- Annihilation. *Phys. Rev. Lett.*, 33:1453–1455, 1974. [Adv. Exp. Phys.5,150(1976)].

[41] S. Abachi et al. Search for high mass top quark production in $p\bar{p}$ collisions at $\sqrt{s} = 1.8$ TeV. *Phys. Rev. Lett.*, 74:2422–2426, 1995.

[42] F. Abe et al. Observation of top quark production in $\bar{p}p$ collisions. *Phys. Rev. Lett.*, 74:2626–2631, 1995.

[43] S. W. Herb et al. Observation of a Dimuon Resonance at 9.5-GeV in 400-GeV Proton-Nucleus Collisions. *Phys. Rev. Lett.*, 39:252–255, 1977.

[44] K. A. Olive et al. Review of Particle Physics. *Chin. Phys.*, C38:090001, 2014.

[45] P. Faccioli, C. Lourenco, J. Seixas, and H. K. Woehri. Study of ψ' and χ_c decays as feed-down sources of J/ψ hadro-production. *JHEP*, 10:004, 2008.

[46] Roel Aaij et al. Study of $\chi_{\rm b}$ meson production in p p collisions at $\sqrt{s} = 7$ and 8 TeV and observation of the decay $\chi_{\rm b}(3{\rm P}) \to \Upsilon(3{\rm S})\gamma$. *Eur. Phys. J.*, C74(10):3092, 2014.

[47] N. Brambilla et al. Heavy quarkonium: progress, puzzles, and opportunities. *Eur. Phys. J.*, C71:1534, 2011.

[48] T. Matsui and H. Satz. J/ψ Suppression by Quark-Gluon Plasma Formation. *Phys. Lett.*, B178:416, 1986.

[49] F. Karsch, M. T. Mehr, and H. Satz. Color Screening and Deconfinement for Bound States of Heavy Quarks. *Z. Phys.*, C37:617, 1988.

[50] Helmut Satz. Colour deconfinement and quarkonium binding. *J. Phys.*, G32:R25, 2006.

[51] A. Adare et al. J/ψ Production vs Centrality, Transverse Momentum, and Rapidity in Au+Au Collisions at $\sqrt{s_{NN}} = 200$ GeV. *Phys. Rev. Lett.*, 98:232301, 2007.

[52] Jaroslav Adam et al. J/ψ suppression at forward rapidity in Pb-Pb collisions at $\sqrt{s_{\rm NN}} = 5.02$ TeV. *Phys. Lett.*, B766:212–224, 2017.

[53] Albert M Sirunyan et al. Relative modification of prompt ψ(2S) and J/ψ yields from pp to PbPb collisions at $\sqrt{s_{\rm NN}} = 5.02$ TeV. *Submitted to: Phys. Rev. Lett.*, 2016.

[54] E. Scomparin. Quarkonium production in AA (pA) collisions. In *Quark Matter*, Chicago, Illinois, Feb. 6-11 2017.

[55] CMS Collaboration. Strong suppression of Υ excited states in PbPb collisions at $\sqrt{s_{NN}}$=5.02 TeV. CMS Physics Analysis Summary CMS-PAS-HIN-16-008, 2016.

[56] CMS Collaboration. Measurement of nuclear modification factor of $\Upsilon(nS)$ mesons in PbPb collisions at $\sqrt{s_{nn}}$=5.02 TeV. CMS Physics Analysis Summary CMS-PAS-HIN-16-023, 2016.

[57] Serguei Chatrchyan et al. Event activity dependence of $\Upsilon(nS)$ production in $\sqrt{s_{NN}}$=5.02 TeV pPb and $\sqrt{s}$=2.76 TeV pp collisions. *JHEP*, 04:103, 2014.

[58] Geoffrey T. Bodwin, Eric Braaten, and G. Peter Lepage. Rigorous QCD analysis of inclusive annihilation and production of heavy quarkonium. *Phys. Rev.*, D51:1125–1171, 1995. [Erratum: Phys. Rev.D55,5853(1997)].

[59] P. Faccioli. private communication.

[60] F. Abe et al. J/ψ and $\psi(2S)$ production in $p\bar{p}$ collisions at $\sqrt{s} = 1.8$ TeV. *Phys. Rev. Lett.*, 79:572–577, 1997.

[61] Mathias Butenschoen and Bernd A. Kniehl. J/ψ polarization at Tevatron and LHC: Nonrelativistic-QCD factorization at the crossroads. *Phys. Rev. Lett.*, 108:172002, 2012.

[62] Pietro Faccioli, Valentin Knunz, Carlos Lourenco, Joao Seixas, and Hermine K. Wohri. Quarkonium production in the LHC era: a polarized perspective. *Phys. Lett.*, B736:98–109, 2014.

[63] Serguei Chatrchyan et al. Measurement of the prompt J/ψ and ψ(2S) polarizations in pp collisions at $\sqrt{s} = 7$ TeV. *Phys. Lett.*, B727:381, 2013.

[64] Serguei Chatrchyan et al. Measurement of the $\Upsilon(1S)$, $\Upsilon(2S)$ and $\Upsilon(3S)$ polarizations in pp collisions at $\sqrt{s} = 7$ TeV. *Phys. Rev. Lett.*, 110(8):081802, 2013.

[65] T. Aaltonen et al. Measurements of Angular Distributions of Muons From Υ Meson Decays in $p\bar{p}$ Collisions at $\sqrt{s} = 1.96$ TeV. *Phys. Rev. Lett.*, 108:151802, 2012.

[66] R Aaij et al. Measurement of J/ψ polarization in pp collisions at $\sqrt{s} = 7$ TeV. *Eur. Phys. J.*, C73(11):2631, 2013.

[67] Betty Abelev et al. J/ψ polarization in pp collisions at $\sqrt{s} = 7$ TeV. *Phys. Rev. Lett.*, 108:082001, 2012.

[68] Eric Braaten and Sean Fleming. Color octet fragmentation and the psi-prime surplus at the Tevatron. *Phys. Rev. Lett.*, 74:3327–3330, 1995.

[69] Eric Braaten and Tzu Chiang Yuan. Gluon fragmentation into heavy quarkonium. *Phys. Rev. Lett.*, 71:1673–1676, 1993.

[70] Peter L. Cho and Mark B. Wise. Spin symmetry predictions for heavy quarkonia alignment. *Phys. Lett.*, B346:129–136, 1995.

[71] R. Vogt. Cold Nuclear Matter Effects on J/ψ and Υ Production at the LHC. *Phys. Rev.*, C81:044903, 2010.

[72] J. W. Cronin, Henry J. Frisch, M. J. Shochet, J. P. Boymond, R. Mermod, P. A. Piroue, and Richard L. Sumner. Production of hadrons with large transverse momentum at 200, 300, and 400 GeV. *Phys. Rev.*, D11:3105–3123, 1975.

[73] Pietro Faccioli, Carlos Lourenco, Joao Seixas, and Hermine K. Wohri. Towards the experimental clarification of quarkonium polarization. *Eur. Phys. J.*, C69:657–673, 2010.

[74] Eric Braaten, Bernd A. Kniehl, and Jungil Lee. Polarization of prompt J/ψ at the Tevatron. *Phys. Rev.*, D62:094005, 2000.

[75] D. Acosta et al. Υ production and polarization in $p\bar{p}$ collisions at $\sqrt{s} = 1.8$ TeV. *Phys. Rev. Lett.*, 88:161802, 2002.

[76] V. M. Abazov et al. Measurement of the polarization of the $\Upsilon 1S$ and $\Upsilon 2S$ states in $p\bar{p}$ collisions at $\sqrt{s} = 1.96$ TeV. *Phys. Rev. Lett.*, 101:182004, 2008.

[77] Lyndon Evans and Philip Bryant. LHC Machine. *JINST*, 3:S08001, 2008.

[78] G. L. Bayatian et al. CMS Physics: Technical Design Report. 2006.

[79] G. L. Bayatian et al. CMS Technical Design Report, Volume II: Physics Performance. *J. Phys.*, G34(6):995–1579, 2007.

[80] S. Chatrchyan et al. The CMS Experiment at the CERN LHC. *JINST*, 3:S08004, 2008.

[81] Cinzia De Melis. The CERN accelerator complex. Complexe des accelerateurs du CERN. Jan 2016. General Photo.

[82] Karlheinz Schindl. The injector chain for the LHC. (CERN-OPEN-99-052):6 p, Jan 1999.

[83] David Barney. CMS Detector Slice. CMS Collection., Jan 2016.

[84] W. Adam et al. The CMS high level trigger. *Eur. Phys. J.*, C46:605–667, 2006.

[85] CMS Collaboration. CMS B-Physics and Quarkonia Results. https://twiki.cern.ch/-twiki/bin/view/CMSPublic/PhysicsResultsBPH, 2011.

[86] CMS: The computing project. Technical design report. 2005.

[87] Ilse Kratschmer. *Measurements of prompt J/ψ and $\psi(2S)$ production and polarization at CMS*. PhD thesis, Vienna, OAW, 2015.

[88] Valentin Karl Knunz. *Measurement of Quarkonium Polarization to Probe QCD at the LHC*. PhD thesis, Vienna, OAW, 2015.

[89] Vardan Khachatryan et al. Υ(nS) polarizations versus particle multiplicity in pp collisions at $\sqrt{s} = 7$ TeV. *Phys. Lett.*, B761:31–52, 2016.

[90] P. Faccioli, J. Seixas, and V. Knünz. A new procedure for the determination of angular distribution parameters in dilepton vector meson decays. CMS Note AN-2011/535, 2011.

[91] Hermine Wohri et al. T&P single muon efficiencies for low p_{T} dimuon triggers in 2011. CMS Note AN-2011/417, 2011.

[92] Hermine Wohri et al. Low p_{T} Muon and Dimuon Efficiencies. CMS Note AN-2012/088, 2012.

[93] C. Lourenço, H.K. Wöhri, P. Faccioli, J. Seixas, V. Knünz, I. Krätschmer, et al. J/ψ and $\psi(2s)$ polarization in pp collisions at $\sqrt{s} = 7$ tev. CMS Note AN-2013/016, 2013.

[94] P. Faccioli, V. Knünz, I. Krätschmer, C. Lourenço, J. Seixas, H.K. Wöhri, et al. Measurement of the Υ(1S), Υ(2S) and Υ(3S) polarizations in pp collisions at $\sqrt{s} = 7$ TeV. CMS Note AN-2012/140, 2012.

[95] C. Ferraioli, C. Lourenço, H.K. Wöhri, P. Faccioli, J. Seixas, V. Knünz, I. Krätschmer, et al. Υ(nS) polarizations in pp collisions versus charged particle multiplicity. CMS Note AN-2015/024, 2015.

[96] C. Ferraioli, C. Lourenço, P. Faccioli, J. Seixas, V. Knünz, and I. Krätschmer. J/ψ and ψ(2S) polarizations in pp collisions versus charged particle multiplicity. CMS Note AN-2017/050, 2017.

[97] CMS Collaboration. Measurement of Tracking Efficiency. 2010.

[98] Vardan Khachatryan et al. Measurements of Inclusive W and Z Cross Sections in pp Collisions at $\sqrt{s} = 7$ TeV. *JHEP*, 01:080, 2011.

[99] W. K. Hastings. Monte Carlo sampling methods using Markov chains and their applications. *Biometrika*, 57(1):97–109, 1970.

[100] The CMS Collaboration. Description and performance of track and primary-vertex reconstruction with the CMS tracker. *Journal of Instrumentation*, 9(10):P10009, 2014.

[101] Serguei Chatrchyan et al. Measurement of the $\Upsilon(1S)$, $\Upsilon(2S)$, and $\Upsilon(3S)$ cross sections in pp collisions at $\sqrt{s} = 7$ TeV. *Phys. Lett.*, B727:101–125, 2013.

[102] Pietro Faccioli, Carlos Lourenco, Joao Seixas, and Hermine K. Wohri. Determination of χ_c and χ_b polarizations from dilepton angular distributions in radiative decays. *Phys. Rev.*, D83:096001, 2011.

[103] Pietro Faccioli, Carlos Lourenço, João Seixas, and Hermine K. Wöhri. Determination of χ_c and χ_b polarizations from dilepton angular distributions in radiative decays. *Phys. Rev. D*, 83:096001, May 2011.

[104] Pietro Faccioli and João Seixas. Observation of χ_c and χ_b nuclear suppression via dilepton polarization measurements. *Phys. Rev. D*, 85:074005, 2012.

[105] Vardan Khachatryan et al. Measurement of Prompt $\psi(2S) \rightarrow J/\psi$ Yield Ratios in Pb-Pb and $p-p$ Collisions at $\sqrt{s_{NN}} = 2.76$ TeV. *Phys. Rev. Lett.*, 113(26):262301, 2014.